

NASA/CR—1998-207932



Determination of Yield and Flow Surfaces for Inconel 718 Under Axial-Torsional Loading at Temperatures up to 649 °C

Christopher M. Gil
Pennsylvania State University, University Park, Pennsylvania

Prepared under Cooperative Agreement NCC3-597

National Aeronautics and
Space Administration

Lewis Research Center

July 1998

Acknowledgments

First, I would like to thank my thesis advisor, Professor Cliff Lissenden for his support and guidance in completing this thesis. I would also like to thank Dr. Brad Lerch (NASA LeRC), my mentor throughout the experimental portion of this project.

I am grateful to Ralph Corner and Chris Burke (both of NASA LeRC) for their assistance in performing the experiments reported herein.

I would also like to acknowledge the members of this thesis reading committee, Professors Charles E. Bakis and Richard Queeney for their reading of this thesis.

Finally, the financial support of NASA Lewis Research Center is gratefully acknowledged.

Trade names or manufacturers' names are used in this report for identification only. This usage does not constitute an official endorsement, either expressed or implied, by the National Aeronautics and Space Administration.

Available from

NASA Center for Aerospace Information
7121 Standard Drive
Hanover, MD 21076
Price Code: A08

National Technical Information Service
5287 Port Royal Road
Springfield, VA 22100
Price Code: A08

The Pennsylvania State University

The Graduate School

College of Engineering

**DETERMINATION OF YIELD AND FLOW SURFACES FOR
INCONEL 718 UNDER AXIAL-TORSIONAL LOADING
AT TEMPERATURES UP TO 649°C**

A Thesis in

Engineering Mechanics

by

Christopher M. Gil

Copyright 1998 Christopher M. Gil

Submitted in Partial Fulfillment
of the Requirements
for the Degree of

Master of Science

May 1998

We approve the thesis of Christopher M. Gil.

Date of Signature

Cliff J. Lissenden

4-6-98

Cliff J. Lissenden

Assistant Professor of Engineering Science and Mechanics

Thesis Advisor

Richard A. Queeney

4/6/98

Richard A. Queeney

Professor of Engineering Mechanics

Charles E. Bakis

4/6/98

Charles E. Bakis

Associate Professor of Engineering Science and Mechanics

Richard P. McNitt

4-6-98

Richard P. McNitt

Professor of Engineering Science and Mechanics

Head of the Department of Engineering Science and Mechanics

Abstract

An experimental program to determine flow surfaces has been established and implemented for solution annealed and aged IN718. The procedure involved subjecting tubular specimens to various ratios of axial-torsional stress at temperatures between 23 and 649°C and measuring strain with a biaxial extensometer. Each stress probe corresponds to a different direction in stress space, and unloading occurs when a 30 microstrain ($1 \mu\epsilon = 10^{-6}$ mm/mm) offset is detected. This technique was used to map out yield loci in axial-torsional stress space.

Flow surfaces were determined by post-processing the experimental data to determine the inelastic strain rate components. Surfaces of constant inelastic strain rate (SCISRs) and surfaces of constant inelastic power (SCIPs) were mapped out in the axial-shear stress plane.

The von Mises yield criterion appeared to closely fit the initial loci for solutioned IN718 at 23°C. However, the initial loci for solutioned IN718 at 371 and 454°C, and all of the initial loci for aged IN718 were offset in the compression direction. Subsequent loci showed translation, distortion, and for the case of solutioned IN718, a slight cross effect. Aged IN718 showed significantly more hardening behavior than solutioned IN718.

Table of Contents

<u>Section</u>	<u>Page</u>
List of Tables	vi
List of Figures	vii
Acknowledgements	xi
Chapter 1: Introduction and Objectives.....	1
Chapter 2: Review of Rate-Independent Deformation in Metals.....	4
2.1 Physical Mechanisms.....	4
2.2 Multiaxial Deformation.....	6
2.2.1 Criteria For Initial Yielding.....	6
2.2.2 Loading Criteria.....	8
2.2.3 Plastic Stress-Strain Relations.....	11
2.2.4 Hardening Laws.....	12
2.2.5 Experiments.....	15
2.3 The Strength-Differential Effect.....	23
Chapter 3: Experimental and Material Details	29
3.1 Material and Specimen Details	29
3.2 Test Equipment.....	34
3.3 Experimental Procedure.....	38
3.3.1 Yield Loci.....	39
3.3.2 Radial Prestraining.....	43
Chapter 4: Experimental Results and Discussion.....	46
4.1 Solutioned Inconel 718.....	46
4.2 Aged Inconel 718	69
4.3 Re-Solutioned Inconel 718.....	80
Chapter 5: Review of Viscoplasticity in Metals	84
5.1 Physical Mechanisms.....	84
5.2 Thermodynamic Framework of Unified Viscoplasticity	86
5.2.1 General Principles.....	87
5.2.2 The State Law	88
5.2.3 The Dissipation Potential.....	89
5.3 Unified Viscoplasticity Models.....	90
5.3.1 Bodner-Partom	90
5.3.2 GVIPS.....	92
5.4 Experimental Considerations	94
Chapter 6: Rate-Dependent Flow Surfaces	97
6.1 Data Reduction Methodology.....	97
6.1.1 Basic Assumptions	98

6.1.2 Determination of Elastic Constants	99
6.1.3 Determining the Inelastic Strains and Thresholds.....	99
6.1.4 Determining Inelastic Strain Rates and Flow Surfaces	100
6.1.5 Software Details	102
6.1.6 Procedure of Clinard and Lacombe.....	104
6.2 SCISR and SCIP Results	106
6.2.1 Solutioned Inconel 718.....	106
6.2.2 Aged Inconel 718.....	113
Chapter 7: Summary, Conclusions, and Future Work	123
7.1 Summary	123
7.2 Conclusions.....	124
7.3 Future Work	125
References.....	127
Appendix A: Yield Loci and Flow Surface Data	134
A.1 Yield Loci	134
A.2 Flow Surfaces	139
Appendix B: Flow Surface Experiments on SiC/Ti-6-2-4-2	143
B.1 Introduction.....	143
B.2 Reults, Discussion, and Suggested Future Work.....	143

List of Tables

<u>Table</u>		<u>Page</u>
3.1	Material composition of Inconel 718.....	30
4.1	Radius and center of each initial yield locus for solutioned and aged IN718 as a function of temperature.....	78

List of Figures

<u>Figure</u>		<u>Page</u>
2.1	Tresca and von Mises yield criteria in the axial-shear stress plane	9
2.2	Isotropic and kinematic hardening in the axial-shear stress plane	13
2.3	Definitions of yielding used in yield surface experiments.....	17
3.1	Typical specimen geometry showing longitudinal and transverse cross sections.....	30
3.2	Optical microstructure of solutioned Inconel 718	32
3.3	Transmission electron microscopy of aged Inconel 718 showing precipitation.....	33
3.4	Servohydraulic test machine and hydraulics.....	35
3.5	Close-up of specimen, extensometer, and heating coils.....	36
3.6	Probe directions used in determining a yield locus.....	40
3.7	Calculation of E, G, and ϵ^{off} during experiments.....	42
3.8	Prestrain paths shown in (a) equivalent strain space and (b) equivalent stress space	44
4.1	Offset strain versus strain during tensile loading for solutioned IN718.....	47
4.2	Yield loci for solutioned IN718 determined under stress and strain control at room temperature	50
4.3	The slope of the diametral strain versus axial strain gives a Poisson's ratio of 0.34.....	51

4.4	Effect of using different values for Poisson's ratio to define the equivalent offset strain	53
4.5	Yield loci for solutioned IN718 defined by target values of 10, 20, and 30 $\mu\epsilon$ equivalent offset	54
4.6	Initial yield loci for solutioned IN718 at room temperature	56
4.7	Comparison of electronic noise at 23 and 454°C	57
4.8	Initial yield loci for solutioned IN718 at 371°C	59
4.9	Initial yield loci for solutioned IN718 at 454°C	60
4.10	Loading history for specimen IN-6 indicating where yield loci were determined.....	61
4.11	Yield locus subsequent to a tension-torsion prestrain of 500 $\mu\epsilon$ offset for solutioned IN718 at 454°C.....	63
4.12	Axial and shear stress-strain curves for a proportional prestrain of a 500 $\mu\epsilon$ equivalent offset for solutioned IN718 at 454°C	64
4.13	Combined axial-torsional cyclic loading at room temperature ($\theta = 45^\circ$)	65
4.14	Yield locus subsequent to cyclic loading for solutioned IN718 at 454°C	67
4.15	Subsequent yield loci for proportional prestraining to 1000 $\mu\epsilon$ offset (locus Q) and 1500 $\mu\epsilon$ offset (locus S) for solutioned IN718 at 454°C.....	68
4.16	Offset strain versus strain during compressive loading for aged IN718, indicating stiffening.....	70
4.17	Initial yield loci for aged IN718 at room temperature.....	73
4.18	Stress versus offset strain for solutioned and aged IN718 under tension and torsion.....	75

4.19	Initial yield loci for aged IN718 at 649°C	76
4.20	Yield locus subsequent to a tension-torsion prestrain of 500 $\mu\epsilon$ offset for aged IN718 at 649°C.....	79
4.21	Yield locus subsequent to a tension prestrain of 9000 $\mu\epsilon$ (0.9%) for aged IN718 at 649°C	81
4.22	Comparison of yield loci for a solutioned specimen in the virgin state and after significant deformation followed by re-solutioning	82
6.1	Axial inelastic strain as a function of time and a sixth-order polynomial curve-fit	101
6.2	Determination of time t and the stresses σ_{11} and σ_{12} associated with the target value	103
6.3	Initial SCISR and SCIP for solutioned IN718 at 23°C	107
6.4	Initial SCISR for solutioned IN718 at 371°C.....	109
6.5	Initial SCIPs for solutioned IN718 at 371°C	110
6.6	Subsequent SCISR for solutioned IN718 at 454°C after a proportional prestrain of 500 $\mu\epsilon$ offset.....	111
6.7	Subsequent SCIPs for solutioned IN718 at 454°C after a proportional prestrain of 500 $\mu\epsilon$ offset.....	112
6.8	Initial SCISR for aged IN718 at 23°C	114
6.9	Initial SCIPs for aged IN718 at 23°C.....	115
6.10	Initial SCISR for aged IN718 at 649°C	116
6.11	Initial SCIPs for aged IN718 at 649°C.....	117
6.12	Subsequent SCISR for aged IN718 at 649°C after a proportional prestrain of 500 $\mu\epsilon$ offset.....	118

6.13	Subsequent SCIPs for aged IN718 at 649°C after a proportional prestrain of 500 $\mu\epsilon$ offset.....	119
6.14	Subsequent SCISR for aged IN718 at 649°C after a tensile prestrain of 9000 $\mu\epsilon$ (0.9%).....	121
6.15	Subsequent SCIPs for aged IN718 at 649°C after a tensile prestrain of 9000 $\mu\epsilon$ (0.9%).....	122
B.1	Max/Min stresses for SiC/Ti-6-2-4-2 tubes under axial loading at 482°C	145
B.2	Attempt at an initial surface on SiC/Ti-6-2-4-2 at 482°C	146

Acknowledgements

First, I would like to thank my thesis advisor, Professor Cliff Lissenden for his support and guidance in completing this thesis. I would also like to thank Dr. Brad Lerch (NASA LeRC), my mentor throughout the experimental portion of this project.

I am grateful to Ralph Corner and Chris Burke (both of NASA LeRC) for their assistance in performing the experiments reported herein.

I would also like to acknowledge the members of this thesis reading committee, Professors Charles E. Bakis and Richard Queeney for their reading of this thesis.

Finally, the financial support of NASA Lewis Research Center is gratefully acknowledged.

CHAPTER 1

INTRODUCTION AND OBJECTIVES

Gas turbine engine components are continuously subjected to multiaxial stress states at elevated temperatures. The materials that are used in such applications must possess unique mechanical properties over a wide range of temperatures. Furthermore, engine designers should be equipped with every possible tool when designing these components. Multiaxial deformation models, such as the GVIPS (Arnold et al., 1996) and Bodner-Partom (1987) viscoplasticity models, have the potential to be valuable tools to the design engineer. So far these models have been of limited use in design because of the lack of experimental data needed to validate them for multiaxial loads. Simple tension tests supply the necessary parameters to characterize these models, however only through multiaxial loading experiments will the models be authenticated for use in design.

The nickel-base superalloy Inconel 718 (IN718) is currently being used in gas turbine engines for applications such as disks and shafts. Its popularity in the aerospace industry is largely due to its excellent strength and fatigue characteristics under extreme temperature environments. Experimental

investigations into the strengthening mechanisms and fatigue behavior of IN718 have been reported by several authors (e.g., Oblak et al., 1974; Fournier and Pineau, 1977; Sundararaman et al., 1988; Worthem et al., 1989; Kalluri et al., 1997). Also, the parameters for the Chaboche and Bodner-Partom viscoplasticity models have been experimentally determined by Abdel-Kader et al. (1986) and Li (1995), respectively. However, until now there has been no experimental data published to describe the multiaxial yield, flow, and hardening behavior of IN718.

The objectives of this study are twofold: (1) to demonstrate that initial and subsequent yield loci can be determined for metallic materials (such as IN718) at temperatures up to 649°C by probing a single specimen multiple times and measuring strains with a biaxial extensometer, and (2) to provide experimental data for IN718 for use in validating and suggesting modifications to existing multiaxial deformation models. This is achieved through the determination of yield loci and rate-dependent flow surfaces.

In the next chapter a review of rate-independent deformation mechanisms, theory, and experiments is given. Chapter 3 discusses the material and experimental details. In Chapter 4, the experimental results are presented and discussed. Chapter 5 gives a review of viscoplasticity in metals. Chapter 6 explains the data reduction procedure for determining flow surfaces, followed by a presentation and discussion of the flow surface results. Finally,

Chapter 7 provides a summary of this work, states the conclusions, and gives suggestions for future work.

CHAPTER 2

REVIEW OF RATE-INDEPENDENT DEFORMATION IN METALS

This chapter focuses on the physical, theoretical, and experimental aspects of rate-independent deformation. Section 2.1 discusses the physical mechanisms of plastic deformation with regards to the changing microstructure. In section 2.2, the focus is on multiaxial deformation theory. Yielding, plastic flow, and hardening are discussed, followed by a review of selected experimental results. Finally, section 2.3 is a review of the strength-differential (SD) effect. Rate-dependent deformation is covered in Chapter 5.

2.1 Physical Mechanisms

The objective of this section is to review some of the physical mechanisms that occur during time-independent plastic deformation as they may relate to this work. There are other physical mechanisms associated with time-independent plastic deformation that are not mentioned here, however a comprehensive discussion of the microstructural effects related to plasticity can be found in several texts (e.g., Khan and Huang, 1995; Stouffer and Dame, 1996).

The most common deformation mechanism at low temperatures (less than one-half the absolute melting temperature) is slip. Slip occurs most easily on slip planes of high atomic density that are closest to the planes with the maximum amount of shear stress. These planes and directions differ depending on the crystallographic structure of the metal and the direction of the applied load.

During plastic deformation many metals experience a resistance to slip called strain hardening. Hardening occurs due to interactions of dislocations with precipitates, grain boundaries, or other dislocations and often leads to dislocation pileups. Back stress may result from the dislocation interactions causing a resistance to further deformation. However, dislocations will propagate more easily upon a reversal in the loading direction due to the back stress and may cause yielding to occur at a lower applied stress level. This phenomenon is known as the Bauschinger effect.

The grain size also has an effect on strain hardening. More slip systems are active at the grain boundaries, thus more hardening occurs near grain boundaries. However, as the grain size decreases there is more strain hardening near the center of the grain. Therefore, metals with smaller grain sizes generally exhibit more hardening because a larger volume of the material is strain hardened.

Strengthening in metals is achieved by slowing the movement of dislocations. This can be achieved by precipitation hardening, in which fine particles of a second phase material are dispersed throughout the grains. Dislocations are pinned at these particles causing dislocation pileups. In order to overcome the precipitate particles the dislocations must either climb over or shear through them, both of which require additional shear stress.

2.2 Multiaxial Deformation

A rate-independent (classical) mathematical theory of plasticity is frequently used to describe the multiaxial deformation of metals at room temperature. Mathematical plasticity theories are phenomenological in nature and must be based on experimental observations. This subsection reviews the fundamental aspects of rate-independent plasticity, which include an initial yield criterion, the definition of loading and unloading, plastic stress-strain relations, and hardening. In the last section a brief history of yield surface experiments is discussed.

2.2.1 Criteria For Initial Yielding

Yielding due to multiaxial stress states can be described by a yield surface. Under isothermal conditions, the initial yield surface of an isotropic metal can be defined by

$$f = F(\sigma_{ij}) - k = 0 \quad (2.1)$$

where $F(\sigma_{ij})$ is a function of the current stress state and k is usually related to the tensile yield strength. Yielding is assumed to occur when $f = 0$, and stress states outside of the yield surface are not permissible. Thus, the yield surface evolves when plastic deformation occurs such that the stress state remains on the yield surface.

Several multiaxial yield criteria have been developed to describe the onset of inelastic flow. The two most popular theories are the Tresca and von Mises yield criteria. Both theories assume an isotropic material and neglect the effect of hydrostatic stress.

The Tresca yield criterion (Tresca, 1864), also known as the maximum shear stress theory, predicts yielding to occur when the maximum shear stress in the material exceeds the tensile yield strength. This criterion is expressed in terms of the principal stress components as

$$\max(|\sigma_I - \sigma_{II}|, |\sigma_{II} - \sigma_{III}|, |\sigma_{III} - \sigma_I|) = \sigma_{TY} \quad (2.2)$$

where σ_I , σ_{II} , and σ_{III} denote the principal normal stresses and σ_{TY} is the yield strength in tension. Since the current work involves axial-torsional loading of tubular specimens, the Tresca criterion is expressed in terms of axial stress and one shear stress component as

$$\sigma_{11}^2 + 4\sigma_{12}^2 = \sigma_{TY}^2 \quad (2.3)$$

where σ_{11} and σ_{12} denote the axial and shear stress, respectively. The Tresca criterion is simple to apply, however it often provides a somewhat conservative prediction of yielding.

The von Mises yielding criterion (von Mises, 1913), also called the maximum distortion energy theory, often agrees more closely with experimental results. Yielding is predicted to occur when the maximum distortion energy exceeds the distortion energy required to cause yielding in pure tension. The von Mises criterion is often expressed as

$$J_2 - k^2 = 0 \quad (2.4)$$

where J_2 is the second invariant of deviatoric stress and k is the yield strength in tension. The von Mises criterion can also be expressed in terms of principle stress components as

$$\sqrt{\frac{1}{2}[(\sigma_I - \sigma_{II})^2 + (\sigma_{II} - \sigma_{III})^2 + (\sigma_{III} - \sigma_I)^2]} = \sigma_{TY} \quad (2.5)$$

and in terms of axial stress and one shear stress component as

$$\sigma_{11}^2 + 3\sigma_{12}^2 = \sigma_{TY}^2 \quad (2.6)$$

Figure 2.1 shows a comparison of the Tresca and von Mises criteria in the axial-shear stress plane.

2.2.2 Loading Criteria

Before proceeding to the discussion of time-independent plastic flow, it is first important to define the three different types of loading. For a material

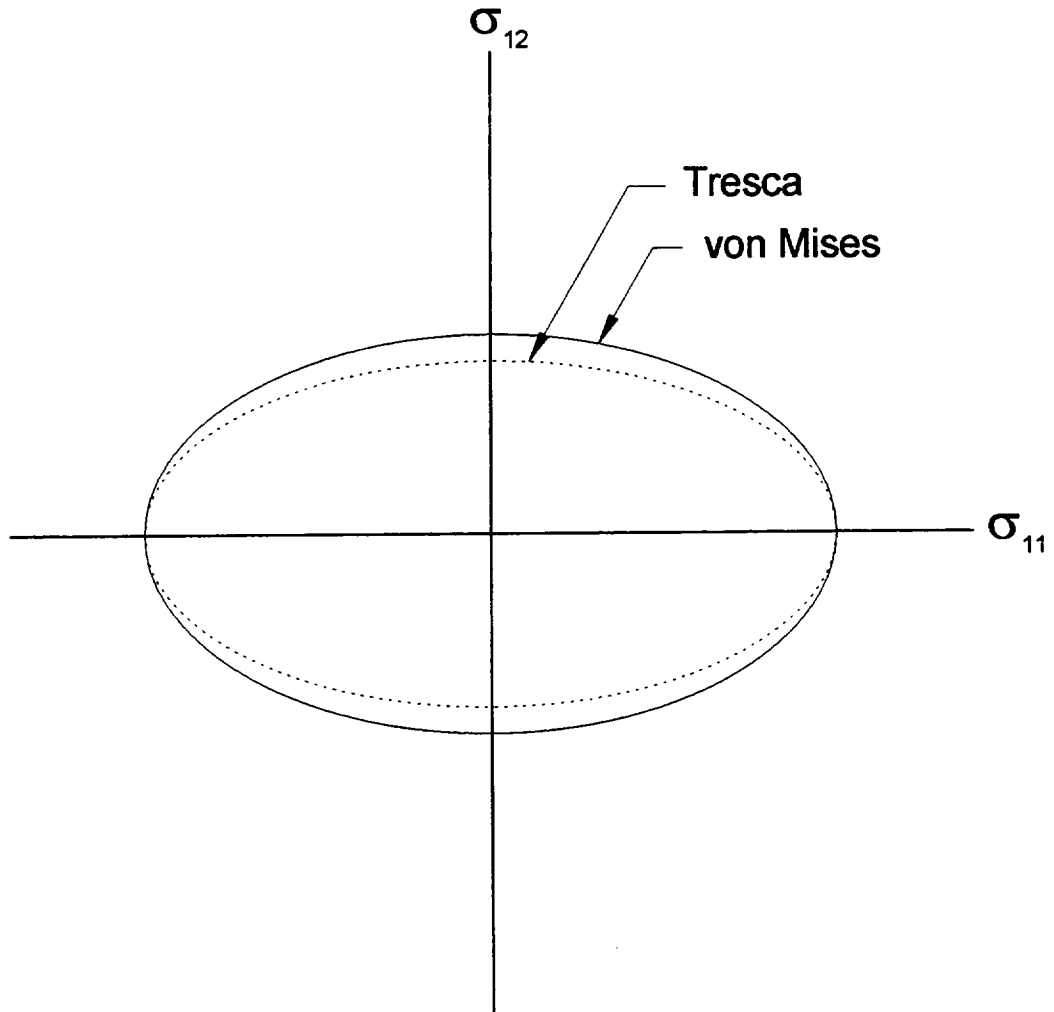


Figure 2.1 - Tresca and von Mises yield criteria in the axial-shear stress plane.

that exhibits strain (or work) hardening, *loading* occurs when the current stress state is on the yield surface, $f = 0$, and an additional stress increment, $d\sigma_{ij}$, is applied that produces plastic strain. Since it is not permissible to have stress states outside of the yield surface, loading results in changes to the yield surface. Therefore, the loading criterion is

$$f = 0 \quad \text{and} \quad \frac{\partial f}{\partial \sigma_{ij}} d\sigma_{ij} > 0 \quad (2.7)$$

Unloading occurs when the current stress state is on the yield surface and an additional stress increment moves the stress state inside the yield surface. Thus, if the unloading criterion,

$$f = 0 \quad \text{and} \quad \frac{\partial f}{\partial \sigma_{ij}} d\sigma_{ij} < 0 \quad (2.8)$$

is satisfied no plastic straining occurs.

Finally, neutral loading occurs when the current stress state is on the yield surface and an infinitesimal stress increment is applied that is tangent to the yield surface. The stress state remains on the yield surface, therefore no hardening occurs. The neutral loading criterion is expressed as

$$f = 0 \quad \text{and} \quad \frac{\partial f}{\partial \sigma_{ij}} d\sigma_{ij} = 0 \quad (2.9)$$

For elastic-perfectly plastic materials the unloading criterion remains the same. However, since no hardening occurs for this type of material the yield

surface will not change. Thus, the loading criterion has the form of Equation (2.9) and a neutral loading criterion is not defined.

2.2.3 Plastic Stress-Strain Relations

Plastic flow begins to occur when the loading criterion has been satisfied. Since plastic flow causes changes to the yield surface (and consequently permanent changes to the microstructure), it is important to quantify the plastic strain as a function of the current stress state. Since plastic strain is often nonlinear with respect to stress, it is necessary to compute plastic strain increments, $d\varepsilon_{ij}^p$.

A general flow rule relating the plastic strain increments to the stress state can be expressed as

$$d\varepsilon_{ij}^p = d\lambda \frac{\partial \Omega(\sigma_{ij})}{\partial \sigma_{ij}} \quad (2.10)$$

where Ω is a plastic potential (von Mises, 1928) that is a scalar function of the stress components and $d\lambda$ is a nonnegative scalar quantity that is zero unless the current stress state is on the yield surface and the loading condition is satisfied. Since $\partial \Omega / \partial \sigma_{ij}$ is normal to the plastic potential function, Ω , Equation (2.10) shows that the plastic strain increment is always normal to the plastic potential function. Hence, Equation (2.10) is often called the *normality flow rule*.

When a yield function (such as von Mises or Tresca) is substituted for Ω , then Equation (2.10) is an *associated* flow rule (Bland, 1957). The flow rule associated with the von Mises yield criterion ($J_2 = k^2$) is the Prandtl-Reuss flow equation (Prandtl, 1924; Reuss, 1930),

$$d\varepsilon_{ij}^p = d\lambda s_{ij} \quad (2.11)$$

where s_{ij} is the deviatoric stress tensor. The scalar quantity $d\lambda$ can be determined using a yield function in Equation (2.10) and a hardening law.

2.2.4 Hardening Laws

When loading occurs (as defined in section 2.2.2) the yield surface evolves such that the stress state remains on the yield surface. The evolution of the yield surface as a result of the loading history depends on the hardening characteristics of the material. Several theories have been developed to describe hardening in metals. The two most common are isotropic and kinematic hardening. According to the isotropic hardening theory, the yield surface expands uniformly without changing shape while its center remains fixed at the stress origin. Kinematic hardening occurs when the yield surface translates in stress space, but remains the same shape and size. Figure 2.2 shows isotropic and kinematic hardening in the axial-shear stress plane.

The general form of the isotropic hardening theory is written as

$$f = F(\sigma_{ij}) - k(q) = 0 \quad (2.12)$$

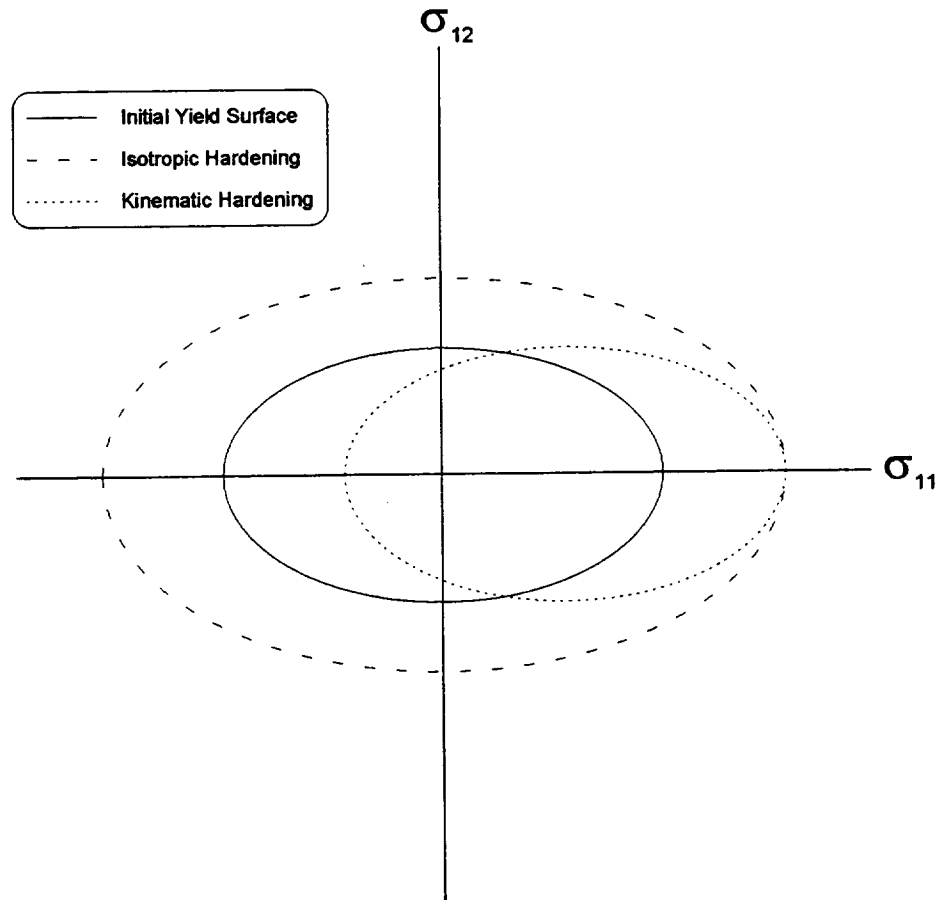


Figure 2.2 - Isotropic and kinematic hardening in the axial-shear stress plane.

where $F(\sigma_{ij})$ is an appropriate yield function and $k(q)$ is a scalar function of the deformation history that defines the overall size of the yield surface. The parameter q is a state variable that defines the current state of hardening in the material. As isotropic hardening occurs, the value of $k(q)$ becomes larger describing an increase of the yield stress in all directions.

The kinematic hardening theory was developed to account for the Bauschinger effect. It can be expressed mathematically as

$$f = F(\sigma_{ij} - \alpha_{ij}) - k = 0 \quad (2.13)$$

where α_{ij} is called the *back stress tensor* and k is determined by the initial yield stress in tension. The back stress tensor (Prager, 1956; Ziegler, 1959) describes the translation of the center of the yield surface as a function of the deformation history. Since the yield surface does not change in size or orientation, k does not change as a result of deformation.

Several other hardening theories have been developed to describe hardening subsequent to plastic flow. Voyiadjis and Foroozesh (1990) have proposed a hardening model that includes isotropic, kinematic, and distortion components. A two-parameter and a three-parameter version have been developed. Both versions use variations of the Hill (1948) fourth-order anisotropy tensor, M_{ijkl} . The two-parameter model is expressed as

$$F^{(m)} \equiv M_{ijkl}^{(m)} (\mathbf{s}_{kl} - \alpha_{kl})(\mathbf{s}_{ij} - \alpha_{ij}) = k^2 \quad (2.14)$$

where $F^{(m)}$ is the yield function after the m th load increment and

$$M_{ijkl}^{(m)} = \frac{1}{2} \delta_{ik} \delta_{jl} + \sum_{n=1}^m \dot{a}^{(n)} \delta_{ik} \delta_{jl} + \sum_{n=1}^m \dot{b}^{(n)} v_{ij}^{(n)} v_{kl}^{(n)} \quad (2.15)$$

where \dot{a} and \dot{b} are material parameters associated with the plastic work and v_{ij} define the directions of distortion. The three parameter model includes one additional material parameter to account for unequal distortion of the forward and rear segments of the yield surface,

$$M_{ijkl}^{(m)} = \frac{1}{2} \delta_{ik} \delta_{jl} + \sum_{n=1}^m \dot{a}^{(n)} \delta_{ik} \delta_{jl} + \sum_{n=1}^m \dot{b}^{(n)} v_{ij}^{(n)} v_{kl}^{(n)} + (s_{rs}^{(m)} - \alpha_{rs}^{(m)}) \sum_{n=1}^m \dot{c}^{(n)} v_{rs}^{(n)} v_{ij}^{(n)} v_{kl}^{(n)} \quad (2.16)$$

where \dot{c} is an additional material parameter.

2.2.5 Experiments

There have been many experimental investigations on the yield and flow behavior of metals. No attempt is made here to cover every investigation, however comprehensive literature reviews are given by Hecker (1976) and Michno and Findley (1976). The investigations referenced here were chosen based on their applicability to the current work.

The most popular type of yield surface experiments involve subjecting thin-walled tubular specimens to combined axial-torsional loading. The stress state is easily controlled and different ratios of axial and shear stress can easily be applied in order to map out yield loci in the axial-shear stress plane.

Internal pressure can also be applied to tubular specimens to define yield surfaces in three-dimensional stress space.

In order to determine the yield point it is necessary to load the material into the plastic range and consequently change the material state. Multiaxial yield experiments involve determining several yield points for the same material. If all of the yield points are obtained from the same specimen, then it is critical to minimize the change in material state associated with each yield point determination. However, if each yield point is determined from a different specimen, then the results are subject to specimen-to-specimen scatter. Thus, the method for determining yielding is an important issue of these experiments.

The three most popular yield definitions are (1) the proportional limit definition, (2) the offset strain definition, and (3) the back-extrapolation definition. These are summarized graphically in Figure 2.3. The proportional limit definition implies that yielding begins to occur at the onset of plastic strain. According to the offset strain definition, yielding has occurred when an arbitrary amount of plastic strain has accumulated. Finally, the back-extrapolation method defines yielding as the intersection of the elastic loading line and a line drawn tangent to the plastic portion of the stress-strain curve.

Using the proportional limit definition involves loading the material until the first sign of nonlinearity in the stress-strain curve is observed. This procedure requires very precise strain measurement so that very little plastic

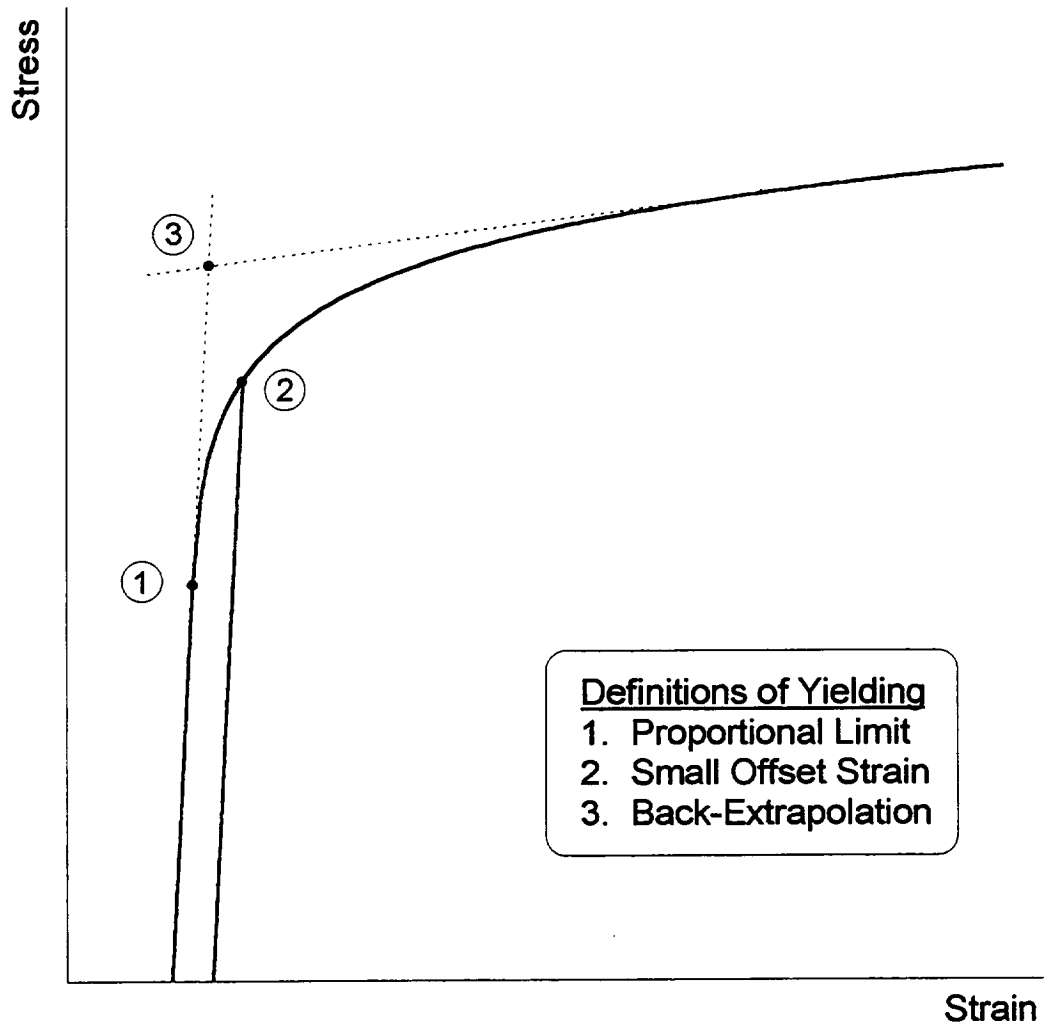


Figure 2.3 - Definitions of yielding used in yield surface experiments.

strain ($< 3 \times 10^{-6}$ mm/mm) is accumulated. Phillips and coworkers (1972) used a combination of the proportional limit and back-extrapolation definitions to determine yield loci for aluminum. Yielding was assumed to have occurred when more than two consecutive data points deviated to the same side of the elastic loading line. Each excursion into the plastic region was approximately $3 \mu\epsilon$ (3×10^{-6} mm/mm). Then a straight line was drawn through the first three data points deviating from the elastic line. The intersection of this line and the elastic line defined the yield point (proportional limit).

The offset strain definition of yielding is more easily applied in experiments, however the magnitude of the offset is rather arbitrary. For multiaxial experiments a target value of equivalent offset strain is used, as defined by

$$\epsilon_{eq}^{off} = \sqrt{\frac{2}{3} \epsilon_{ij}^{off} \epsilon_{ij}^{off}} = \sqrt{(\epsilon_{11}^{off})^2 + \frac{4}{3} (\epsilon_{12}^{off})^2} \quad (2.17)$$

for axial-torsional loading, where ϵ_{11}^{off} and ϵ_{12}^{off} are the axial and tensorial shear offset strains, respectively. A very small equivalent offset strain, such as $5 \mu\epsilon$, represents initiation of yielding (slip in a few grains) and is essentially the same as the proportional limit definition. Large offsets, such as the commonly used 0.2% offset, give more of a macroscopic definition of yielding and represent overall plastic flow. For small offset definitions, a single specimen can be used to determine all of the yield points. Large target value definitions significantly

change the material during each probe and therefore require that multiple specimens be used. There appears to be no distinct target value of offset strain below which one specimen can be used to determine the entire yield surface. Target values between $5 \mu\epsilon$ (Helling et al., 1986) and $100 \mu\epsilon$ (Nouailhas and Cailletaud, 1995) have been used to define yield loci using a single specimen.

The back-extrapolation definition was used in the famous experiments of Taylor and Quinney (1931) to determine the multiaxial yield behavior of copper, aluminum, and mild steel. This method is often very difficult to apply because it requires near-linear hardening to facilitate the linear back-extrapolation. Furthermore, a large excursion into the plastic region is almost always necessary in order to achieve data that is linear enough to fit a straight line through, thus requiring multiple specimens to determine a single yield surface.

Another issue for multiaxial yield and flow experiments is whether to load using constant stress rate or constant strain rate. In earlier years this did not pose a problem since the only testing machines available were of the dead weight loading type. As servohydraulic testing machines were developed, it became possible to conduct tests using a constant strain rate. Phillips and Lu (1984) compared stress-controlled and strain-controlled loading paths to determine yield surfaces for pure aluminum using a servohydraulic testing machine. There appeared to be no difference between stress-controlled and

strain-controlled loading. Wu and Yeh (1991) suggest that using strain-controlled loading will produce more accurate results when using the offset strain definition of yielding, however this has not been confirmed experimentally.

The effect of strain rate on yielding behavior has also been investigated at room temperature. Ellis et al. (1983) studied the dependence of probing rate on the small-offset yield behavior of type 316 stainless steel at room temperature. Strain rates between 100 and 500 $\mu\text{m}/\text{min}$ appeared to have a negligible effect on the yield behavior. However, during preloading, where large excursions into the plastic range took place, a significant amount of creep was observed. Although classical plasticity theory assumes that deformation is rate-independent at room temperature, plastic deformation takes time to occur, especially at higher stresses (above the proportional limit). Furthermore, plastic deformation is always rate-dependent to some degree.

Experimental investigations to define the initial yield loci of metals date back to the work of Taylor and Quinney (1931). They found the von Mises yielding criterion (Eq. 2.6) described the initial yielding behavior of copper and aluminum in the axial-shear stress plane more accurately than the Tresca criterion (Eq. 2.3). Other experimental results for isotropic metals are in agreement (e.g., Phillips et al., 1972; Naghdi, 1958; Greenstreet, 1977; Liu, 1977; Helling et al., 1986).

The von Mises yield criterion appears to be adequate for describing the initial yield behavior of isotropic metals. However, experiments on metals with a crystallographic texture have shown that the yield loci can have anisotropic characteristics and may not be well described by the von Mises criterion. Texture can develop in metals as a result of large-scale deformation, such as during an extrusion process. Althoff and Wincierz (1972) found that the yield loci of textured brass and aluminum exhibited a unique dependence on texture only. Furthermore, the shape of the loci compared more favorably with formulations based on crystallographic calculations than with isotropic continuum yield criteria.

In addition to defining the initial yield behavior of metals, most researchers are also interested in determining how the yield surface changes due to a significant excursion into the plastic range. The two most basic hardening theories that were mentioned earlier, isotropic and kinematic hardening, attempt to describe how the yield surface changes as a result of changing material state. However, the majority of experimental results indicate that neither simplistic theory alone accurately describes the evolution of state. In fact, the shape of subsequent yield loci appear to be strongly dependent on the definition of yielding and target value that is employed.

When a small offset or proportional limit definition of yielding is used, the subsequent yield locus is translated away from the stress origin and

distorted. Naghdi et al. (1958) observed a region of high curvature near the preload point on the subsequent yield locus of aluminum preloaded in pure shear. In addition, a strong Bauschinger effect was indicated by a flattening of the surface in the region opposite the preload direction.

Small offset yield surface experiments by other researchers (e.g., Ivey, 1961; Phillips and Tang, 1972; Wu and Yeh, 1991) have resulted in results similar to those of Naghdi et al. However, in some cases a large *cross effect*, or an increase in the width of the yield surface in the direction normal to the preloading direction, has been observed. Williams and Svensson (1970; 1971) observed a large cross effect in aluminum after preloading in torsion, but very little cross effect after a tensile preload. On the contrary, Michno and Findley (1974) observed a negative cross effect (a decrease in the width) for mild steel.

When a large target value definition of yielding is used, the subsequent yield surface tends to expand isotropically. Hecker (1971), for example, subjected 1100-0 aluminum to combined axial loading and internal pressure, where yielding was defined using several definitions ranging from the proportional limit to 2000 $\mu\epsilon$ offset. For smaller definitions the subsequent yield surface exhibited a combination of isotropic, kinematic, and distortional hardening. However, the subsequent yield surface defined by an offset strain of 2000 $\mu\epsilon$ was observed to be an isotropic expansion of the initial yield surface.

Despite the differing experimental results on subsequent yield loci, one key feature that is consistently observed is normality of the plastic strain rate vector to the yield surface. Recall that Equation (2.10) demands this mathematically. It has also been confirmed experimentally for initial and subsequent yield loci by several authors (e.g., Michno and Findley, 1974; Phillips and Moon, 1977; Khan and Wang, 1993).

2.3 The Strength-Differential Effect in Metals

It is generally assumed that polycrystalline metals have the same yield strength in tension and compression. However, some high strength metals exhibit a significantly greater flow stress in compression than in tension. This phenomenon is known as the strength-differential (SD) effect. Many experimental and theoretical studies have been conducted in order to better understand the physical mechanisms that cause the strength-differential effect. Several hypotheses have been proposed to explain the behavior, such as microcracking, residual stresses, internal Bauschinger effect, particle-dislocation interactions, and volume expansion during plastic deformation. In this section a brief history of these investigations is presented. No attempt was made to reference every publication dealing with the strength-differential effect, however the following discussion provides a basic understanding of the topic.

Leslie and Sober (1967) were among the first to observe a strength-differential in martensitic steels. They found that untempered carbon martensite is significantly stronger in compression than in tension. Furthermore, the strength-differential appeared to increase with increasing carbon content. This unexplainable phenomenon soon became known as the strength-differential effect and led to a large amount of research in the 1970s.

Rauch and Leslie (1972) were among the first to propose that the strength-differential in steels is due to a volume expansion during plastic deformation. A volume expansion during plastic deformation is mathematically associated with an effect of hydrostatic stress on yielding. Furthermore, this produces a larger yield stress in compression than in tension. Volume is normally assumed to be conserved during plastic deformation in metals, however a volume expansion does readily occur during plastic deformation in plastics and granular media and causes a strength-differential in these materials (Drucker, 1973).

Experimental investigations into the effect of hydrostatic stress on plastic deformation have indicated that some metals are hydrostatic stress dependent, however a permanent change in volume was not always observed. Spitzig et al. (1975) have reported that the yield strength of quenched AISI 4310 and 4330 steels increased evenly in both tension and compression as a function of increasing hydrostatic pressure. Furthermore, a permanent volume change

was detected and found to be proportional to the plastic strain. It was suggested that the change in volume was due to a large increase in the dislocation density. Consequently, a strength-differential effect of approximately 6% was observed for both steels that appeared to be independent of increases in plastic strain and hydrostatic pressure. Spitzig et al. proposed a modified yield function that is dependent on the hydrostatic stress and the second and third deviatoric stress invariants.

Rauch et al. (1975) agree that a significant generation of dislocations would lead to a volume change, especially in aged materials where preexisting dislocations are immobilized by precipitates. However, their experimental results for tempered AISI 4310, 4320, and 4330 steels disagree with the notion of a permanent volume change. They found that the application of hydrostatic pressure had a greater effect on the compressive yield strength than on the tensile yield strength and no evidence of a permanent volume expansion was observed. It was also observed that the strength-differential effect increases with decreasing test temperature and decreases with increasing test temperature.

Another theory for the strength-differential effect was reported by Hirth and Cohen (1970) involving nonlinear elastic strains that contribute to a seemingly higher flow stress in compression than in tension. Hirth and Cohen suggest that the distortion in the lattice that occurs in the vicinity of a solute

atom can lead to local elastic strains that are nonlinear. This would inevitably alter the atomic force-displacement relationships such that they would be different for tension and compression. Kalish and Cohen (1969) suggest that the nonlinear elastic strain hypothesis can also apply to the coherency strains around precipitated particles. This suggestion is supported by the results of Chait (1973), who tested three Ti alloys in the aged condition and found that coherent precipitation contributes to the strength-differential effect. Similar results for Ti alloys have been reported by Winstone et al. (1973). Chait suggested that the strength-differential effect arises from interactions between dislocations and the strain field around precipitate particles. Furthermore, it was suggested that alloys for which the precipitates are not coherent with the matrix could show a smaller strength-differential effect.

Pampillo et al. (1972) added to the theory of Hirth and Cohen by suggesting that the nonlinear elastic behavior would lead to a change in the instantaneous elastic moduli at sufficiently large elastic strains. The change occurs such that the elastic modulus decreases in tension and increases in compression. The strength-differential effect is then due to an increase of the internal stress in compression and a decrease of the internal stress in tension as a result of the changes in the elastic modulus. This hypothesis is in agreement with Rauch and Leslie (1972), who reported that the elastic modulus

of martensitic AISI 4320 steel was consistently 1-3.5% less in tension than in compression.

Olsen and Ansell (1969) proposed a different theory for the strength-differential effect in two-phase alloys. A Nickel alloy with a 2% by volume dispersion of ThO_2 particles tested at room temperature showed a 0.2% offset yield strength that was 30% higher in compression than in tension. It was suggested that the formation of voids at the particle-matrix interface during tensile loading results in a lower yield strength in tension than compression. The particle-matrix decohesion during tension permits dislocation annihilation, thus lowering the stress needed for particle bypass and consequently lowering the yield strength in tension. An aluminum alloy with a 2% by weight dispersion of alumina (Al_2O_3) was also tested that did not show a strength-differential effect at 0.2% offset yield. However, the proportional limit in compression was observed to be approximately 30% higher than in tension. This was assumed to be due to residual elastic strains.

The theory proposed by Olsen and Ansell applies to two-phase alloys that exhibit a weak bond between the particles and the matrix. Aluminum- Al_2O_3 are known to exhibit very good bonding characteristics. Thus, this could explain why there was no strength-differential observed for this alloy. On the contrary, Mannan and Rodriguez (1973) observed that the strength-differential effect in a zirconium alloy increased with increasing interstitial content,

however no decohesion was observed between the matrix and second-phase interstitial atoms. This suggests that the strength-differential effect may be due to different mechanisms in different materials.

In summary, the experimental results suggest that a microstructure containing interstitial solute atoms or precipitate particles is a prerequisite for the strength-differential effect. None of the proposed models adequately accounted for the strength-differential effect in all of the materials tested, however the exact mechanism leading to the strength-differential may be different depending on the microstructure of the material. The most promising theories appear to be the volume expansion and particle-dislocation interaction hypotheses. In most cases both theories underestimate the observed strength-differential effect, thus it is possible that both mechanisms contribute to this effect. The other proposed theories, such as the internal Bauschinger effect and the microcracking hypothesis, suggest that the strength-differential effect will decrease with increasing plastic strain, which was not generally observed in the experiments.

CHAPTER 3

EXPERIMENTAL AND MATERIAL DETAILS

The experimental procedure and test equipment is of critical concern for elevated temperature yield and flow surface experiments. Precise strain measurement is crucial for detecting the small strain offsets necessary in mapping out yield and flow surfaces using a single specimen. This chapter begins by discussing the material and specimen details in section 3.1. Section 3.2 provides an overview of the test equipment. Finally, in section 3.3 the issues of the experimental methods are discussed.

3.1 Material and Specimen Details

The wrought Inconel 718 superalloy used in this study was obtained in the form of extruded 31.8 mm diameter bars, all from the same heat. The composition is listed in Table 3.1. The bars were machined into tubular specimens having the final dimensions shown in Figure 3.1. After machining, the specimens were solutioned at 1038°C in argon for 1 hour and air cooled. Select specimens were further heat-treated as follows: aged at 720°C in argon for 8 hours, cooled at 55°C/hour to 620°C and held for 8 hours, then air cooled

Element	Content (wt.%)
Ni	53.58
Cr	17.52
Mo	2.87
(Nb+Ta)	5.19
Ti	0.95
Al	0.57
Co	0.39
C	0.034
S	0.002
Mn	0.120
Si	0.070
B	0.004
Cu	0.050
P	0.006
Fe	Bal.

Source: Teledyne Allvac.

Table 3.1 - Material composition of Inconel 718.

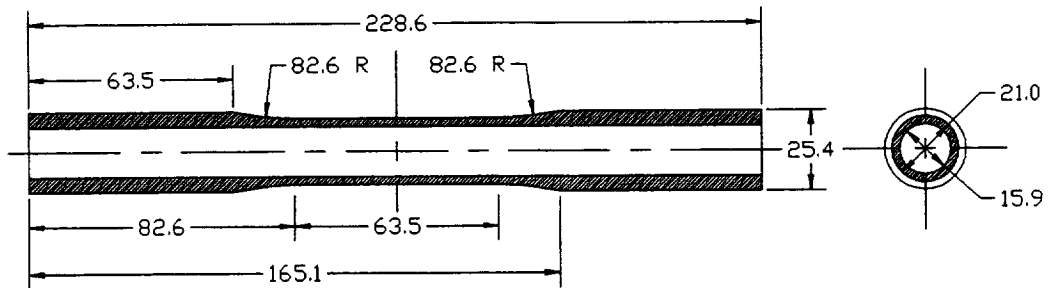


Figure 3.1 - Typical specimen geometry showing longitudinal and transverse cross sections (all dimensions are in millimeters).

to room temperature. Throughout this work, the two material states will be referred to as simply *solutioned* and *aged*.

Metallography was performed on transverse and longitudinal sections taken from the grip ends and from the gage sections of both solutioned and aged tubes. The polished specimens were etched using Tucker's reagent (45 mL HCl, 25 mL H₂O, 15 mL HNO₃, and 15 mL HF) to reveal the grain structure (Fig. 3.2). No difference was observed between the grip ends and the gage sections. Furthermore, both the solutioned and the aged microstructures appeared similar. The grain structure consisted of equiaxed grains having an ASTM grain size of 4 (90 μ m in diameter). Carbide particles were observed throughout the microstructure.

Microhardness was also measured on the metallographic samples. The solutioned samples had a Vicker's Hardness of 180 (Rockwell B of 89) and was much softer than the aged samples, which had a Vicker's Hardness of 440 (Rockwell C of 45).

Transmission electron microscopy was performed on the solutioned and aged IN718. The aged material was observed to have a fine dispersion of γ'' precipitates with a preferred orientation within a particular grain (Fig. 3.3). The precipitate particles were observed to be platelets approximately 10-15 nm in length. Texture analysis was also performed, which showed there to be no preferred grain orientation. Thus, the preferred orientation of the precipitates

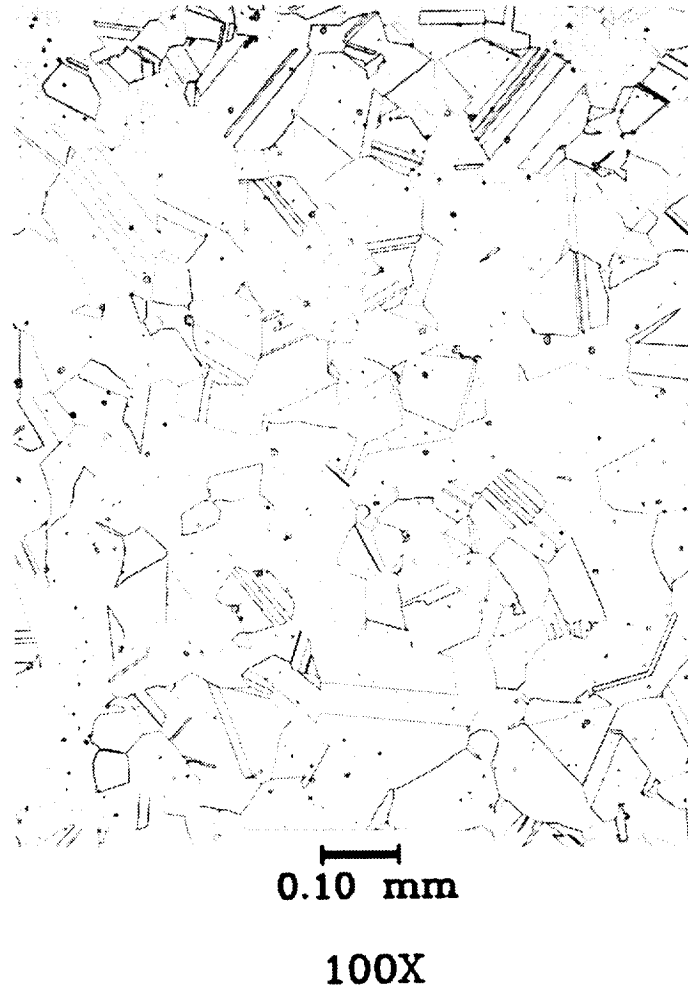


Figure 3.2 - Optical microstructure of solutioned Inconel 718. The microstructure for aged Inconel 718 was similar.

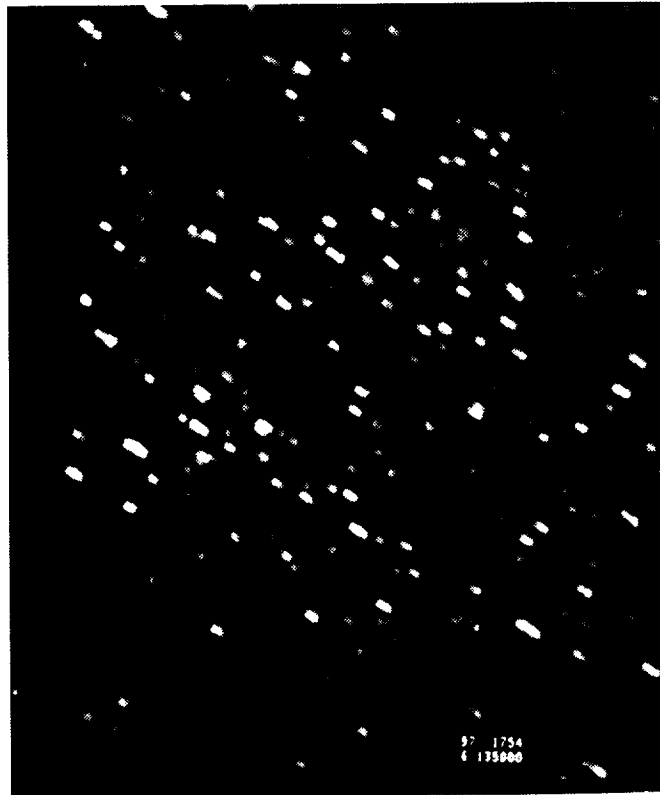


Figure 3.3 - Transmission electron microscopy of aged Inconel 718 showing precipitation.

within the grain is not expected to cause anisotropic behavior in the aged IN718. The solutioned IN718 did not show any precipitation.

3.2 Test Equipment

The experiments were performed on a computer controlled MTS biaxial servohydraulic test machine capable of applying an axial load of $\pm 222,000$ N and a twisting moment of $\pm 2,260$ N·m (Fig. 3.4). The specimen was held in place by water-cooled, hydraulically actuated grips. The top grip remained fixed throughout a test while the bottom grip is attached to an actuator capable of independent rotation and vertical translation. Two MTS 458 analog controllers (one for axial and one for torsion) were used to control the motion of the actuator. Additional details regarding the biaxial test machine are provided by Kalluri and Bonacuse (1990).

The test machine is equipped with a closed-loop induction heating system (Ellis and Bartolotta, 1997) capable of specimen temperatures in excess of 800°C . The system consists of a 5-kW Ameritherm radiofrequency induction heating unit and three adjustable, water-cooled copper coils that surround the gage section of the specimen (Fig. 3.5). The specimen temperature is controlled by spot welding one thermocouple to the gage section of the specimen. Three additional thermocouples were spot welded to

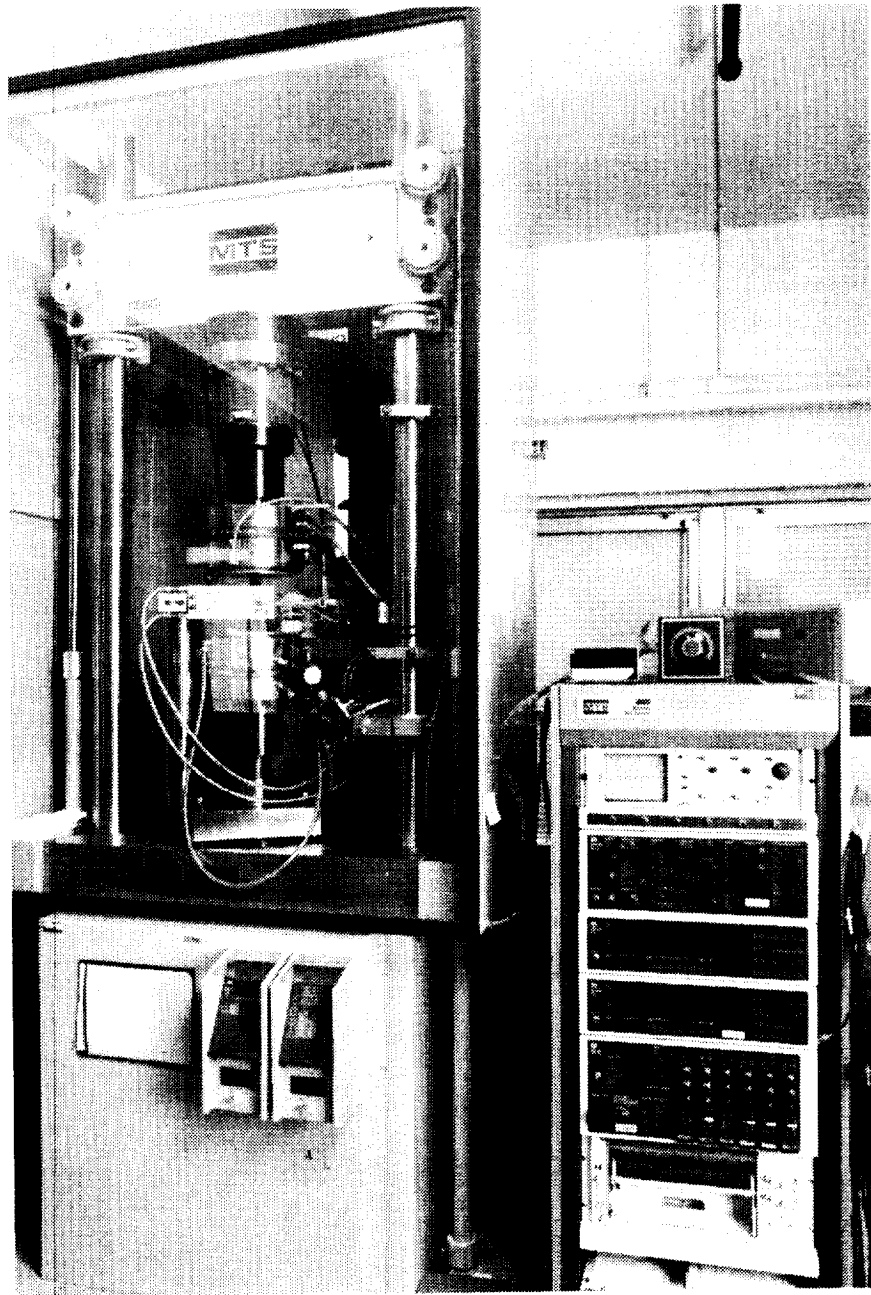


Figure 3.4 - Servohydraulic test machine and electronics.

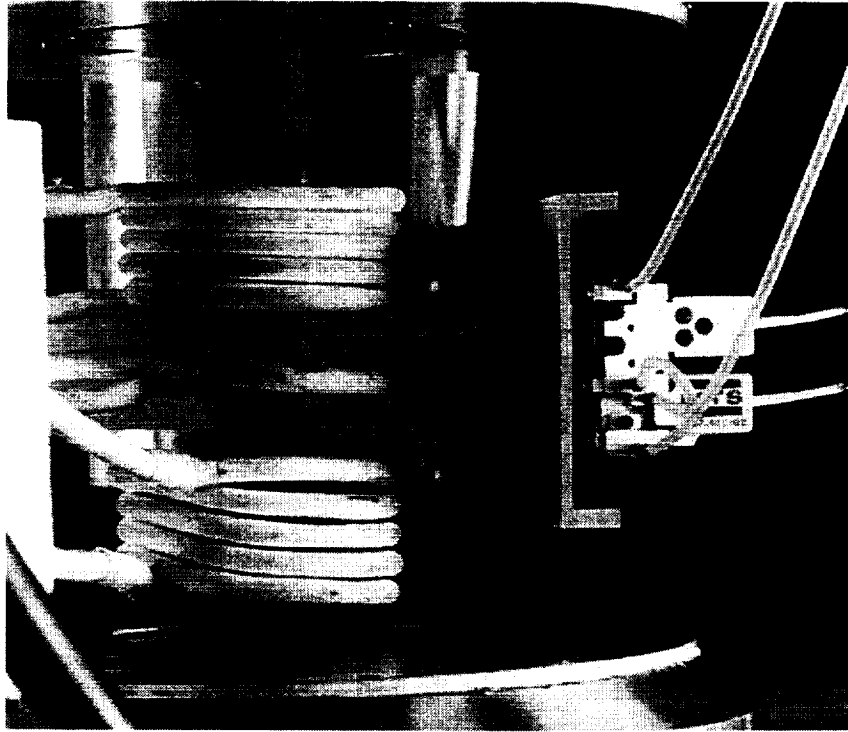


Figure 3.5 - Close-up of specimen, extensometer, and heating coils.

the specimen to help achieve an acceptable gradient ($\pm 1\%$ of the absolute test temperature).

The ability to measure very small increments of strain (precise to the microstrain level) is necessary for yield surface experiments, since the goal is to detect yielding and then unload the specimen before significant permanent deformation occurs. Furthermore, the strain measurement device must maintain this level of performance for a wide range of specimen temperatures. This is especially difficult at elevated temperatures, where large amplitude electronic noise can hinder high resolution strain measurement.

In this investigation, axial and shear strains were measured using an MTS water-cooled biaxial extensometer (model no. 632.68C-05) that is capable of operating over a large temperature range. (The precision of the extensometer at different temperatures is discussed in Chapter 4.) The extensometer (Fig. 3.5) uses two high-purity alumina (Al_2O_3) rods, spaced 25 mm apart, to precisely measure axial deformation and twist. Lissenden et al. (1997) have supplied more details on the biaxial extensometer.

For transverse strain measurement, a diametral extensometer was employed. The diametral extensometer is similar to the biaxial extensometer in appearance, although it contains longer rods that fit on either side of the gage section of the specimen to directly measure the change in diameter.

Transverse strains were measured to determine Poisson's ratio (which will be

used to calculate the equivalent strain rate) and to determine whether Poisson's ratio changes during the course of a yield locus probe.

3.3 Experimental Procedure

All of the experiments were conducted in strain control using an equivalent strain rate of $10 \mu\epsilon/\text{sec}$ (10^{-5} s^{-1}). For axial-torsional loading the equivalent strain rate reduces to

$$\dot{\epsilon}_{eq} = \sqrt{\frac{2}{3} \dot{\epsilon}_{ij} \dot{\epsilon}_{ij}} = \sqrt{\frac{2}{3} [(1 + 2\nu^2) \dot{\epsilon}_{11}^2 + 2\dot{\epsilon}_{12}^2]} \quad (3.1)$$

where $\dot{\epsilon}_{ij}$ is the strain rate tensor, ν is Poisson's ratio, and $\dot{\epsilon}_{11}$ and $\dot{\epsilon}_{12}$ denote the axial and shear strain rates, respectively. Substituting the elastic Poisson's ratio ($\nu = 0.34^*$) into Equation (3.1) gives

$$\dot{\epsilon}_{eq} = \sqrt{(0.906)^2 \dot{\epsilon}_{11}^2 + \frac{4}{3} \dot{\epsilon}_{12}^2} \quad (3.2)$$

The elastic Poisson's ratio was used since most of the loading was elastic.

Custom written software and a personal computer, equipped with analog-to-digital (A/D) and digital-to-analog (D/A) conversion hardware, were used to control the experiments. The D/A hardware was commanded to send strain increment data to the electronic controller 1000 times per second. Similarly, the A/D hardware collected load, torque, and strain data from the controller at 1000 Hertz. Every 100 data points were averaged to help

* Measured at 23°C and confirmed by (Abdel-Kader et al., 1986).

minimize the effect of electronic noise, which resulted in a maximum of 10 data points per second being written to a file.

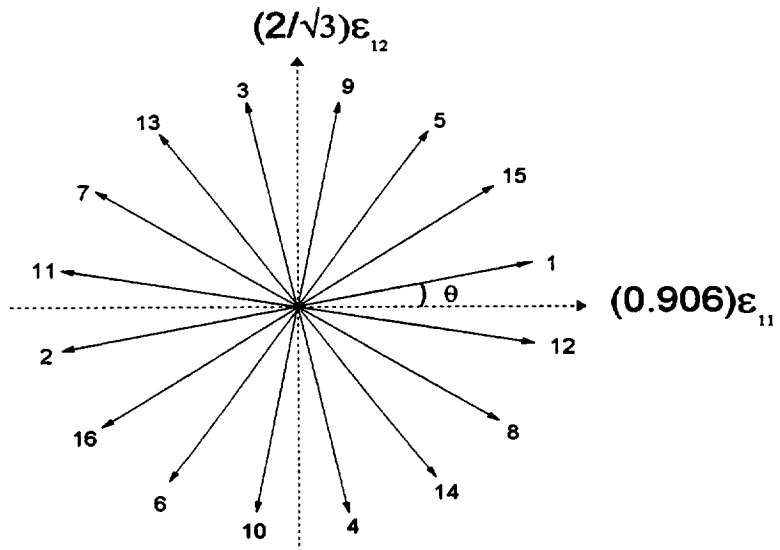
Two different software programs were developed for controlling the experiments. One program was used to determine the individual yield points that were used to map out initial and subsequent yield loci and the other program performed the radial prestrains.

3.3.1 Yield Loci

Each locus was determined by straining the specimen in 16 unique directions, according to a specified angle in equivalent axial-torsional strain space (Fig. 3.6). The order in which the probes were conducted was chosen to minimize changes to the material state. For example, Figure 3.6 shows that each even-numbered probe was in the opposite direction from the preceding odd-numbered probe. By using this sequence it was hoped to counter balance the effects of the previous probe. Furthermore, each surface was repeated at least once to ensure that the results were repeatable and to verify that the material state remained practically undisturbed.

Each point on the yield locus was determined using the following procedure:

- Calculate the coefficients of the axial and shear elastic loading lines (E , σ_{11}^o , G , and σ_{12}^o) over a predefined strain range during the initial (assumed to be linear elastic) portion of the loading using a least squares regression



Probe Number	Probe Angle	Probe Number	Probe Angle
1	12°	9	79°
2	192°	10	259°
3	102°	11	170°
4	282°	12	350°
5	57°	13	125°
6	237°	14	305°
7	147°	15	35°
8	327°	16	215°

Figure 3.6 - Probe directions used in determining a yield locus.

technique (Fig. 3.7). E and G are the axial and shear moduli; σ_{11}^o and σ_{12}^o are the axial and shear prestresses.

- Continually calculate the offset strain components (Fig. 3.7)

$$\varepsilon_{11}^{off} = \varepsilon_{11} - \frac{\sigma_{11} - \sigma_{11}^o}{E} \quad (3.3)$$

$$\varepsilon_{12}^{off} = \varepsilon_{12} - \frac{\sigma_{12} - \sigma_{12}^o}{2G} \quad (3.4)$$

where σ_{11} , σ_{12} are the axial and shear stresses and ε_{11} , ε_{12} are the axial strain and tensorial shear strain ($\varepsilon_{12} = \frac{1}{2} \gamma_{12}$).

- When the equivalent offset strain,

$$\varepsilon_{eq}^{off} = \sqrt{(\varepsilon_{11}^{off})^2 + \frac{4}{3}(\varepsilon_{12}^{off})^2}, \quad (3.5)$$

reaches the target value (usually $30 \mu\varepsilon$), write the current stress values (axial and shear) to an output file, unload the specimen and then begin the next probe.

Equation (3.5) defines the equivalent offset strain (also Eq. 2.17), which was derived from an equation similar to Equation (3.1). A Poisson's ratio of 0.5 was used, assuming plastic incompressibility. Although the incompressibility condition may not be met for small offset strains, this relationship for the equivalent offset strain has been traditionally used by researchers for determining yield loci (e.g., Wu and Yeh, 1991; Khan and Wang, 1993; Lissenden et al., 1997). Additionally, the equivalent offset strain refers to an

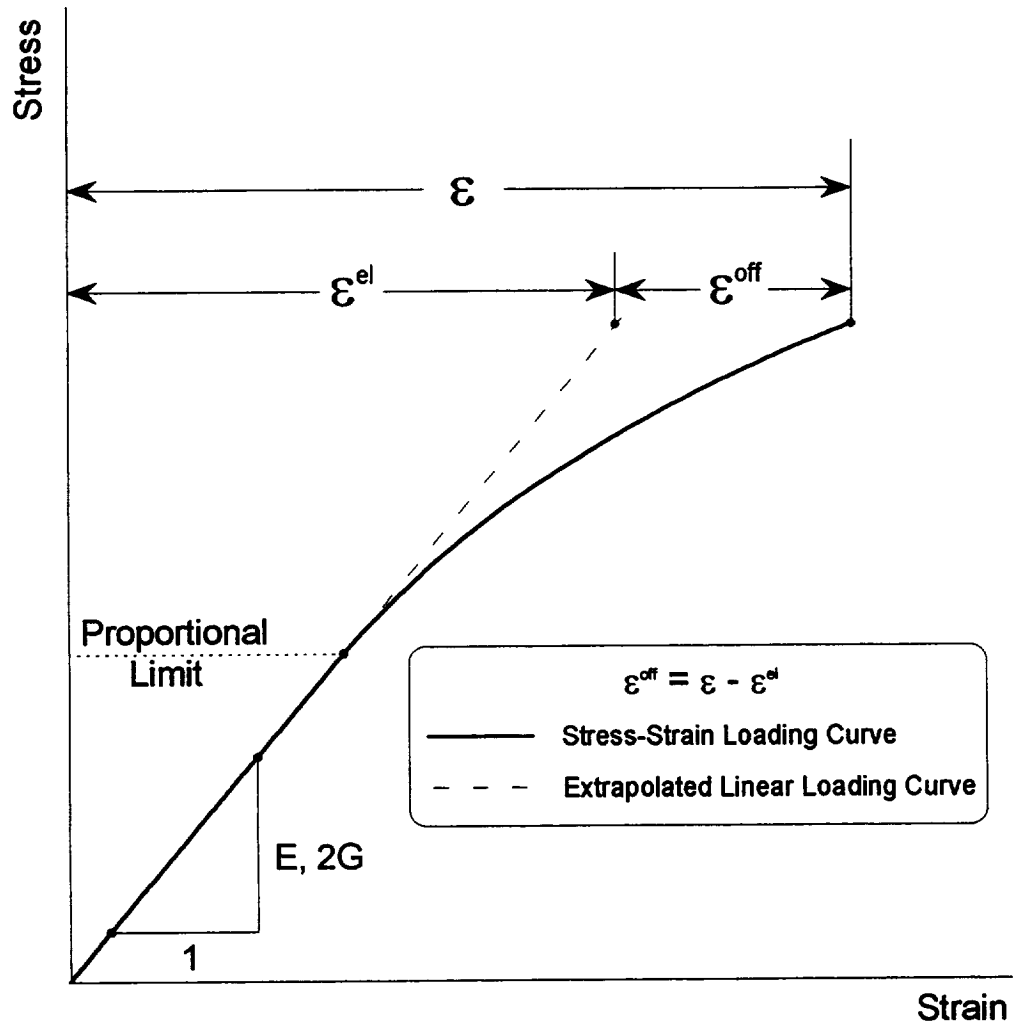


Figure 3.7 - Calculation of E, G, and ϵ^{off} during experiments.

offset during loading and does not necessarily have the same magnitude as the permanent set.

3.3.2 Radial Prestraining

After determining the initial yield loci, the specimens were subjected to radial prestraining at elevated temperature (except in one case cyclic radial prestraining at room temperature was applied). Two radial prestrain paths were used. One path was combined tension-torsion, corresponding to an angle of $\angle 45^\circ$ in equivalent strain space (Fig. 3.8a). This was nearly equivalent to a $\angle 45^\circ$ path in equivalent stress space (Fig. 3.8b). The maximum prestrain point was determined by detecting a particular value of equivalent offset strain. The other prestrain path consisted of straining the specimen in pure tension until a predefined total axial strain was achieved.

The same procedure was followed for both strain paths and is outlined in the following.

- The stress-free specimen was heated to the desired temperature.
- After several minutes at the target temperature, the specimen was strained until the target prestrain value was achieved (point A_1 (or B_1) in Fig. 3.8).

The mode was switched from strain control to load/torque control and the specimen was held at constant stress for several minutes. During this time creep strains were monitored on X-Y plotters and recorded by the data acquisition software.

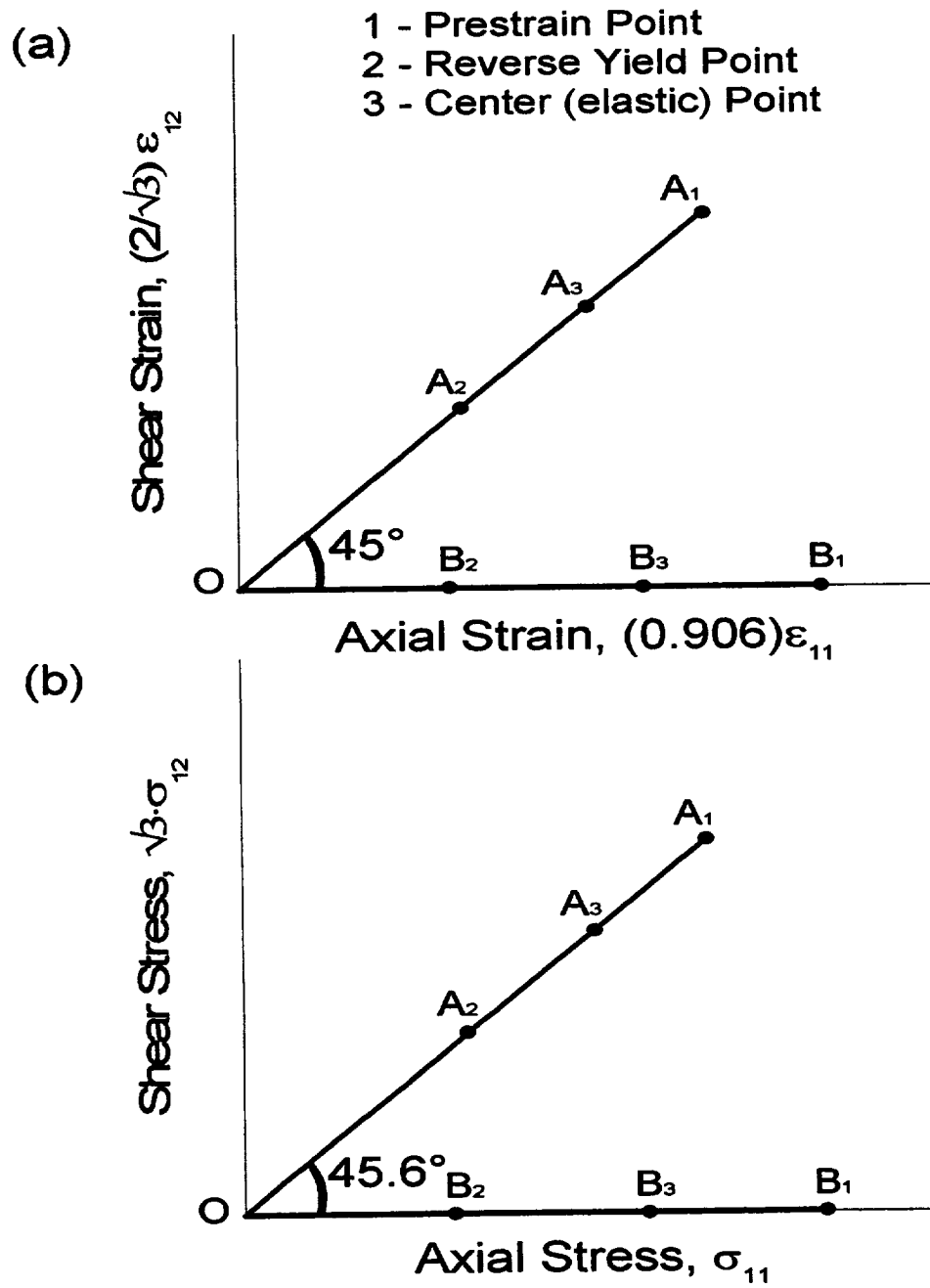


Figure 3.8 - Prestrain paths shown in (a) equivalent strain space, and (b) equivalent stress space.

- After several minutes, the control mode was switched back to strain control. The reverse yield point was found (point A_2 (or B_2) in Fig. 3.8) by unloading the specimen until the equivalent offset strain exceeded the target value.
- The specimen was reloaded to a point (point A_3 (or B_3) in Fig. 3.8) midway between the prestrain point and the reverse point. The subsequent yield locus was then determined using this point as the probe origin.

CHAPTER 4

EXPERIMENTAL RESULTS AND DISCUSSION

This chapter presents and discusses the initial and subsequent yield loci results for Inconel 718. In section 4.1 several preliminary issues are resolved experimentally using solutioned IN718, followed by some initial and subsequent yield loci at 23, 371, and 454°C. Section 4.2 provides results for aged IN718 at 23 and 649°C. Finally, in section 4.3 some initial yield loci are presented for re-solutioned IN718 specimens.

4.1 Solutioned Inconel 718

When using the offset strain definition of yielding it is important to relate the offset strain during loading to the permanent set that is measured after unloading is complete. In an attempt to compare these two quantities, the offset strain for a small offset tension test was plotted versus the total axial strain (Fig. 4.1). The offset strain accumulates to approximately 30 $\mu\epsilon$ during loading and continues to increase during unloading to a total offset of approximately 44 $\mu\epsilon$.

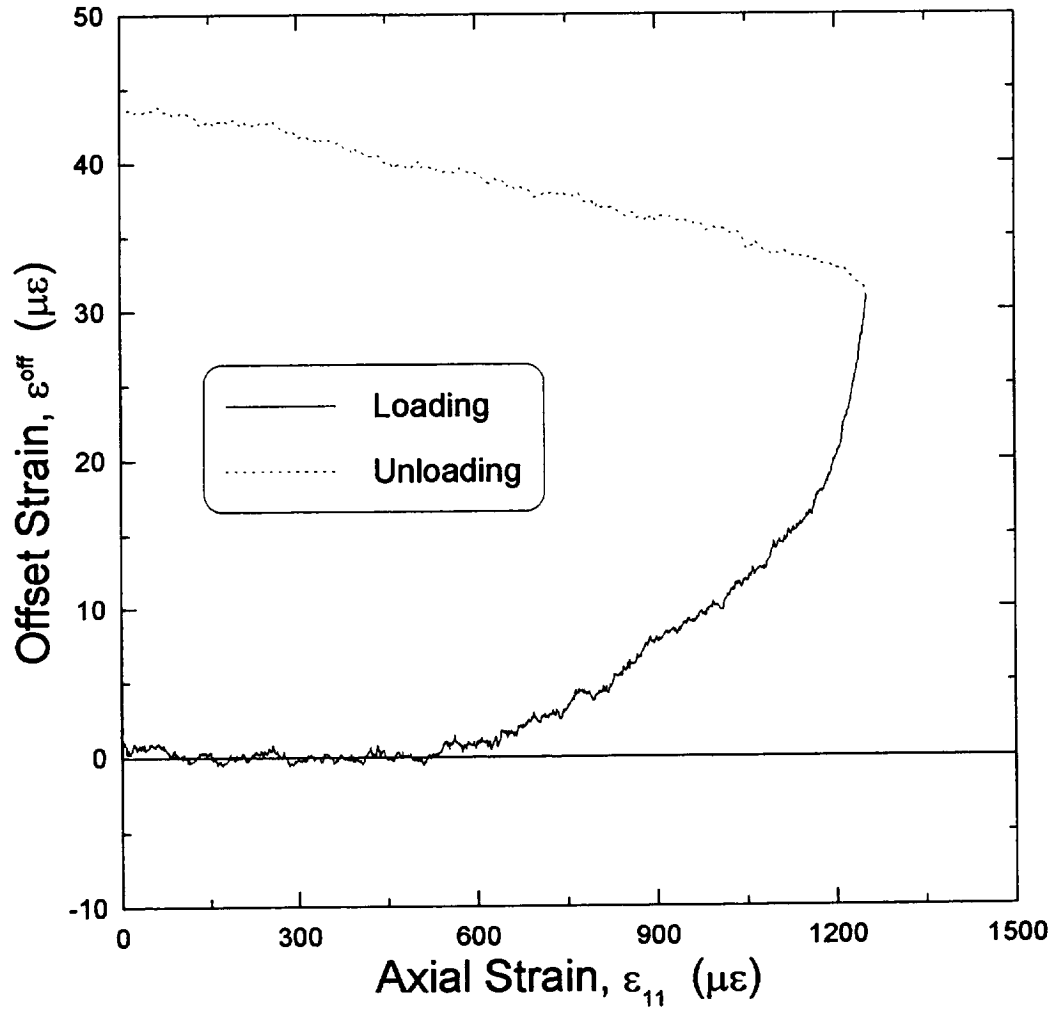


Figure 4.1 - Offset strain versus strain during tensile loading for solutioned IN718.

The discrepancy between the offset strain during loading and the offset after unloading is believed to be due to inaccuracy of the extensometer after a load reversal, rather than true material behavior. Data from previous tests (Lissenden et al., 1997) were analyzed, where an extensometer and strain gages were both used to measure strain. A comparison of strain data obtained from the extensometer and from the strain gages showed that there was good agreement between the two measurement devices during loading. However, after the load reversal the extensometer strains did not always agree well with those from the strain gages, particularly for shear strains. This suggests that strains measured by the extensometer during loading are accurate, but that a correlation between the offset strain and permanent set cannot be made.

After confirming that the extensometer was accurately measuring the offset strain, specimen IN-15 was used to determine which control mode, stress or strain, gave more consistent results at 23°C. Phillips and Lu (1984) investigated the yield behavior of aluminum using stress and strain controlled loading, however a direct comparison of the results was not shown. In this preliminary work the size and shape of the yield locus using stress and strain control were compared. Since the goal was to detect a small target offset strain (calculated from measured stress and strain), it was important to determine if there was more or less scatter in the results for strain control compared to stress control.

Initial yield loci for specimen IN-15 were determined under stress and strain controlled loading at room temperature. In these tests the target value was an equivalent offset strain of $20 \mu\epsilon$. The resulting loci are plotted in the modified normal-shear stress plane ($\sqrt{3}\sigma_{12}-\sigma_{11}$) in Figure 4.2. Clearly the control mode had little effect on the data. Repetitive tests were made to verify this result. Strain control was used for the remaining experiments to be consistent with prestraining.

Next, the elastic Poisson's ratio (which was needed for Eq. 3.1) was determined during a tensile probe by measuring the diametral strain. Specimen IN-9 (a virgin specimen) was tested in tension until a $10 \mu\epsilon$ offset was reached. Figure 4.3 shows the diametral strain (ϵ_{22}) plotted versus the axial strain (ϵ_{11}). The slope of Figure 4.3, which is the Poisson's ratio, is 0.34 and remains constant up to the load reversal. This suggests that the elastic Poisson's ratio ($\nu = 0.34$) may also be more appropriate (rather than $\nu = 0.5$ which implies plastic incompressibility) for use in Equation (3.5) when performing small offset yield experiments.

Experimental data from specimen IN-6 (discussed later in detail) was reduced to examine the effect of using two different values for Poisson's ratio (0.25 and 0.5) to determine yield loci. That is, the equivalent offset strain was defined by

$$\epsilon_{eq}^{off} = \sqrt{\frac{3}{4}(\epsilon_{11}^{off})^2 + \frac{4}{3}(\epsilon_{12}^{off})^2} \quad (4.1)$$

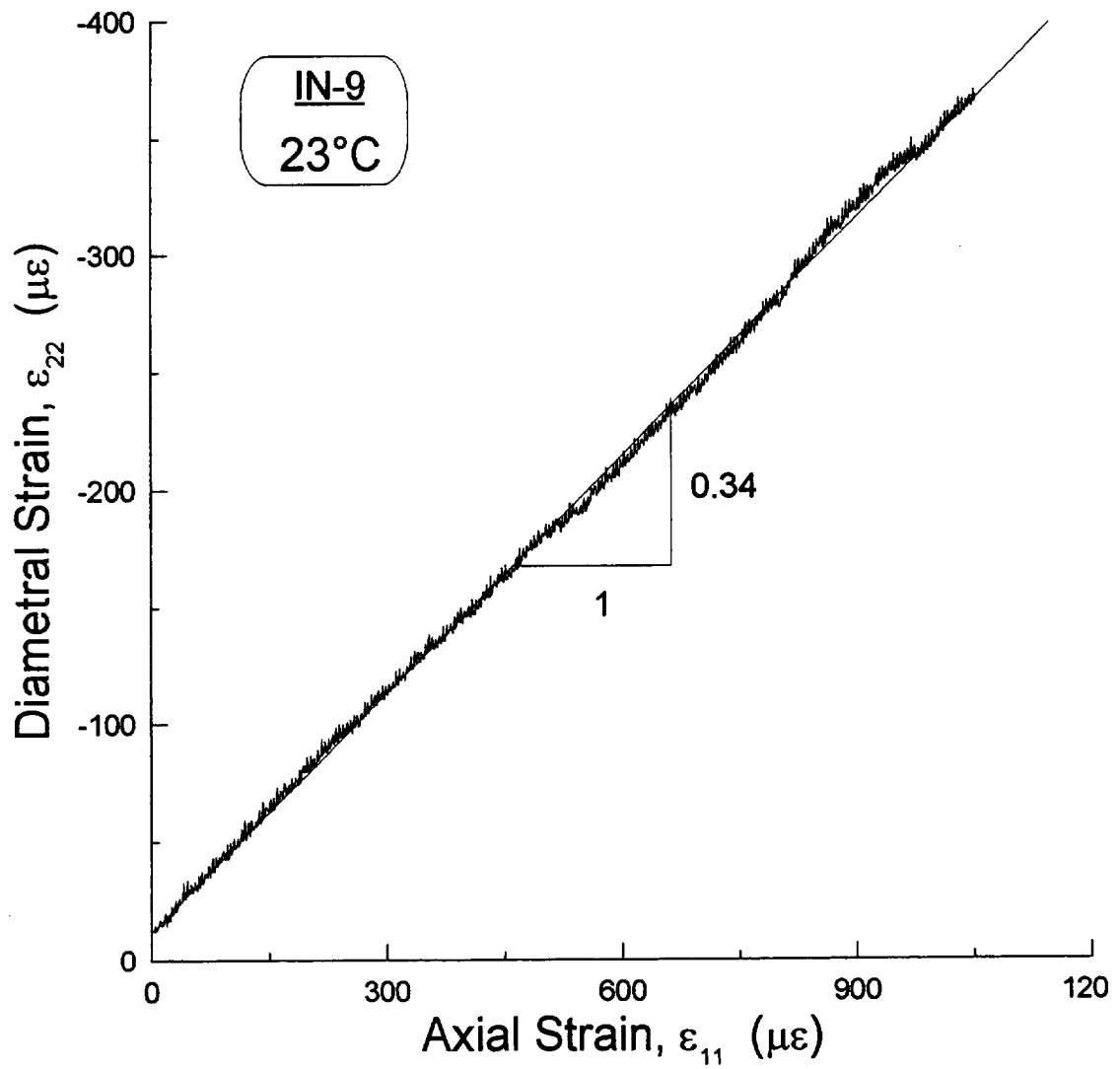


Figure 4.3 - The slope of the diametral strain versus axial strain gives a Poisson's ratio of 0.34.

for $\nu = 0.25$, and by

$$\varepsilon_{eq}^{off} = \sqrt{(\varepsilon_{11}^{off})^2 + \frac{4}{3}(\varepsilon_{12}^{off})^2} \quad (4.2)$$

for $\nu = 0.5$. A target value of $25 \mu\varepsilon$ was used for each definition and the results are plotted in Figure 4.4. The data appears to be relatively insensitive to variations in Poisson's ratio between 0.25 and 0.5. This suggests that substitution of the elastic Poisson's ratio ($\nu = 0.34$) into Equation (3.4) would not change the results.

The effect of using target values between 10 and $30 \mu\varepsilon$ to determine yield loci was examined next. Three loci were determined for each target value (with the exception of $30 \mu\varepsilon$, where only two loci were determined) to judge repeatability (Fig. 4.5). The results were repeatable for each target value. This demonstrates that each of these target values are small enough to avoid a significant change to the material state. A target value of $30 \mu\varepsilon$ was chosen for the remaining experiments in order to obtain a maximum amount of offset strain data to analyze in terms of rate-dependent flow definitions (see Chapter 6). Additionally, at elevated temperatures electronic noise decreases the resolution of the measured strain, making a larger target value more practical.

The strain rate dependence of solutioned IN718 at room temperature was also investigated. In the past, researchers have chosen to use very slow strain rates to allow time for the plastic strain to fully develop. Therefore, it was

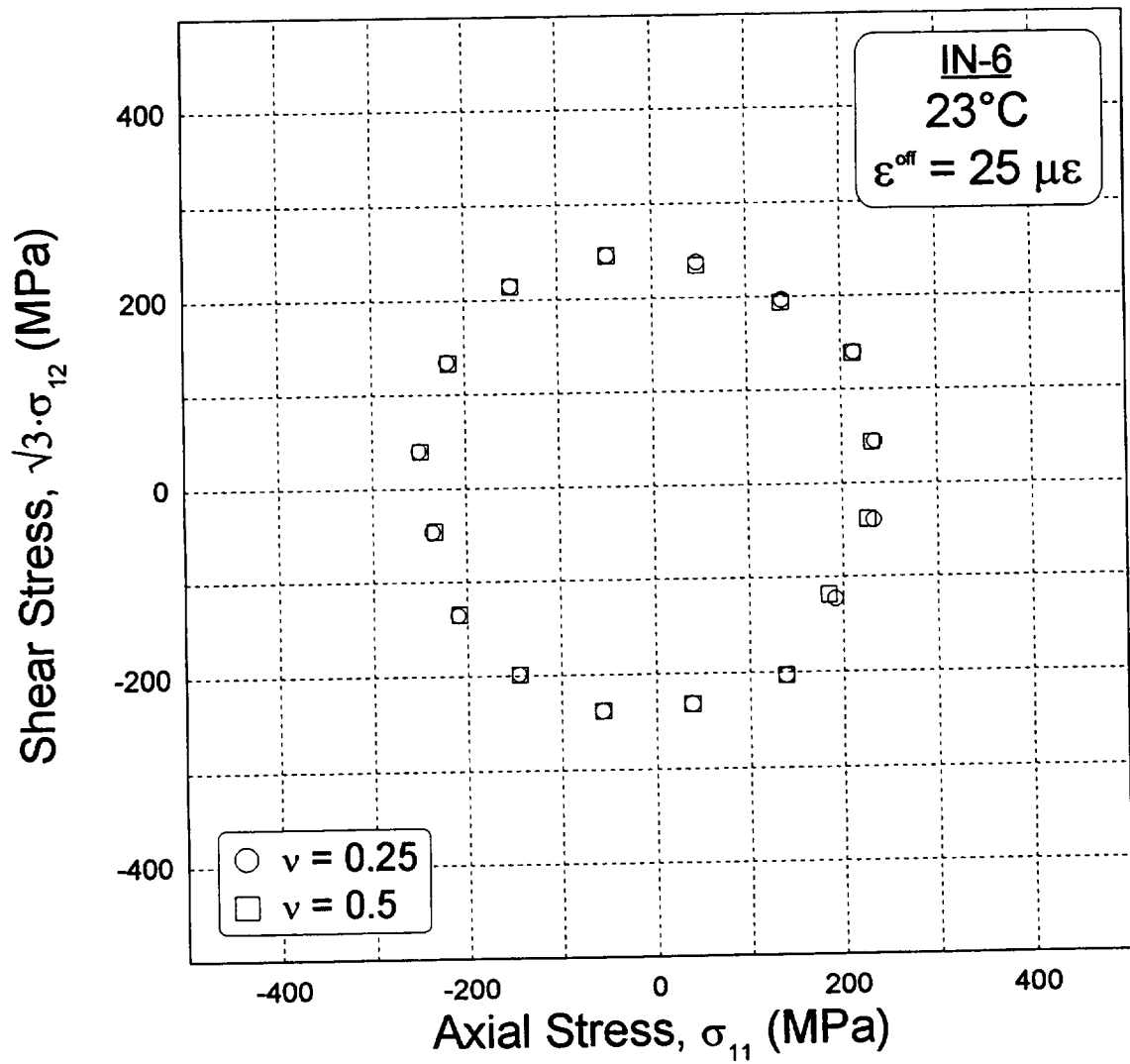


Figure 4.4 - Effect of using different values for Poisson's ratio to define the equivalent offset strain.

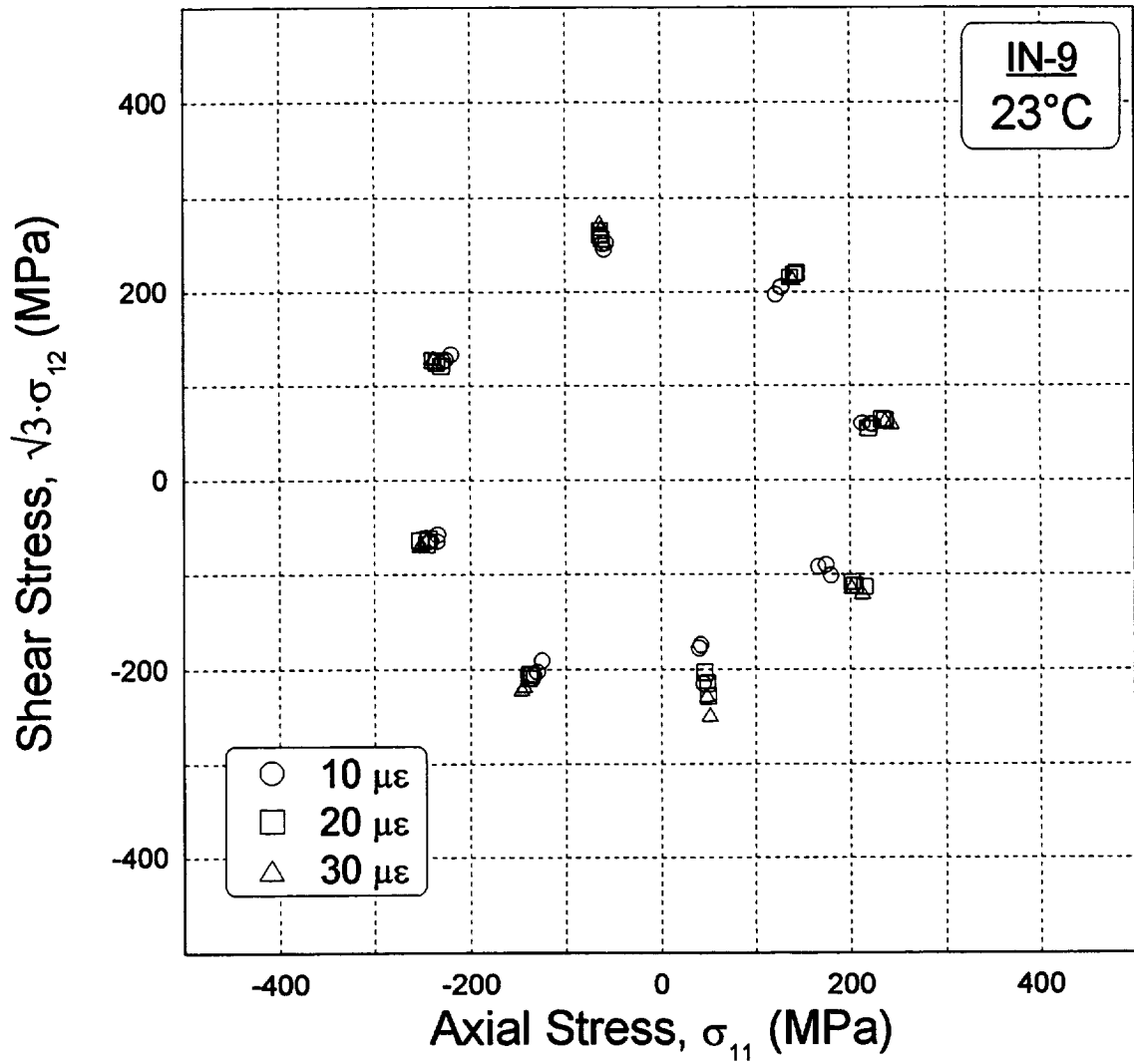


Figure 4.5 - Yield loci for solutioned IN718 defined by target values of 10, 20, and 30 $\mu\epsilon$ equivalent offset.

important to verify that the procedure outlined in Chapter 3 was applicable for a range of strain rates. This was done by determining yield loci using strain rates of 2, 10, and 20 $\mu\text{s}/\text{sec}$. The results were nearly identical for each strain rate, indicating that this small-scale plastic deformation had adequate time to occur for each strain rate.

After these preliminary issues were resolved, the initial yield behavior of solutioned IN718 was investigated at 23°C using two virgin specimens (IN-6 and IN-25). There was remarkably very little specimen-to-specimen scatter between the initial loci (Fig. 4.6). Furthermore, each specimen showed repeatable results, suggesting that the change in material state associated with detecting each yield point was insignificant.

The von Mises and Tresca yield criteria, discussed in Chapter 2, are compared with the experimental data in Figure 4.6. A modified axial-shear stress plane ($\sqrt{3}\cdot\sigma_{12}-\sigma_{11}$) is used so that the von Mises criterion plots as a circle. The von Mises circle, centered at the stress plane origin with a radius of 248 MPa, fits the data well. The Tresca ellipse provides a more conservative prediction of yielding when torsional loads are present.

Before investigating the initial yield behavior at elevated temperature the electronic noise in the strain signals at elevated temperature was compared to readings taken at room temperature (Fig. 4.7). The peak-to-peak amplitude of the electronic noise was well below 1 μs for both axial and shear strain at room

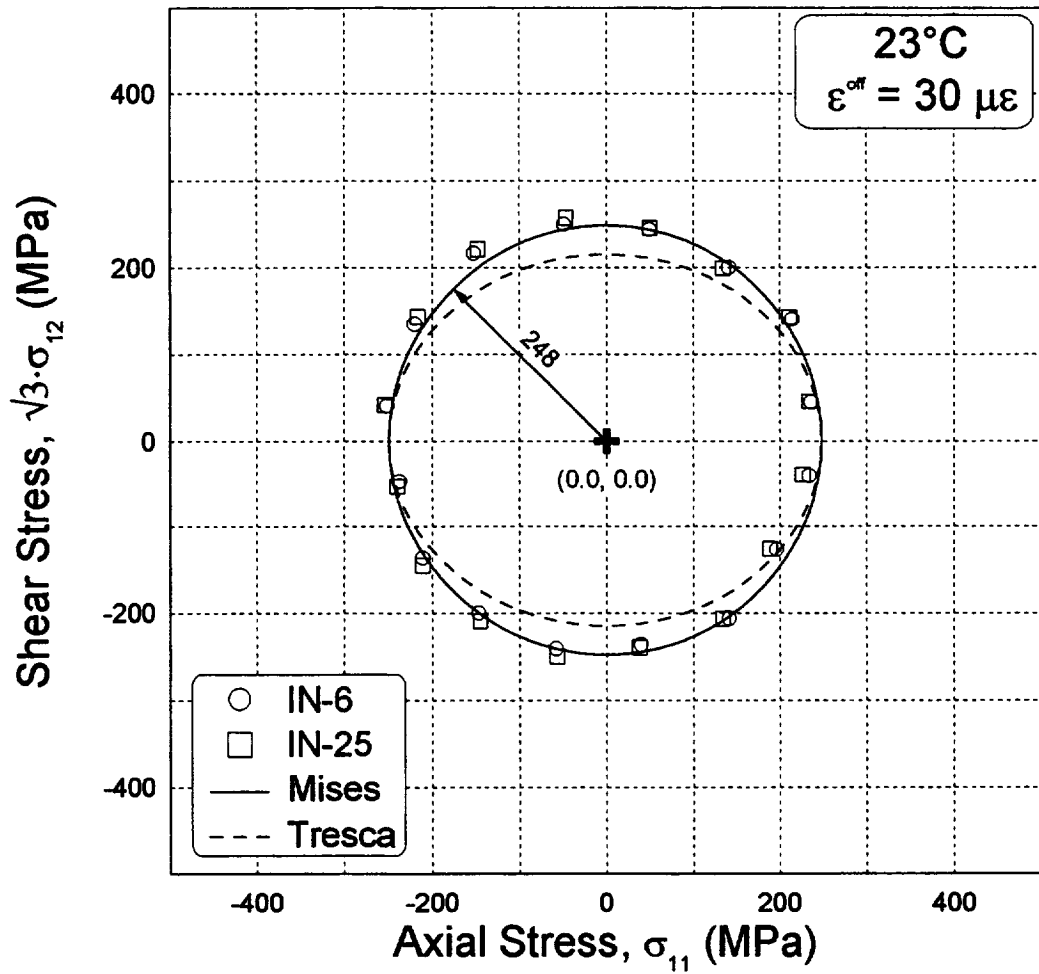


Figure 4.6 - Initial yield loci for solutioned IN718 at room temperature. The von Mises and Tresca yield criteria are also shown.

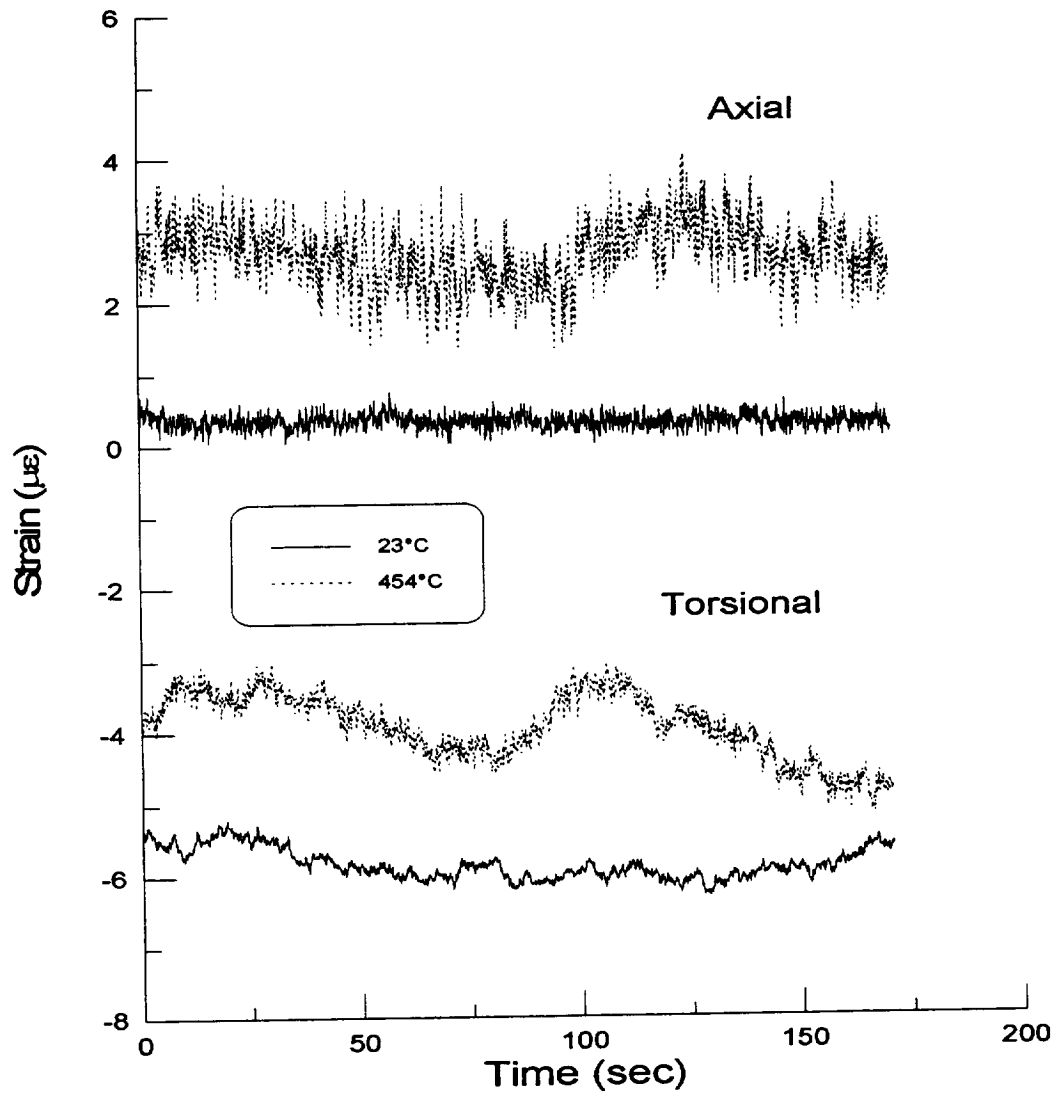


Figure 4.7 - Comparison of electronic noise at 23 and 454°C.

temperature. At elevated temperature (454°C), the amplitude is larger (especially in the axial strain) due to the induction heating system. This becomes important when attempting to measure strains precise to a few microstrain.

Initial yield loci for specimens IN-6 and IN-25 determined at 371 and 454°C are shown in Figure 4.8 and Figure 4.9, respectively. As the temperature increases, the yield loci decrease in size, but retain the same shape. In addition, the center of the locus is not located at the origin of the stress plane. A von Mises circle with a radius of 207 MPa centered at (-13.8, 0.0) MPa in the modified axial-shear stress plane appears to fit the data at 371°C very well (Fig. 4.8). At 454°C (Fig. 4.9), a von Mises circle with a radius of 193 MPa and centered at (-27.5, 0.0) was used. These results indicate that as the temperature increases, the yield locus decreases in size and its center translates in the compression direction. A possible explanation for the translation of the center of the yield locus is discussed in the next section.

Next, specimen IN-6 was subjected to combined axial-torsional prestraining, as shown in Figure 4.10. Point A corresponds to the location where the initial loci were determined. Subsequent yield loci were determined at locations C, O, Q, and S.

The first prestrain consisted of combined tension-torque loading at 454°C. Specimen IN-6 was strained along a $\angle 45^\circ$ radial path in equivalent

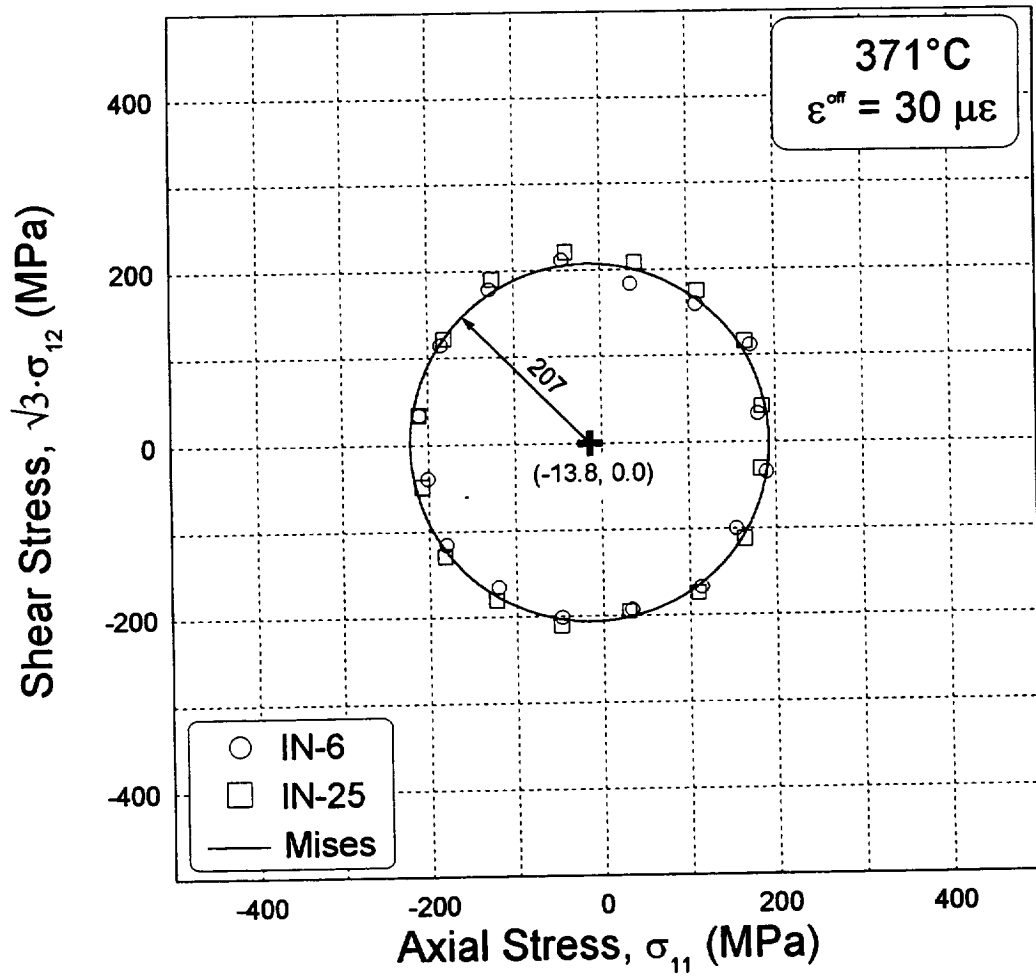


Figure 4.8 - Initial yield loci for solutioned IN718 at 371°C.

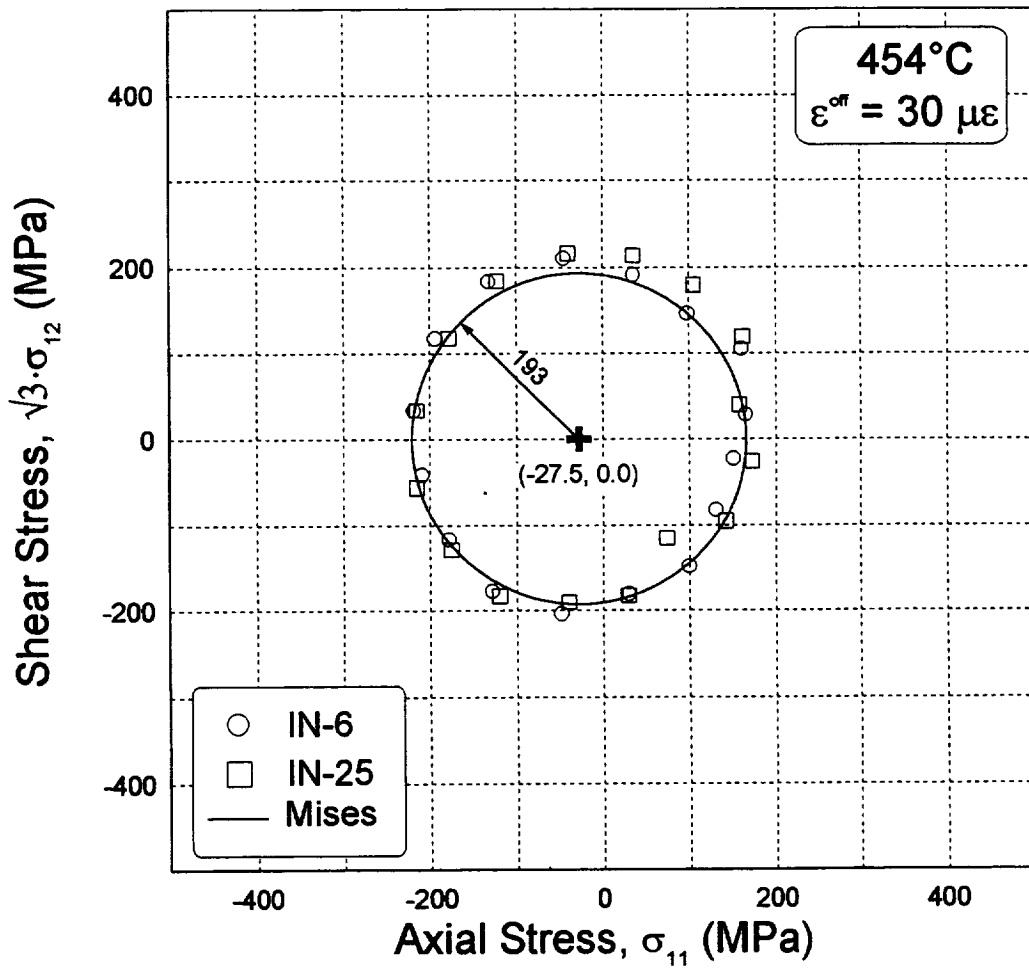


Figure 4.9 - Initial yield loci for solutioned IN718 at 454°C.

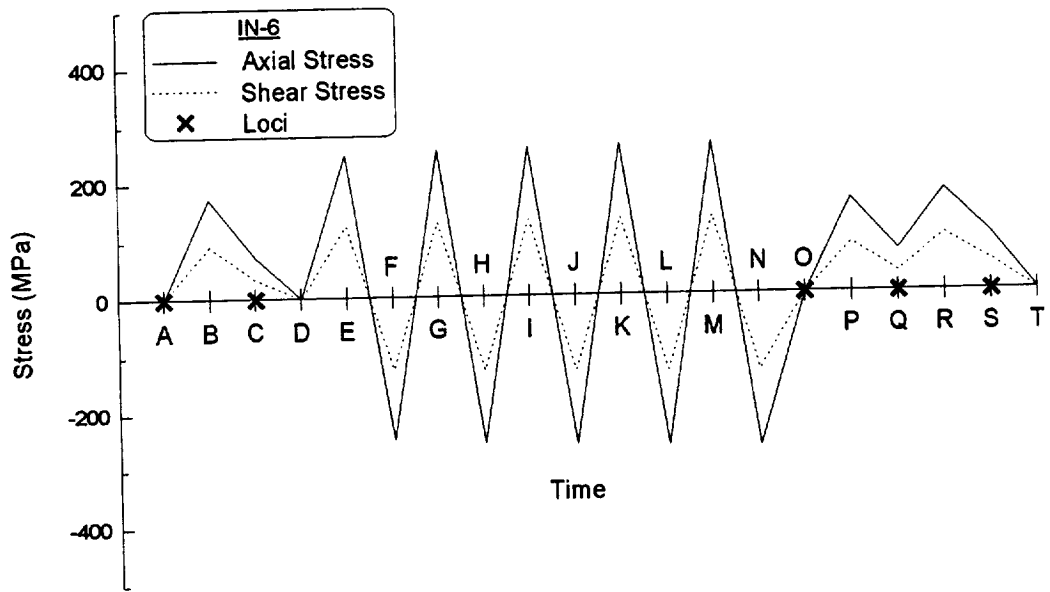


Figure 4.10 - Loading history for specimen IN-6 indicating where yield loci were determined.

strain space (path $OA_1A_2A_3$ in Figure 3.8) until an equivalent offset strain of $500 \mu\epsilon$ was attained (point B in Figure 4.10). The center of the elastic region (point C) was then found, as described in the previous section, and two subsequent loci were determined.

The first subsequent yield locus (Locus C) is shown in Figure 4.11, along with the prestrain point B. A spline fit is included to aid in interpreting the data. There is clearly some translation of the yield locus toward the prestrain point. Furthermore, the back of the locus has become flattened indicating some distortional hardening. Various researchers have observed similar results for monolithic metals such as aluminum (Phillips et al., 1972), brass (Helling et al., 1986), and stainless steel (Wu and Yeh, 1991). Figure 4.11 also indicates that neither the isotropic nor kinematic hardening laws accurately describe the hardening behavior of solutioned IN718 at 454°C . Furthermore, the locus shows a small amount of cross effect, that is, an expansion of the locus in the directions perpendicular to the prestrain direction.

Solutioned IN718 exhibited very little hardening behavior during the first prestrain cycle at 454°C , as shown by the axial and shear stress-strain curves in Figure 4.12. Upon reaching prestrain point B, the axial and shear responses were nearly perfectly plastic. In an attempt to work harden the material, specimen IN-6 was subjected to five strain-controlled cycles of combined axial-torsional loading at 23°C , beginning and ending at zero stress (Fig. 4.13). The

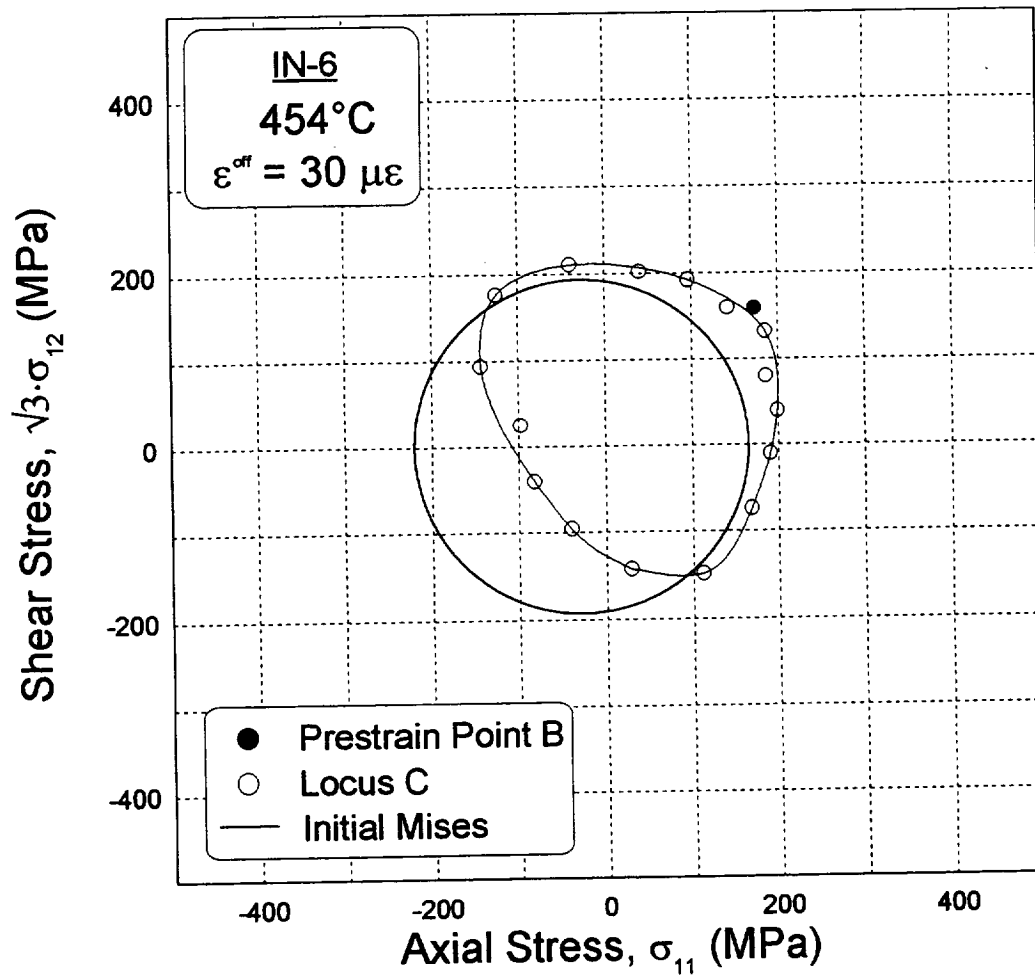


Figure 4.11 - Yield locus subsequent to a tension-torsion prestrain of 500 $\mu\epsilon$ offset for solutioned IN718 at 454°C.

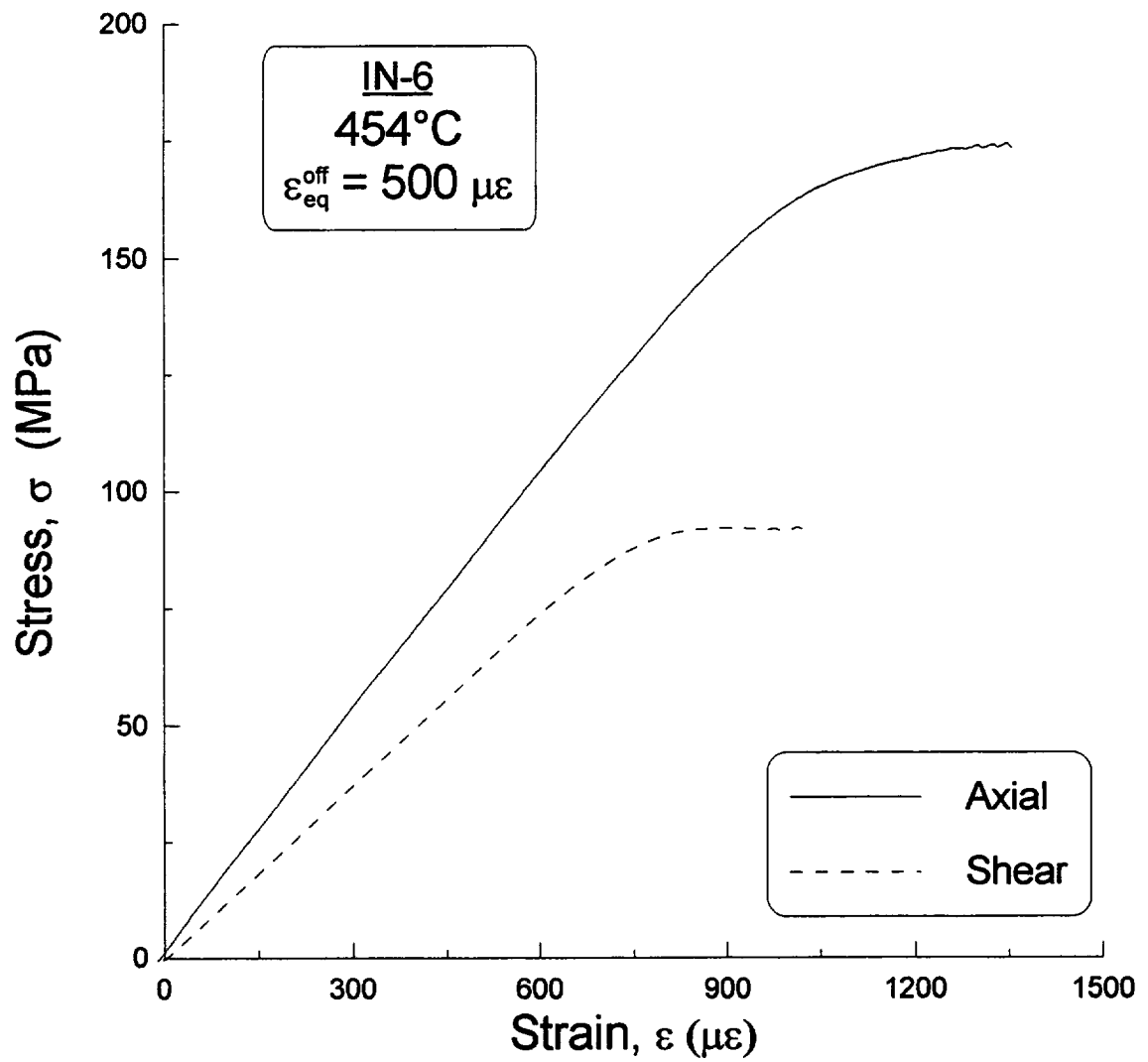


Figure 4.12 - Axial and shear stress-strain curves for a proportional prestrain of a 500 $\mu\epsilon$ equivalent offset for solutioned IN718 at 454°C.

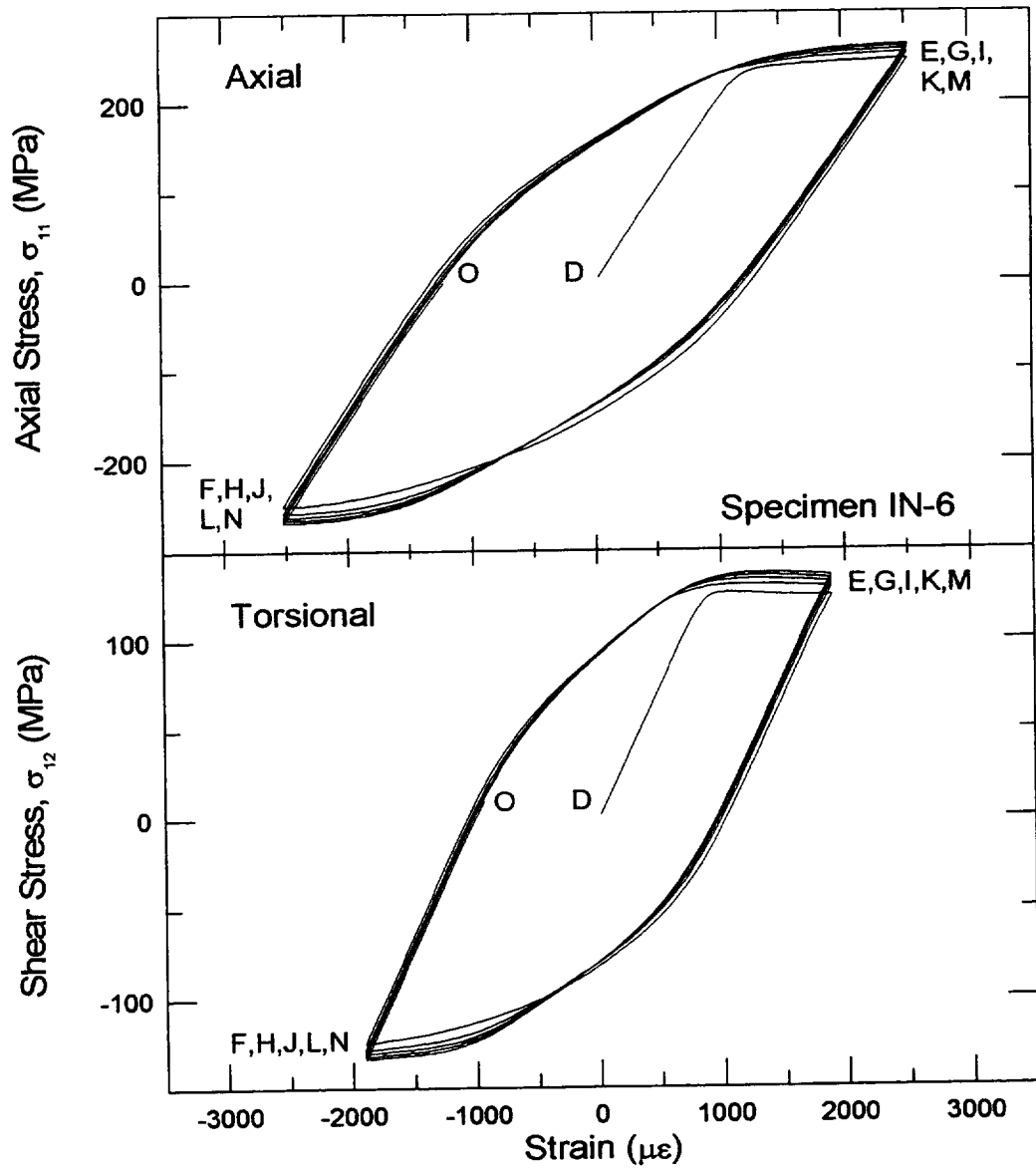


Figure 4.13 - Combined axial-torsional cyclic loading at room temperature ($\theta = 45/225^\circ$). Five complete cycles beginning and ending at zero stress.

radial strain path, with limits of $\epsilon_{11} = \pm 2500 \mu\epsilon$ and $\epsilon_{12} = \pm 1875 \mu\epsilon$, corresponded to $\angle 45^\circ$ for positive strains and $\angle 225^\circ$ for negative strains, as measured counterclockwise from the positive axial strain axis.

The last cycle ended when the axial and torsional loads reached zero, thus the final loading was in the $\angle 225^\circ$ direction. Terminating the final cycle at zero stress (point O in Fig. 4.13) led to an equivalent offset strain of $1625 \mu\epsilon$ between points O and D. Specimen IN-6 was then reheated to 454°C and a subsequent yield locus was determined. Figure 4.14 shows the subsequent locus (Locus O) as well as the prestrain path. As expected, the locus has been translated and distorted in the $\angle 225^\circ$ direction compared to Figure 4.11 and was located at approximately the same position as the initial Mises circle. It also appears that the cyclic loading may have slightly increased the yield strength in the directions perpendicular to the loading path.

Specimen IN-6 was again prestrained in the $\angle 45^\circ$ direction at 454°C until an equivalent offset strain of $1000 \mu\epsilon$ was achieved (point P, Fig. 4.10). Locus Q was then determined, as shown in Figure 4.15, and was again translated in the direction of prestrain and distorted. From this point, specimen IN-6 was then further prestrained until an additional offset strain of $500 \mu\epsilon$ was reached (point R, Fig. 4.10) and locus S was determined (Fig. 4.15). For each locus shown in Figure 4.15, the corresponding prestrain point is shown to provide a reference. Loci Q and S are very similar in shape and size, however

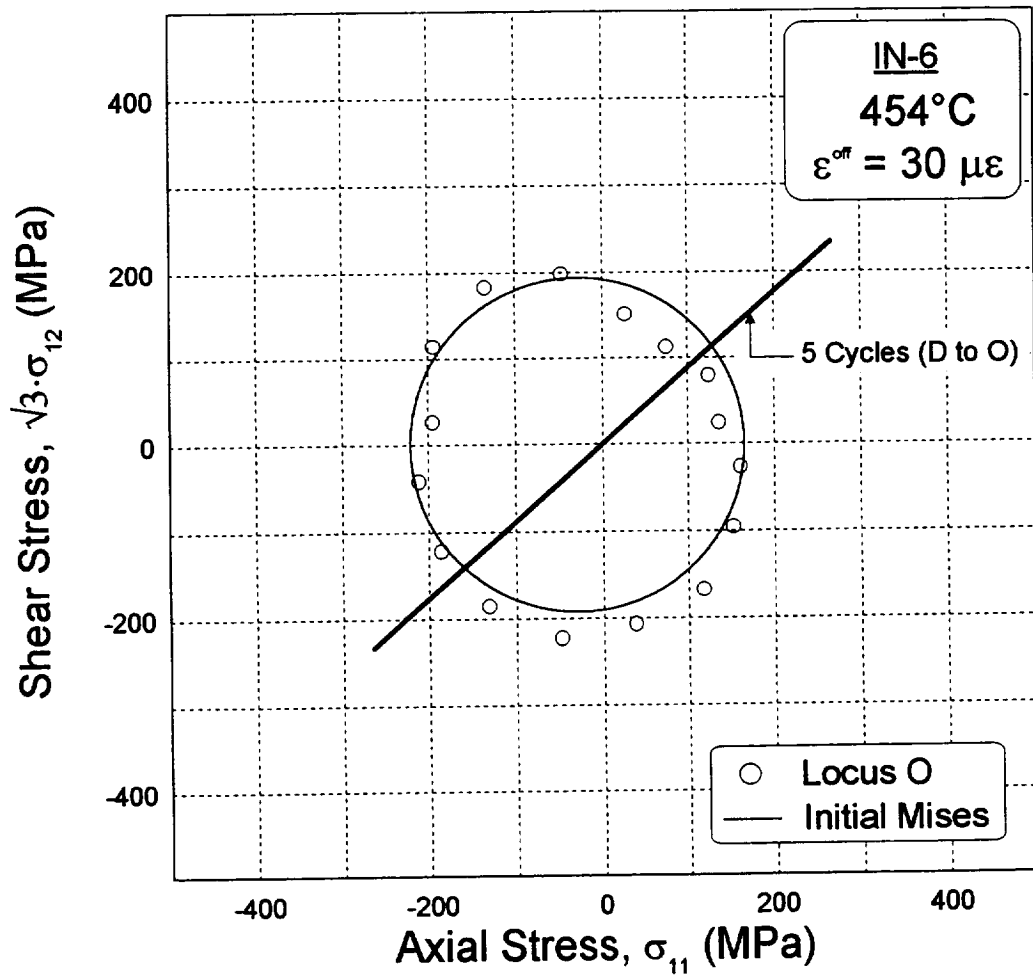


Figure 4.14 - Yield locus subsequent to cyclic loading for solutioned IN718 at 454°C.

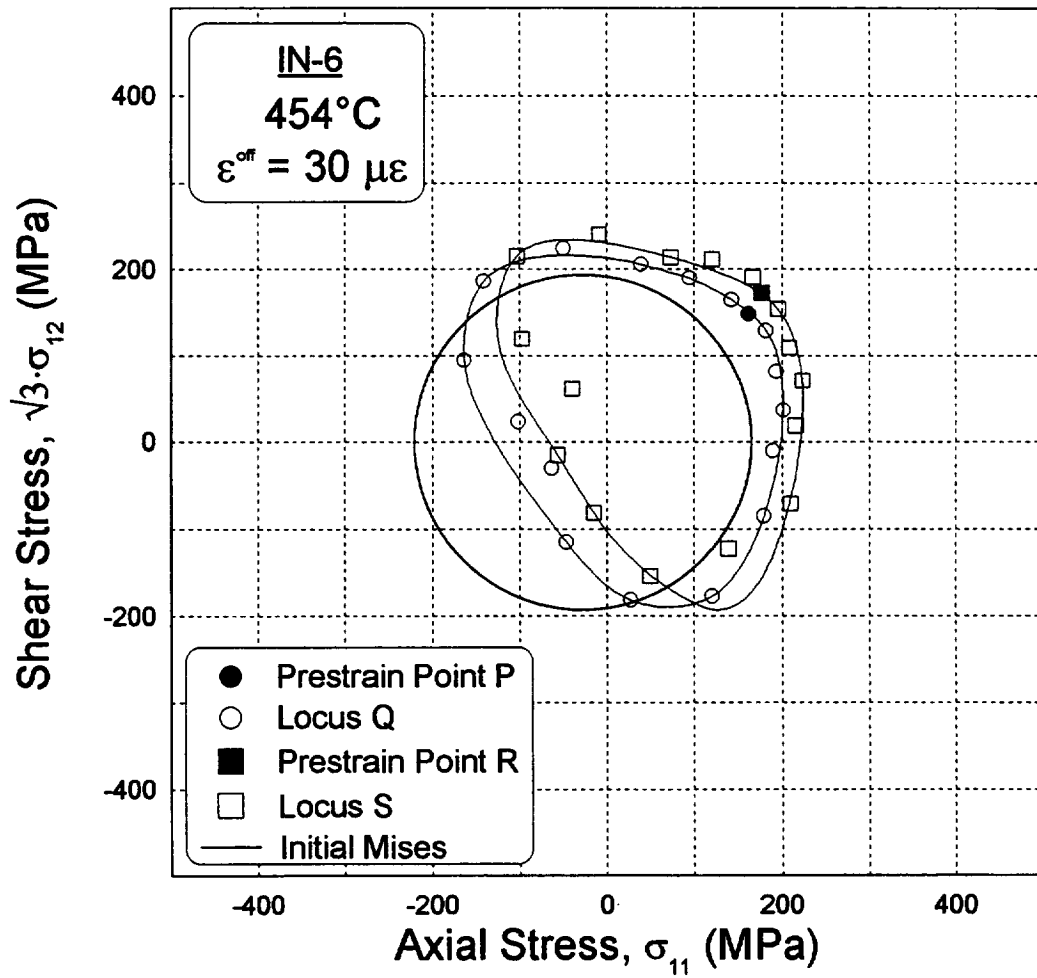


Figure 4.15 - Subsequent yield loci for proportional prestraining to 1000 $\mu\epsilon$ offset (locus Q) and 1500 $\mu\epsilon$ offset (locus S) for solutioned IN718 at 454°C.

locus S is shifted slightly more in the prestrain direction with respect to locus Q due to the additional prestrain. Additionally, the loci have expanded slightly in the direction perpendicular to the prestrain direction. This expansion could be due to a combination of the cyclic loading (cyclic hardening) and cross effect.

4.2 Aged Inconel 718

Experiments to determine yield loci for aged IN718 were hindered by an anomalous material response, termed *stiffening* (Gil et al., 1998), that occurred during compressive loading. Stiffening is a nonlinear material response that is characterized by a slight increase in the instantaneous stiffness that causes nonlinear stress-strain behavior. This behavior is shown in Figure 4.16, where the offset

strain initially has a positive sign for compressive loading. At some point, as indicated in Figure 4.16, the direction of the offset strain reverses. Again during unloading, the offset strain continues to increase. As mentioned, the permanent set shown in Figure 4.16 may not be representative of the true material behavior since the extensometer may be inaccurate after the load reversal.

Stiffening could be associated with nonlinear interactions between dislocations and precipitate particles. Recall from Chapter 2 that Hirth and

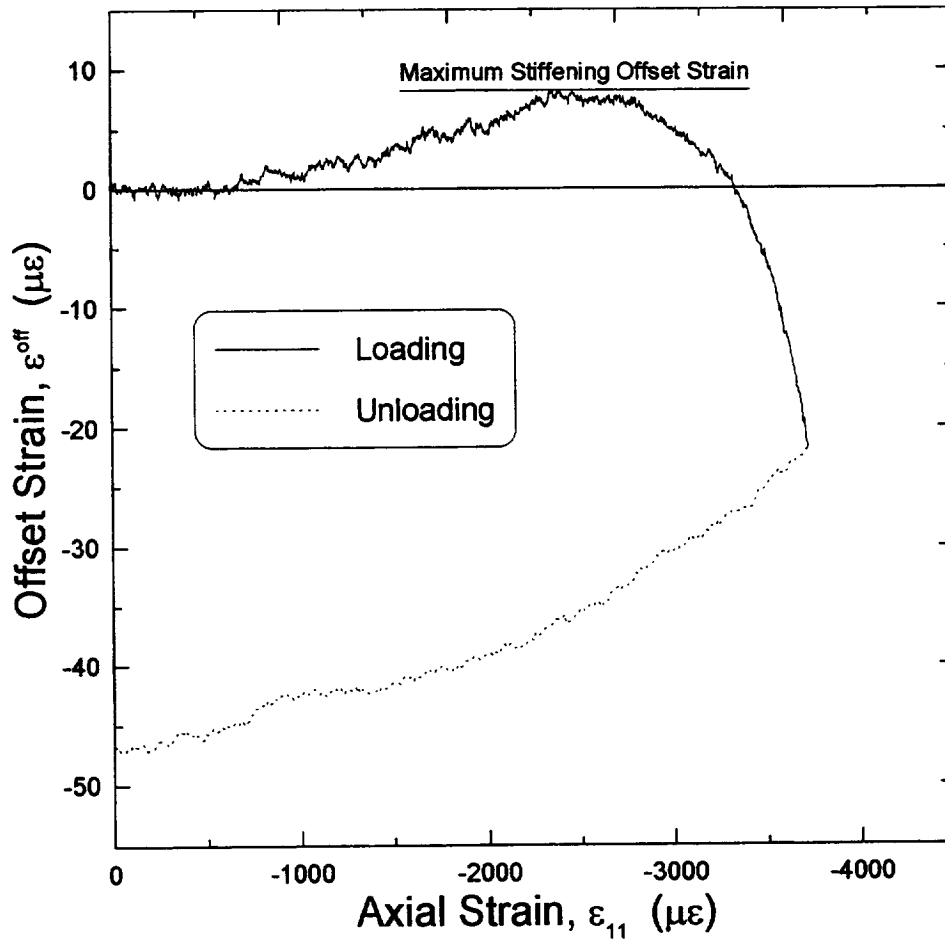


Figure 4.16 - Offset strain versus strain during compressive loading for aged IN718, indicating stiffening.

Cohen (1970) proposed a theory to account for the strength-differential effect in steels, in which dislocations interact with solute atoms causing local distortion of the lattice and leading to local elastic strains that are nonlinear. According to the model, nonlinear elastic tensile strains reduce stiffness while nonlinear elastic compressive strains increase stiffness. As a result, there is a seemingly higher yield strength in compression than in tension. Also, Kalish and Cohen (1969) suggest that this theory can also apply to the coherency strains around precipitated particles.

It is not clear whether nonlinear elastic tensile strain occurred for aged IN718 since there were no intermediate unloadings and also the permanent set after unloading may not have been accurately measured. However, nonlinear elastic strain (stiffening) was observed during compressive loading, as predicted by Hirth and Cohen. Furthermore, a strength-differential was also observed and will be discussed in more detail later.

Stiffening presented a real challenge to the procedure for detecting yielding because the procedure explicitly assumes an initial linear elastic response. If stiffening is truly an elastic response (which appeared to be the case), then inelastic strain begins to occur when the stiffening offset has reached a maximum (Fig. 4.16). Therefore, in the presence of stiffening, the inelastic strain was taken to be the offset strain plus the maximum stiffening strain.

Two virgin aged IN718 specimens (IN-8 and IN-10) were tested at 23°C and the initial yield loci are shown in Fig. 4.17. A von Mises circle of radius 655 MPa appears to fit the data well, however the locus is severely translated away from the stress origin and centered at (-138, 0) MPa. The offset of the locus in the compression direction is representative of the strength-differential effect.

As discussed in Chapter 2, the strength-differential effect may be due to several different mechanisms. Since stiffening was observed, this supports a strength-differential effect due to nonlinear elastic behavior, as modeled by Hirth and Cohen (1970). According to this theory, an equal amount of nonlinear elastic strain occurs in tension and compression. In tension, the decreasing stiffness could be mistaken for inelastic strain. In compression, the nonlinear elastic response results in stiffening. Thus, if the elastic strain in tension is mistaken for inelastic strain then there will be an apparent strength-differential. This type of strength-differential is expected to decrease with increasing plastic strain, and eventually disappear.

Several authors (e.g., Rauch and Leslie, 1972; Drucker, 1973; Rauch et al., 1975; Spitzig et al., 1975) have suggested that a strength-differential effect is associated with the influence of hydrostatic stress on yielding. As discussed in Chapter 2, many researchers have observed an increase in the yield strength in both tension and compression as a result of increasing hydrostatic

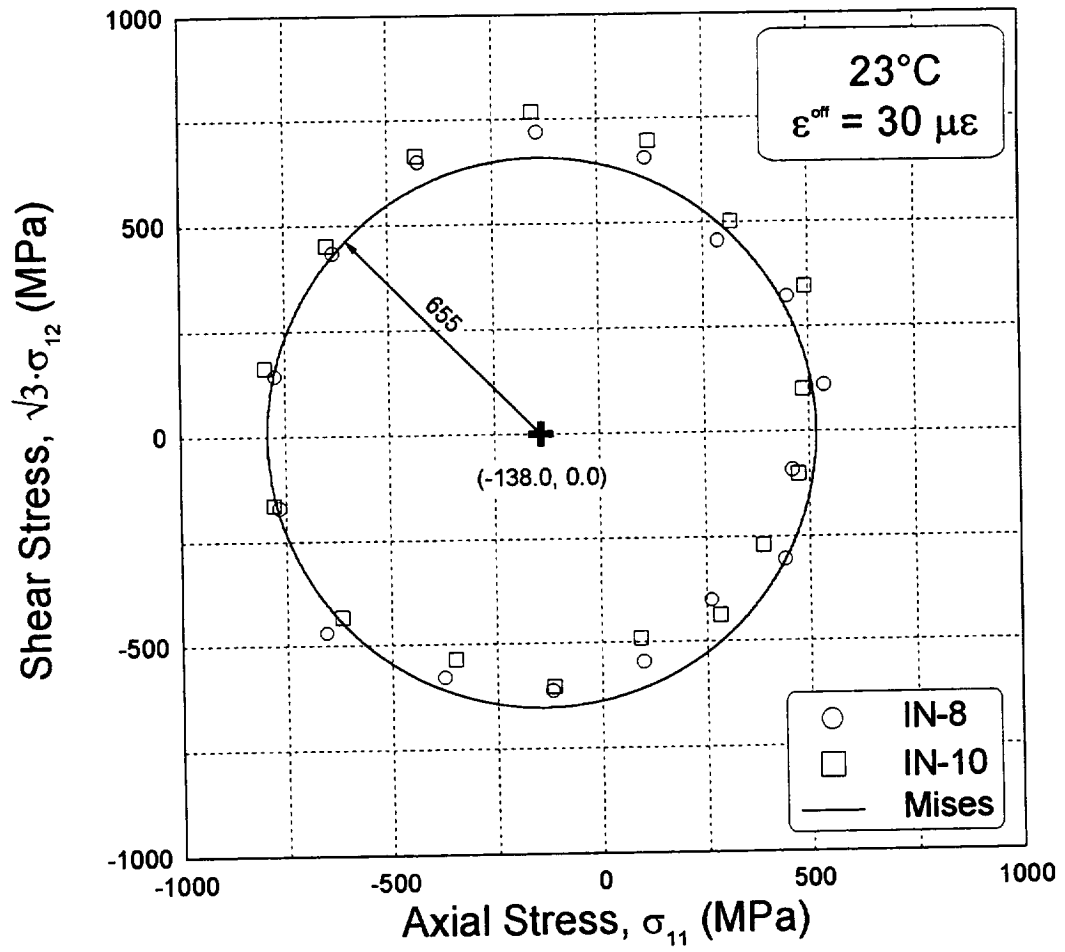


Figure 4.17 - Initial yield loci for aged IN718 at room temperature. A modified version of the von Mises yield criterion is used to fit the data.

stress. Furthermore, a yield criterion (such as the one suggested by Spitzig et al., 1975) that includes an effect of hydrostatic stress predicts a strength-differential effect.

A series of experiments in tension and compression to a larger offset strain (such as 1%) would give valuable information regarding the strength-differential effect in aged IN718. A decrease in the strength-differential would support the theory of nonlinear elastic strain, whereas a constant strength-differential with increasing plastic strain would support the theory of hydrostatic stress dependence. These tests were not performed as part of this study, however the tests are planned as part of the future work on IN718.

It quickly became apparent that there is more scatter in the aged IN718 results than in the solutioned IN718 results. This is believed to be due to the different inelastic strain behavior of the two materials. Figure 4.18 compares the von Mises effective stress ($\sqrt{3J_2}$) versus equivalent offset strain up to a 30 $\mu\epsilon$ offset for both materials under combined tension/torsion ($\theta = 57^\circ$) at 23°C. The smaller hardening modulus of the solutioned IN718 results in minimal scatter because of the small stress increment relative to the aged IN718.

The results obtained at 23°C (Fig. 4.17) on both specimens were repeatable. Specimens IN-8 and IN-10 were then tested at 649°C (Fig. 4.19). Following the same trend that was observed for solutioned IN718, the loci are

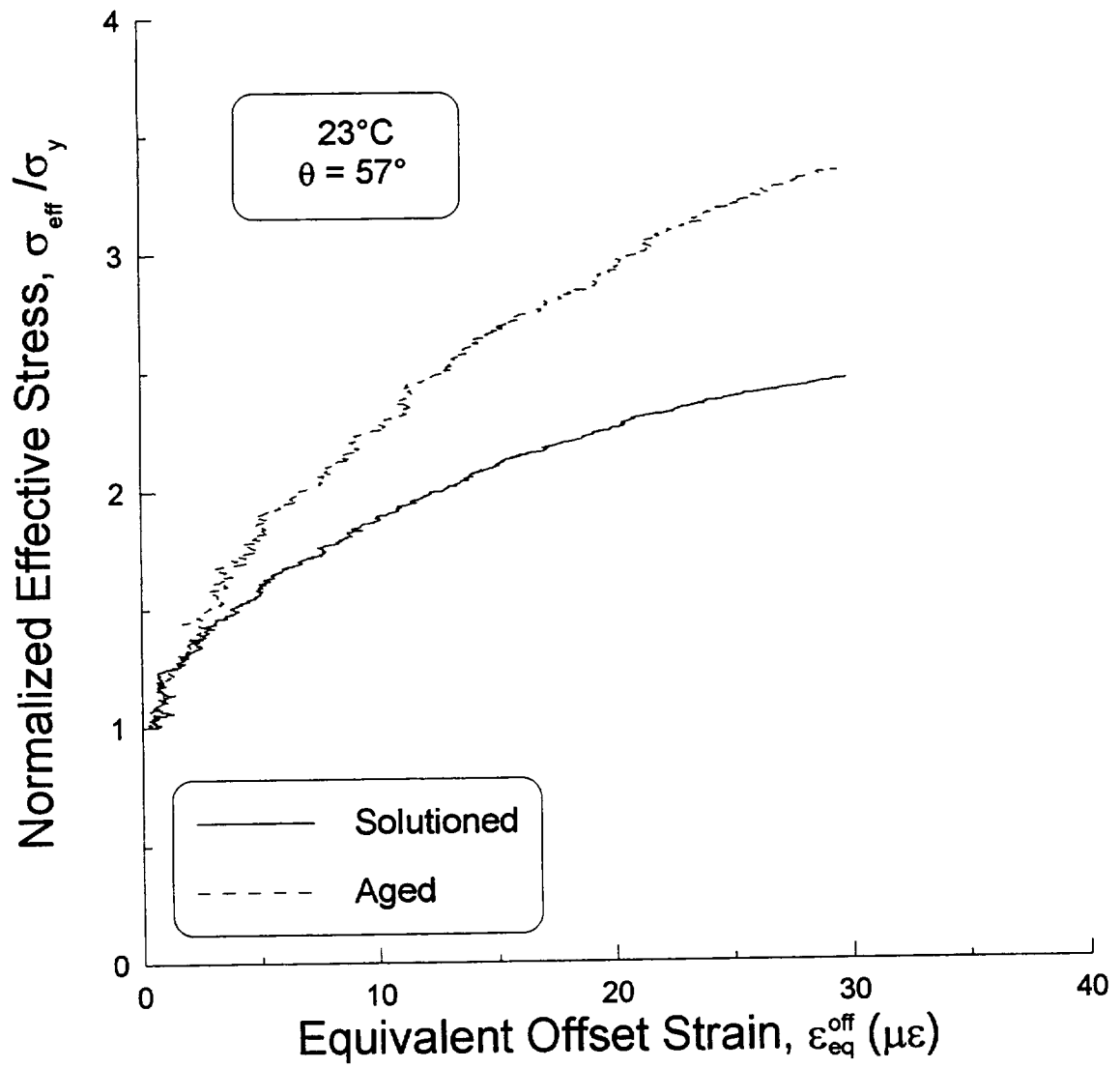


Figure 4.18 - Stress versus offset strain for solutioned and aged IN718 under tension and torsion.

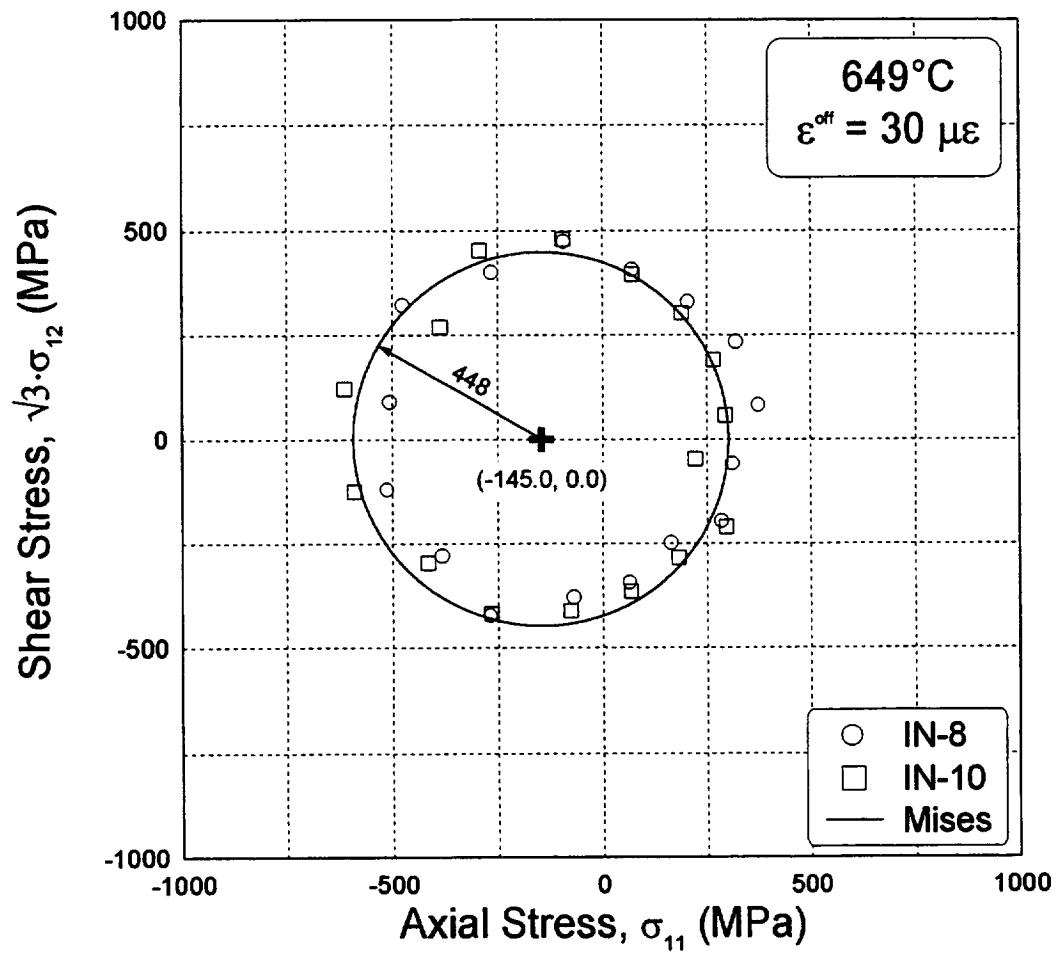


Figure 4.19 - Initial yield loci for aged IN718 at 649°C.

similar in shape to the loci at 23°C, yet smaller in size and translated further in the compression direction. A von Mises circle with a radius of 448 MPa and centered at (-145.0, 0.0) MPa appears to closely fit the data from both specimens. More scatter is observed at 649°C due to the effect of electronic noise generated by the induction heating system. The yield loci for both solutioned and aged IN718 appear to translate in the compression direction with increasing test temperature, as indicated in Table 4.1. This might be due to an increasing dependence on hydrostatic stress with temperature, however that would contradict the results of Rauch et al. (1975). More experiments are planned as part of the future work on IN718 to verify this result.

Specimen IN-10 was subjected to a combined axial-shear prestrain ($\angle 45^\circ$ in equivalent strain space) at 649°C until an equivalent offset of 500 $\mu\epsilon$ was detected. The subsequent yield locus is shown in Figure 4.20, where the initial Mises circle is also shown for reference. During the prestrain procedure the center of the locus was not accurately identified, possibly due to the influence of electronic noise, which may have led to the scatter in the data points on the yield locus. Nevertheless, a few important characteristics are observed. First, the locus is translated further in the direction of the prestrain than was observed for solutioned IN718 (Fig. 4.11). This suggests that precipitation in IN718 not only increases the yield strength of the material but also increases its ability to strain harden. Additionally, there appears to be no

Temperature (°C)	<u>Solutioned</u>		<u>Aged</u>	
	Radius of Mises Circle (MPa)	Center of Mises Circle (MPa)	Radius of Mises Circle (MPa)	Center of Mises Circle (MPa)
23	248	(0.0, 0.0)	655	(-138.0, 0.0)
371	207	(-13.8, 0.0)	-	-
454	193	(-27.5, 0.0)	-	-
649	-	-	448	(-145.0, 0.0)

Table 4.1 - Radius and center of each initial yield locus for solutioned and aged IN718 as a function of temperature.

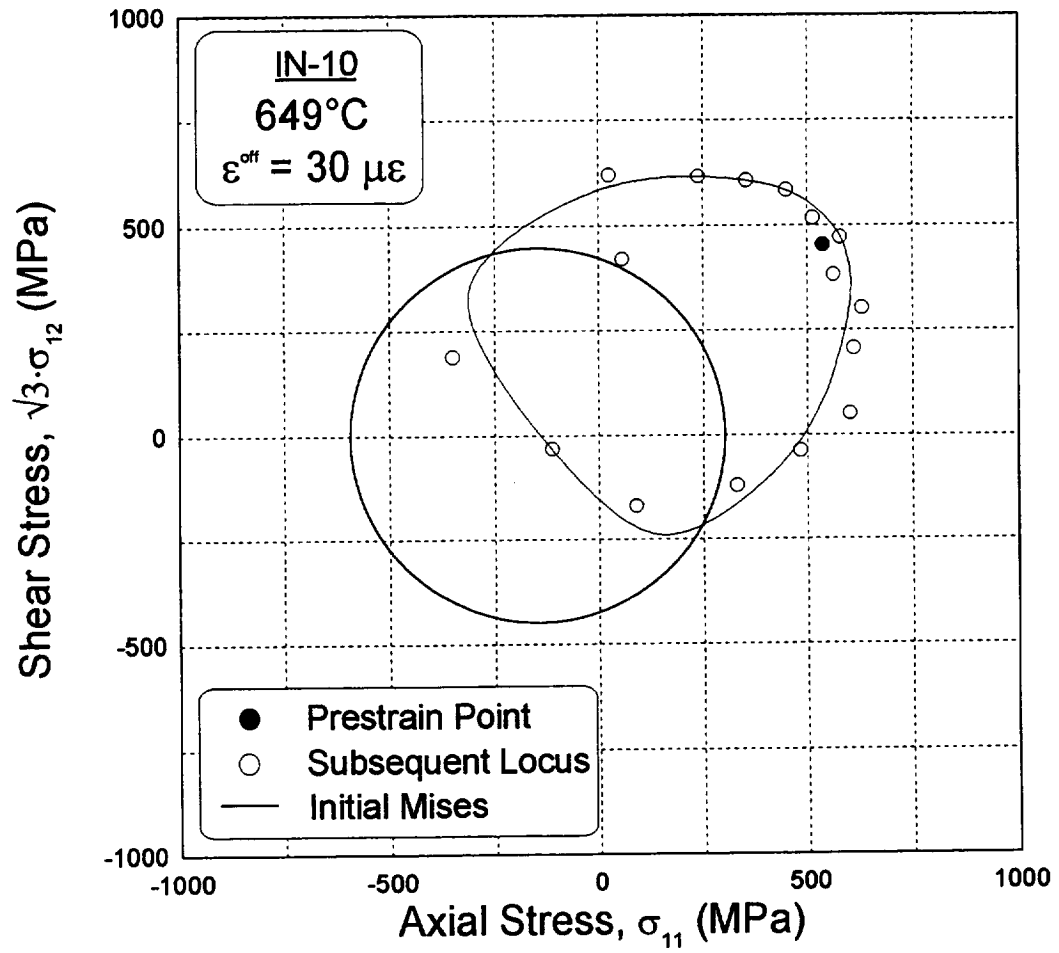


Figure 4.20 - Yield locus subsequent to a tension-torsion prestrain of $500 \mu\epsilon$ offset for aged IN718 at 649°C.

cross effect, however it is difficult to make any strong conclusions based on the limited amount of data that was collected.

The other aged specimen (specimen IN-8) was subjected to a tensile prestrain until a total axial strain of $9000 \mu\epsilon$ (0.9%) had been reached. The first subsequent yield locus is shown in Figure 4.21. The locus translated in the direction of prestrain and distorted. No cross effect is observed. However, despite being distorted the locus appears to have elongated in the direction of the prestrain.

4.3 Re-Solutioned Inconel 718

Solution treating a metal can return the material to a virgin or near-virgin material state. In order to investigate this, two permanently deformed specimens were re-solutioned and then tested at 23°C. The first specimen (specimen IN-6), originally solutioned, had been subjected to a complex loading history (Fig. 4.10). The second specimen (specimen IN-10), originally solutioned and aged, had been tested extensively at 649°C (Fig. 4.19-4.20).

Specimens IN-6 and IN-10 were solutioned, as described in Chapter 3. The initial yield locus for each specimen was then determined at 23°C using the same procedure as in earlier tests. Figure 4.22 shows the result of these tests as well as the first initial yield locus for specimen IN-6 at 23°C. All three data sets are essentially the same. This indicates that solutioned and

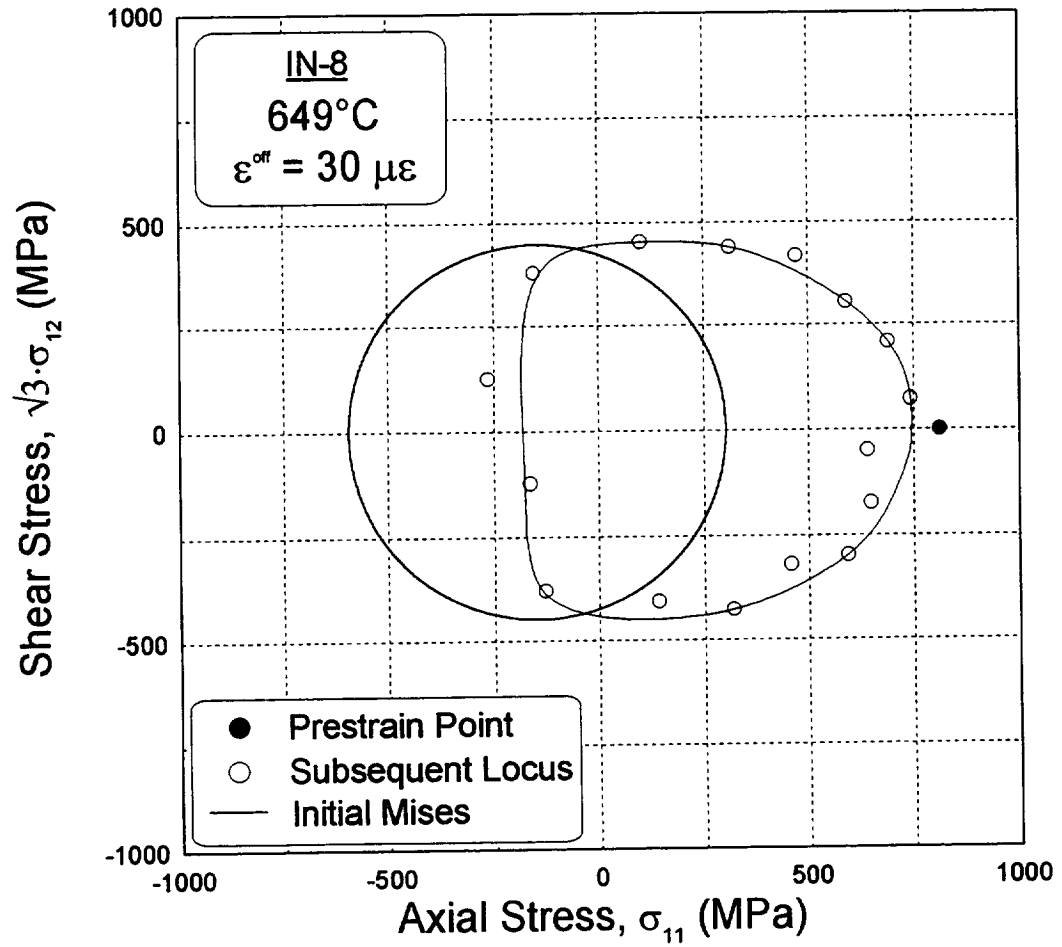


Figure 4.21 - Yield locus subsequent to a tension prestrain of $9000 \mu\epsilon$ (0.9%) for aged IN718 at 649°C.

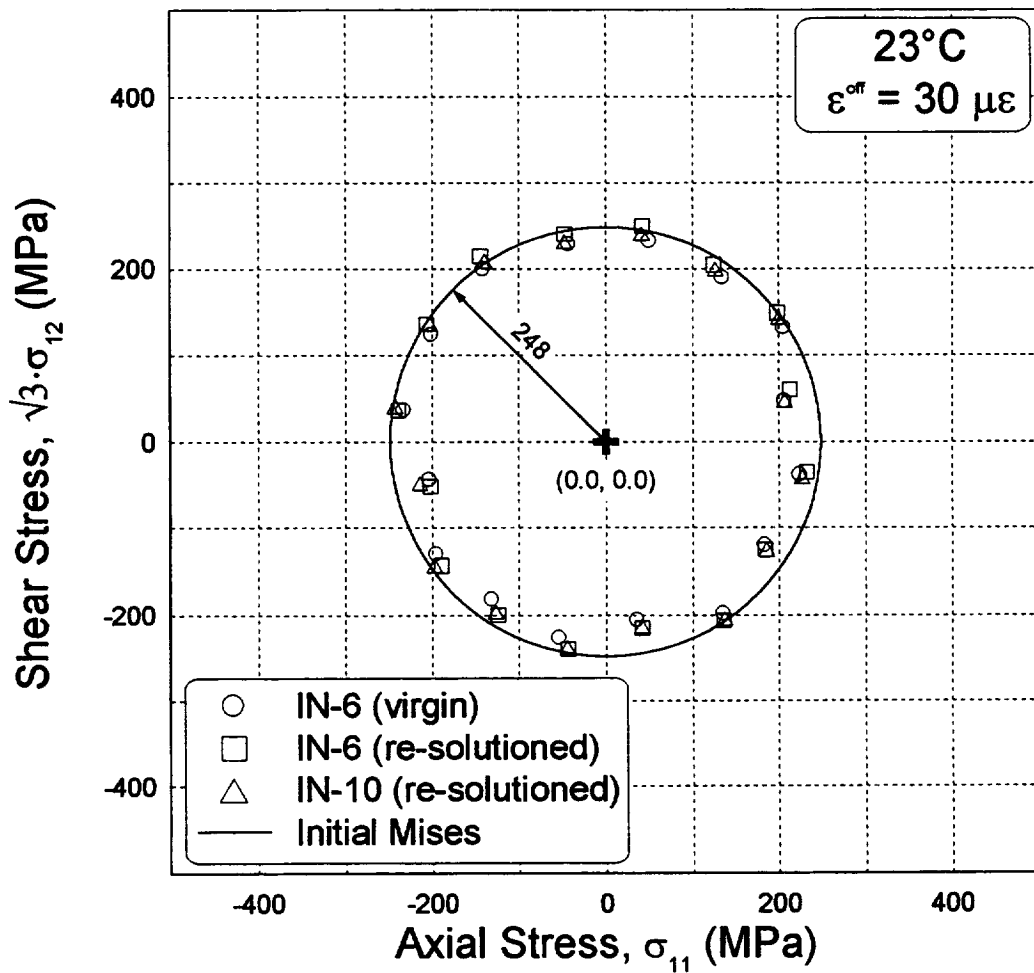


Figure 4.22 - Comparison of yield loci for a solutioned specimen in the virgin state and after significant deformation followed by re-solutioning. The yield locus for previously aged specimen that has been re-solutioned is also shown.

solutioned + aged specimens that have been lightly deformed ($< \sim 1\%$) can be returned to their original material state by re-solutioning them. Furthermore, it is suspected that the aged specimen (specimen IN-10) would produce similar results to Figure 4.17 (initial locus for aged IN718 at 23°C) if it were re-aged.

CHAPTER 5

REVIEW OF VISCOPLASTICITY IN METALS

At elevated temperatures, metals typically exhibit time-dependent deformation. Many time-independent plasticity models handle time-dependent deformation by considering creep strains to be additive to time-independent plastic strain. Many viscoplasticity models have taken a unified approach, where there is no decomposition and all permanent deformation is lumped together and given the term *inelastic strain*. This chapter reviews some recent advances in viscoplasticity theory. First, in section 5.1 the physical mechanisms of time-dependent deformation are discussed. Section 5.2 presents a thermodynamic framework for viscoplasticity. In section 5.3, two unified viscoplasticity models are summarized. Finally, section 5.4 discusses the correlation between experiments and theory.

5.1 Physical Mechanisms

The physical mechanisms of rate-independent deformation were discussed in Chapter 2. In this section, some of the physical mechanisms associated with time-dependent deformation are covered. Again, no attempt is

made to cover all aspects of time-dependent deformation. A more comprehensive discussion is given by Stouffer and Dame (1996).

Recall from Chapter 2 that slip is the dominant deformation mechanism at low temperatures. At high temperatures metals also deform by dislocation climb and dislocation glide. Dislocation climb is the diffusion of atoms or vacancies to or away from an edge dislocation. When this occurs, the edge dislocation moves perpendicular to the slip plane. Positive climb occurs when the slip plane is in compression and is associated with the removal of atoms from the dislocation plane. This results in the dislocation moving up one atomic distance. Negative climb is due to tensile forces on the slip plane and occurs when atoms are added to the dislocation plane. During dislocation glide, dislocations move along slip planes and overcome barriers with the assistance of thermal energy and stress.

At elevated temperatures, inelastic deformation can occur while the stress state is held constant (and nonzero) due to creep. Creep is time-dependent and results mainly from diffusion, dislocation glide, and dislocation climb. During dislocation glide, the creep rate is controlled by the intrinsic activation energy of the particular dislocation-barrier system and by thermal and external energy. The creep rate resulting from dislocation climb depends on the diffusion properties of the material and the thermal and mechanical loads. The primary driving forces for creep are temperature and stress.

Another important mechanism at elevated temperatures is recovery. Static recovery is a diffusion controlled process and occurs after inelastic deformation has taken place and the loads have been removed. During static recovery, dislocations are mobilized by the interaction stresses that occur between dislocations. Recovery occurs as a result of dislocation annihilation or polygonization.

At elevated temperature, dynamic recovery occurs simultaneously with inelastic deformation and results from the formation of subgrains. Dynamic recovery can also occur at low temperature resulting in dislocation cells, however the effect of recovery is greater at higher temperatures since the mobility of dislocations and vacancies increases with temperature. A decrease in the dislocation density and effective rate of strain hardening may result from dynamic recovery.

5.2 Thermodynamic Framework of Unified Viscoplasticity

The material response of metals can be represented in terms of thermodynamics, where elastic and inelastic deformation is characterized by reversible and irreversible processes, respectively. Several phenomenological viscoplasticity theories have been formulated using thermodynamic principles (two are summarized in section 5.3). This section gives an overview of the thermodynamic approach to viscoplastic constitutive modeling.

5.2.1 General Principles

All thermodynamic processes must obey certain basic principles. These include:

- *Conservation of Mass*

$$\rho dV = \text{constant} \quad (5.1)$$

where ρ is the mass density and dV is a differential volume element.

- *Conservation of Linear Momentum, which results in*

$$\sigma_{ij,j} + \rho b_i = \rho a_i \quad (5.2)$$

where b_i is the body force, a_i is the acceleration, and $_{,j}$ represents the first derivative with respect to x_j .

- *Conservation of Angular Momentum, which provides*

$$\sigma_{ij} = \sigma_{ji} \quad (5.3)$$

- *Conservation of Energy (1st Law of Thermodynamics)*

$$\rho \dot{u} = \sigma_{ij} \dot{\epsilon}_{ij} + \rho r - q_{i,i} \quad (5.4)$$

where \dot{u} is the internal energy density, r is the heat supply, and $q_{i,i}$ is the heat flux. Here, only mechanical and thermal energy are considered.

- *Clausius-Duhem Inequality (2nd Law of Thermodynamics)*

$$\rho \dot{s} - \rho \frac{r}{T} + \left(\frac{q_i}{T} \right)_{,i} \geq 0 \quad (5.4)$$

where \dot{s} is the specific entropy and T is the absolute temperature.

These basic principles are necessary for derivation of material behavior on a thermodynamic basis.

5.2.2 The State Law

Using a stress formulation, the state of a material can be characterized by the current stress state (σ_{ij}), the absolute temperature (T), and an array of internal variables (ξ_α), which can be scalars or tensors. The Gibb's free energy $G(\sigma_{ij}, T, \xi_\alpha)$ is chosen as the thermodynamic potential

$$G = \sigma_{ij} \varepsilon_{ij} - H \quad (5.5)$$

where $H(\varepsilon_{ij}, T, \varepsilon_{ij}^m, \xi_\alpha)$ is the Helmholtz free energy, given by

$$H = u - Ts \quad (5.6)$$

where u and s are the specific internal energy and entropy, respectively.

The first derivative of the Gibb's free energy can be expressed as

$$dG = \frac{\partial G}{\partial \sigma_{ij}} d\sigma_{ij} + \frac{\partial G}{\partial T} dT + \frac{\partial G}{\partial \xi_\alpha} d\xi_\alpha \quad (5.7)$$

such that

$$\varepsilon_{ij} \equiv -\frac{\partial G}{\partial \sigma_{ij}}, \quad s \equiv -\frac{\partial G}{\partial T}, \quad p_\alpha \equiv -\frac{\partial G}{\partial \xi_\alpha} \quad (5.8)$$

where p_α are the generalized forces.

The total strain rate can then be written as

$$\dot{\varepsilon}_{ij} = \frac{d}{dt} \left(-\frac{\partial G}{\partial \sigma_{ij}} \right) = -\frac{\partial^2 G}{\partial \sigma_{ij} \partial \sigma_{kl}} \dot{\sigma}_{kl} - \frac{\partial^2 G}{\partial \sigma_{ij} \partial T} \dot{T} - \frac{\partial^2 G}{\partial \sigma_{ij} \partial \xi_\alpha} \dot{\xi}_\alpha \quad (5.9)$$

where for linear elasticity and isothermal conditions, Equation (5.9) reduces to

$$\dot{\varepsilon}_{ij} = -\frac{\partial^2 G}{\partial \sigma_{ij} \partial \sigma_{kl}} \dot{\sigma}_{kl} \quad (5.10)$$

5.2.3 The Dissipation Potential

In rate-independent plasticity theory (Chapter 2) the flow rule was written in terms of a plastic potential function. A similar potential function is assumed in viscoplasticity theory, called the dissipation potential, $\Omega(\sigma_{ij}, T, \xi_\alpha)$, which serves a similar role to the yield surface in rate-independent plasticity. Thus, the flow law can be written as

$$\dot{\varepsilon}_{ij}^{in} = \frac{\partial \Omega}{\partial \sigma_{ij}} \quad (5.11)$$

As with the yield surface, the dissipation potential evolves as a result of inelastic deformation. The evolution equation may be expressed as

$$\dot{p}_\alpha = -\frac{\partial \Omega}{\partial \xi_\alpha} \quad (5.12)$$

where \dot{p}_α is the first time derivative of p_α . Considering isothermal conditions,

Equation (5.12) can be rewritten in terms of the Gibb's free energy as

$$\dot{p}_\alpha = -\frac{\partial^2 G}{\partial \xi_\alpha \partial \xi_\beta} \dot{\xi}_\beta = Q_{\alpha\beta} \dot{\xi}_\beta \quad (5.13)$$

where $Q_{\alpha\beta}$ is an array of internal compliance tensors.

5.3 Unified Viscoplasticity Models

In classical plasticity theory, time-dependent behavior, such as creep, is considered additive to the rate-independent plastic strain. In unified viscoplasticity theory, there is no decomposition of the inelastic strain into rate-independent and rate-dependent components. Therefore, unified viscoplasticity models can account for interaction between plasticity and creep. Furthermore, some unified models make use of a yield criterion, whereas others do not. In the following subsections two unified viscoplasticity models are summarized. The Bodner-Partom model is derived from a framework of dislocation dynamics, whereas a Generalized Viscoplasticity with Potential Structure (GVIPS) model is derived from the general thermodynamic framework that was discussed in section 5.2.

5.3.1 Bodner-Partom

The Bodner-Partom constitutive equations (Bodner and Partom, 1975) are based on dislocation dynamics and no formal yield criterion is used. Thus, elastic and inelastic deformation are assumed to take place during the entire loading regime. However, there may exist a region in stress space where the inelastic strain component is insignificant. A brief summary of the basic

constitutive equations is provided. A more detailed description can be found in a review by Bodner (1987).

The total strain rate is decomposed into elastic and inelastic components, given by

$$\dot{\varepsilon}_{ij} = \dot{\varepsilon}_{ij}^e + \dot{\varepsilon}_{ij}^{in} \quad (5.14)$$

where $\dot{\varepsilon}_{ij}^e$ and $\dot{\varepsilon}_{ij}^{in}$ designate the elastic and inelastic components of the strain rate, respectively. The elastic strain rate component is given by the time derivative of Hooke's law. The inelastic component of the strain rate is given by

$$\dot{\varepsilon}_{ij}^{in} = \phi s_{ij} \quad (5.15)$$

which is the Prandtl-Reuss flow law. To account for isotropic hardening,

$$\phi = \frac{D_o}{\sqrt{J_2} \exp\left[\left(\frac{Z^2}{3J_2}\right)^n \left(\frac{n+1}{2n}\right)\right]} \quad (5.16)$$

where J_2 is the second invariant of deviatoric stress and D_o , Z , and n are material parameters. Kinematic hardening is represented by using an effective internal variable,

$$Z_{eff} = Z_o + q \int_0^t \dot{Z}(\tau) d\tau + (1-q) r_{ij} \int_0^t \dot{Z}(\tau) r_{ij} d\tau \quad (5.17)$$

where

$$r_{ij} = \frac{\sigma_{ij}}{\sqrt{\sigma_{kl}\sigma_{kl}}} \quad (5.18)$$

are the current stress direction cosines and the evolution equation is,

$$\dot{Z} = \frac{m(Z_1 - Z)\dot{W}_{in}}{Z_o} \quad (5.19)$$

where $\dot{W}_{in} = \sigma_{ij}\dot{\epsilon}_{ij}^{in}$ is the inelastic power. The material parameters that must be determined by experiments are Z_o , Z_1 , D_o , m , n , and q (typically uniaxial loading is used). The parameter q effectively controls the amount of kinematic hardening relative to isotropic hardening (see Equation 5.17).

5.3.2 GVIPS

The Generalized Viscoplasticity with Potential Structure (GVIPS) Model (Arnold et al., 1996) is completely derivable from the thermodynamic framework presented in section 5.2. The model uses a yield criterion, one internal variable (the back stress, α_{ij}), and an evolutionary law to account for nonlinear hardening. Evolution of the internal state variable is related to its thermodynamic conjugate by an internal compliance tensor, which is derived from the Gibb's potential.

The Gibb's free energy potential is written as

$$G = G_E + G_I + G_A = -\frac{1}{2}C_{ijkl}\sigma_{ij}\sigma_{kl} - \sigma_{ij}\epsilon_{ij}^{in} - B_0(g + B_1g^p) \quad (5.20)$$

and the dissipation potential as

$$\Omega = \frac{\mu f^{n+1}}{n+1} + \frac{R_\alpha B_0 g^{q+1}}{q+1} \quad (5.21)$$

The internal state variable is given the symbol α_{ij} and its conjugate is λ_{ij} . The resulting theory is then given by three basic equations: the flow law,

$$\dot{\epsilon}_{ij}^{in} = \dot{\lambda} \Sigma_{ij} \quad (5.22)$$

the evolution law,

$$\dot{\lambda}_{ij} = \begin{cases} Q_{ijkl} C_{klpq} b_{pq} & \text{if } \alpha_{ij} \Sigma_{ij} < 0 \\ b_{ij} & \text{if } \alpha_{ij} \Sigma_{ij} \geq 0 \end{cases} \quad (5.23)$$

and the internal constitutive rate law,

$$\dot{\alpha}_{ij} = L_{ijkl} \dot{\lambda}_{kl} \quad (5.24)$$

where

$$\dot{\lambda} = \sqrt{\frac{\dot{\epsilon}_{ij}^{in} \dot{\epsilon}_{ij}^{in}}{2J_2}} \quad (5.25)$$

$$L_{ijkl} = Q_{ijkl}^{-1} = K_1 (I_{ijkl} + K_2 \alpha_{ij} \alpha_{kl}) \quad (5.26)$$

$$b_{ij} = \dot{\epsilon}_{ij}^I - K_3 \alpha_{ij} \quad (5.27)$$

$$f = \left\langle \frac{\sqrt{3J_2}}{\kappa} - y \right\rangle, \quad y = \langle 1 - \beta \sqrt{g} \rangle, \quad g = \frac{3\alpha_{ij} \alpha_{ij}}{2\kappa_0^2} \quad (5.28)$$

$$J_2 = \frac{1}{2} \Sigma_{ij} \Sigma_{ij}, \quad \Sigma_{ij} = s_{ij} - \alpha_{ij} \quad (5.29)$$

$$s_{ij} = \sigma_{ij} - \frac{1}{3} \sigma_{kk} \delta_{ij}, \quad \alpha_{ij} = \alpha_{ij} - \frac{1}{3} \alpha_{kk} \delta_{ij} \quad (5.30)$$

In the above equations, f is the yield criterion, y is the yield stress below which there is only elastic strain, I_{ijkl} is the fourth order identity tensor, δ_{ij} is the kronecker delta function, α_{ij} is the deviatoric back stress, Σ_{ij} is the effective stress, and $\langle \rangle$ are the MacCauley brackets, such that

$$\langle x \rangle = \begin{cases} 0 & \text{if } x \leq 0 \\ x & \text{if } x > 0 \end{cases} \quad (5.31)$$

The constants $K_1 - K_3$ contain the material parameters $(B_o, B_1, R_\alpha, \kappa_o, \kappa, \mu, \beta, n, p, q)$.

5.4 Experimental Considerations

An important step in the development of multiaxial viscoplasticity models is experimental evaluation. Three types of experiments (Robinson, 1985) are necessary to support the development of a potential based model for viscoplastic material behavior. These are

- *Exploratory* experiments that aid in developing the functional form of the dissipation and Gibb's free energy potentials,
- *Characterization* experiments that provide data for a particular material which are used to determine the material parameters, and
- *Verification* experiments that are used for a comparison between the predictions of the model and the actual material response.

In general, exploratory experiments may also be considered verification experiments and are the focus of this work. Characterization experiments normally consist of uniaxial loading at various temperatures and applying different strain rates.

When a potential based theory (such as the GVIPS model) and thermodynamics of irreversible processes are used to describe the viscoplastic behavior of metals, the only information required to completely define the flow and evolution laws are the functional forms of the Gibb's free energy potential (G) and the dissipation potential (Ω). Geometrically and thermodynamically based concepts, such as surfaces of constant inelastic strain rate (SCISRs), $\sqrt{\frac{2}{3} \dot{\epsilon}_{ij}^{in} \dot{\epsilon}_{ij}^{in}}$ and surfaces of constant dissipation rate (SCDRs), $\sigma_{ij} \dot{\epsilon}_{ij}^{in} - \alpha_{ij} \dot{\epsilon}_{ij}$, can be determined experimentally and used to describe the form of these potentials. SCDRs are the most theoretically meaningful (see Lissenden and Arnold, 1997) because they are directly proportional to Ω , even for anisotropic material behavior (SCISRs and SCDRs are proportional only for J_2 -type initial flow behavior). Also, as a result of the proportionality between SCDRs and Ω the directions of the inelastic strain rate vectors are mathematically normal to the SCDRs.

SCDRs are difficult to determine from experiments, however, because by definition the current value for the back stress, α_{ij} , must be known. However,

if the assumption is made that α_{ij} remains constant throughout the loading history (e.g., Clinard and Lacombe, 1988) then the dissipation rate $(\sigma_{ij}\dot{\epsilon}_{ij}^{in} - \alpha_{ij}\dot{\lambda}_{ij})$ is in essence equal to the inelastic power $(\sigma_{ij}\dot{\epsilon}_{ij}^{in})$ and SCDRs become surfaces of constant inelastic power (SCIPs).

SCIPs and SCISRs can be determined directly during experiments or using a post-experimental data reduction technique. In order to determine SCIPs or SCISRs during experiments, the inelastic strain rate must be calculated in real time (see Ellis and Robinson, 1985; Battiste and Ball, 1986; Lissenden et al., 1997). However, the presence of electronic noise makes this difficult. An alternative approach is to conduct small offset strain experiments (which are essentially the same as yield surface experiments) and then post-process the data to determine the inelastic strain rate which is free of electronic noise. This approach was followed by Clinard and Lacombe (1988) and is also the subject of the next chapter.

CHAPTER 6

RATE-DEPENDENT FLOW SURFACES

In this chapter, a procedure for determining rate-dependent flow surfaces is introduced and results are presented. Section 6.1 describes how the yield surface data from the preceding chapters is reduced and relates them to a similar procedure that was developed and implemented by Clinard and Lacombe (1988). Surfaces of constant inelastic strain rate (SCISRs) and surfaces of constant inelastic power (SCIPs) are presented and discussed in section 6.2.

6.1 Data Reduction Methodology

A FORTRAN software program was written to post-process the experimental data that was presented in Chapter 4. The experimental data from each probe are post-processed in order to fit a polynomial to the inelastic strain data and eliminate the electronic noise. The inelastic strain rate is then calculated and used in a flow surface definition to determine a point on the flow surface.

6.1.1 Basic Assumptions

The data file from a probe of the yield surface contains six columns of data: the probe time (t), axial stress (σ_{11}), shear stress (σ_{12}), axial strain (ε_{11}), tensorial shear strain (ε_{12}), and diametral strain (ε_{22}). The data in these files are read and stored in two arrays, one for the loading data and one for the unloading data, however only the loading data is used for the data reduction. The diametral strain (ε_{22}) is stored in the arrays, but is not currently used in the data reduction.

The following assumptions are made concerning the experimental data:

1. The initial axial and shear stress-strain responses for each probe are assumed to be linear elastic and characterized by E and σ_{11}^o for axial loading and G and σ_{12}^o for torsional loading (E , G , σ_{11}^o , and σ_{12}^o were defined in Chapter 3).
2. For each probe, the onset of inelastic deformation is assumed to occur at threshold times, t_{oa} and t_{os} , defined separately for axial and shear deformation, respectively.
3. Any offset strain that occurs after the threshold time is assumed to be inelastic strain (as opposed to nonlinear elastic strain, damage, or anything else).

These assumptions provide the foundation for determining the axial and shear inelastic strain rates, which is the main task of the data reduction procedure.

6.1.2 Determination of Elastic Constants

A least-squares regression technique is used to fit linear equations to the initial axial and shear stress-strain data, as was done in real time by the control program during an experiment. The resulting equations are

$$\sigma_{11} = E\varepsilon_{11} + \sigma_{11}^o \quad (6.1)$$

$$\sigma_{12} = 2G\varepsilon_{12} + \sigma_{12}^o \quad (6.2)$$

Usually the axial and shear prestresses are small, but even small prestresses are important when calculating the very small inelastic strains discussed below.

Equations (6.1) and (6.2) are linearly regressed over a predefined time range, t_a to t_b . The first few data points typically exhibit abnormally high scatter due to factors associated with the testing equipment. Therefore, the regression normally begins several seconds after the initiation of loading and ends prior to reaching the proportional limit.

6.1.3 Determination of the Inelastic Strains and Thresholds

The linear regression constants (E , G , σ_{11}^o , and σ_{12}^o) are used to determine the inelastic axial and shear strain components

$$\varepsilon_{11}^i = \varepsilon_{11} - \frac{\sigma_{11} - \sigma_{11}^o}{E} \quad (6.3)$$

$$\varepsilon_{12}^{in} = \varepsilon_{12} - \frac{\sigma_{12} - \sigma_{12}^o}{2G} \quad (6.4)$$

and then individually plotted versus time, as shown in Figure 6.1 for ε_{11}^{in} .

The threshold time (t_{oa}) is first determined for the axial inelastic strain. This is done graphically on the computer screen by visually identifying the point where inelastic strain begins to occur. In the presence of stiffening (Chapter 4), the inelastic strain is assumed to begin at the point of maximum stiffening. A sixth-order polynomial is then fit to the data between the threshold time (t_{oa}) and the time corresponding to the stress reversal (t_r) (Fig. 6.1). The process of identifying the threshold is often repeated several times until a satisfactory polynomial fit is obtained. Once a polynomial has been adequately fit to the axial data, the same procedure is repeated for the shear data.

It is important to note that on occasion the data from a probe is not adequate for use in determining a point on the flow surface. That is, in some probes no significant inelastic strain occurs for one of the axial or shear responses. For example, a 12° probe angle (mostly tension) may not exhibit inelastic shear strain. On these occasions (which are rare) the data is treated as elastic.

6.1.4 Determination of Inelastic Strain Rates and Flow Surfaces

The inelastic strain rates are determined by simply differentiating the sixth-order polynomials that were fit to the actual data

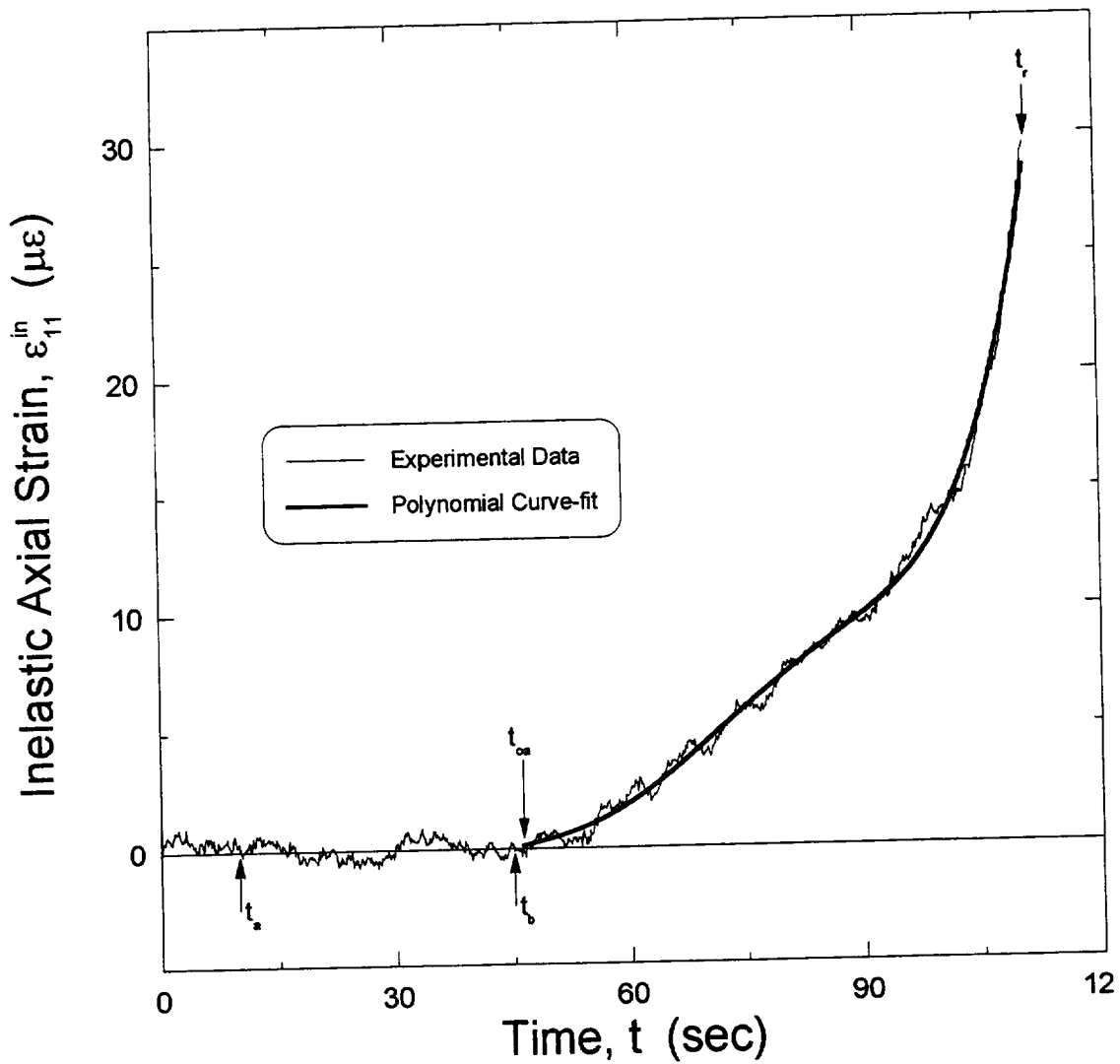


Figure 6.1 - Axial inelastic strain as a function of time and a sixth-order polynomial curve-fit.

$$\dot{\epsilon}_{11}^{in} = 6a_1t^5 + 5a_2t^4 + 4a_3t^3 + 3a_4t^2 + 2a_5t + a_6 \quad (6.5)$$

$$\dot{\epsilon}_{12}^{in} = 6b_1t^5 + 5b_2t^4 + 4b_3t^3 + 3b_4t^2 + 2b_5t + b_6 \quad (6.6)$$

where $a_1 - a_6$ and $b_1 - b_6$ are the polynomial fit coefficients.

Equations (6.5) and (6.6) are then substituted into the equivalent inelastic strain rate definition,

$$\dot{\epsilon}_e^{in} = \sqrt{\frac{2}{3} \dot{\epsilon}_{ij}^{in} \dot{\epsilon}_{ij}^{in}} = \sqrt{(\dot{\epsilon}_{11}^{in})^2 + \frac{4}{3} (\dot{\epsilon}_{12}^{in})^2} \quad (6.7)$$

to determine a SCISR; or the inelastic power definition,

$$\sigma_{ij} \dot{\epsilon}_{ij}^{in} = \sigma_{11} \dot{\epsilon}_{11}^{in} + 2\sigma_{12} \dot{\epsilon}_{12}^{in} \quad (6.8)$$

to determine a SCIP. The next step is to select a target value for the SCISR or SCIP. The time, t , required to satisfy the target value can be traced back to a value of σ_{11} and σ_{12} , as shown in Figure 6.2. A locus of points in the axial-shear stress plane is constructed by following this procedure for each of the probes resulting in a rate-dependent flow surface. In addition, the values of the inelastic strain rate components from Equations (6.5) and (6.6) evaluated at time t indicate the direction of the inelastic strain rate vector. According to the normality flow rule, the inelastic strain rate vectors should always be directed outward and normal to SCIPs.

6.1.5 Software Details

The FORTRAN software is capable of generating up to 20 different flow surfaces during one run. The stress points (σ_{11} and σ_{12}) and the inelastic

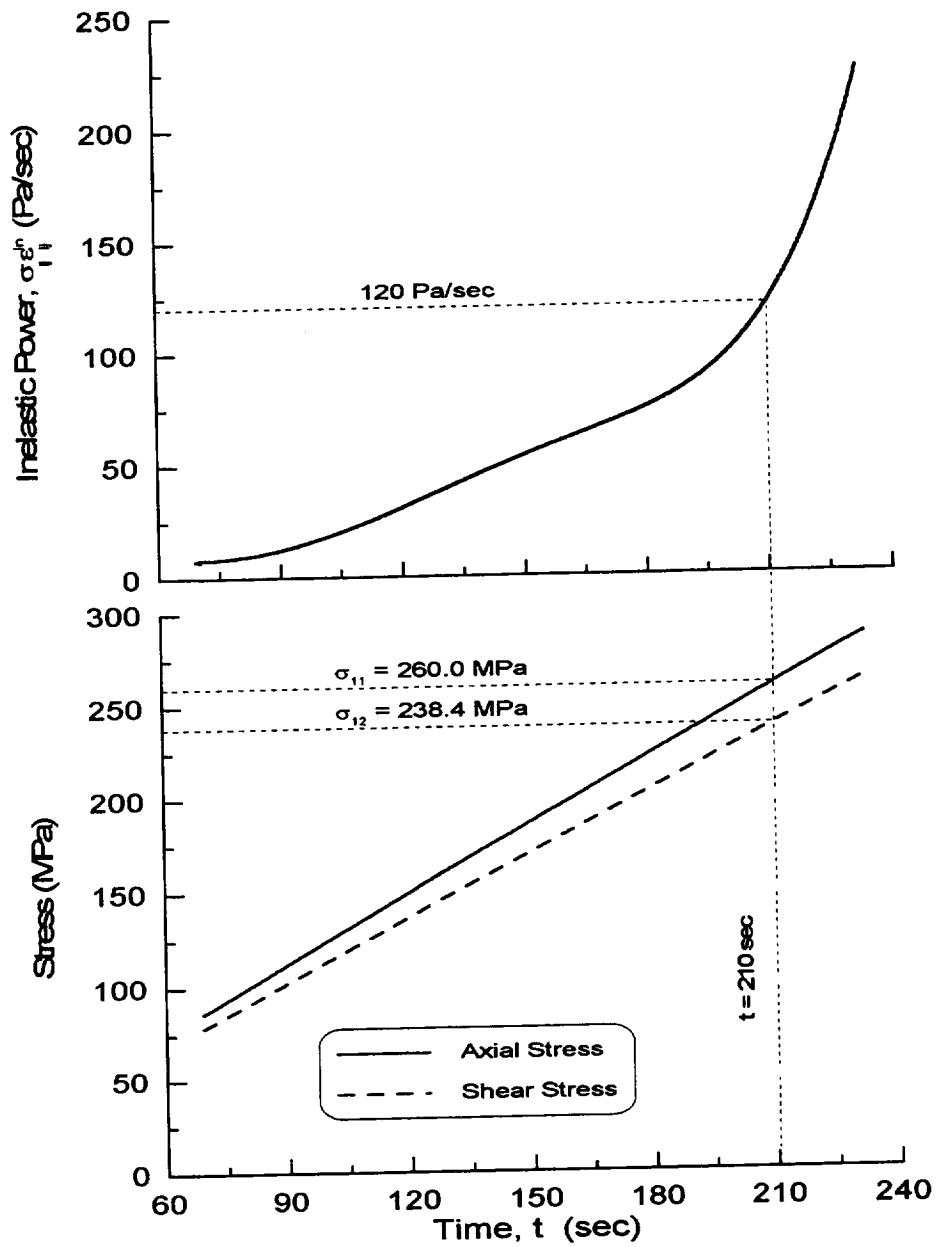


Figure 6.2 - Determination of time t and the stresses σ_{11} and σ_{12} associated with the target value.

strain rates ($\dot{\varepsilon}_{11}^{in}$ and $\dot{\varepsilon}_{12}^{in}$) for each flow surface are tabulated and written to an output file. This allows the loci and direction of the inelastic strain rate vectors associated with each stress point to be easily plotted.

Additional data for each probe is also recorded in a sequence of different output files. Each output file contains data for a specific probe, including loading and unloading. All of the original data from the experiments is recorded: the current probe time (t), the axial stress (σ_{11}), the shear stress (σ_{12}), the axial strain (ε_{11}), the tensorial shear strain (ε_{12}), and the diametral strain (ε_{22}). In addition, the post-processed data is recorded: the inelastic axial strain (ε_{11}^{in}), the inelastic shear strain (ε_{12}^{in}), the inelastic axial curve-fit (ε_{11}^{fit}), the inelastic shear curve-fit (ε_{12}^{fit}), the inelastic axial strain rate ($\dot{\varepsilon}_{11}^{in}$), and the inelastic shear strain rate ($\dot{\varepsilon}_{12}^{in}$).

6.1.6 Procedure of Clinard and Lacombe

Working from experimental data obtained by Battiste and Ball (1986), Clinard and Lacombe (1988) used a similar procedure to determine flow surfaces for 316 stainless steel. The differences between their approach and the current one are outlined in the following:

- The experimental data used by Clinard and Lacombe was collected from stress-controlled loading experiments, whereas strain-controlled loading was used in the current investigation. Since plastic deformation is rate-dependent at elevated temperatures, the inelastic strain rate under stress-

controlled loading can be significantly different than under strain-controlled loading. In fact, for strain controlled tests the inelastic strain rate is limited to the applied strain rate. No such limitation exists for stress controlled tests.

- Clinard and Lacombe assumed the linear portion of the stress-strain curves to be fully characterized by only two elastic constants (E and G). In the current procedure, an equation of the form $\sigma = E\varepsilon + \sigma_o$ is used.
- Clinard and Lacombe assumed that the threshold time for a given probe was the same for both axial and shear strains. Here, two different threshold times may be used.
- A second-order polynomial is used by Clinard and Lacombe to approximate the inelastic strain versus time curve. In the current work, a sixth-order polynomial gave a much better representation of the data.
- Clinard and Lacombe determined the threshold and polynomial fit from the equivalent inelastic strain and then differentiated the polynomial to obtain an equivalent inelastic strain rate. This approach requires that a particular relationship be used to combine the inelastic strain components. In the current work, the threshold was determined separately for each inelastic strain component, after which the individual inelastic strain rates were determined and substituted into a flow surface definition.

6.2 SCISR and SCIP Results

Surfaces of constant inelastic strain rate (SCISRs) and surfaces of constant inelastic power (SCIPs) were determined for solutioned and aged IN718 using the experimental data from the experiments in Chapter 4. In subsection 6.2.1, initial SCISRs and SCIPs are shown for solutioned IN718 at 23 and 371°C. Subsequent surfaces are shown at 454°C. Subsection 6.2.2 shows initial SCISRs and SCIPs for aged IN718 at 23 and 649°C and subsequent surfaces at 649°C.

6.2.1 Solutioned Inconel 718

SCISRs and SCIPs were determined using the procedure described in section 6.1 for solutioned IN718 at 23, 371, and 454°C. A trial and error procedure was used for choosing the target values, since the values of $\dot{\epsilon}_{eq}^{in}$ and $\sigma_{ij}\dot{\epsilon}_{ij}^{in}$ (for SCISRs and SCIPs, respectively) at t_r are different for each probe. One target value was chosen for $\dot{\epsilon}_{eq}^{in}$ and was based on the largest value for which a point on the SCISR could be obtained from all (or nearly all) of the probes. A similar process was used to determine the target value for SCIPs. In most cases, a smaller target value of $\sigma_{ij}\dot{\epsilon}_{ij}^{in}$ was also used.

In Figure 6.3 an initial SCIP is plotted along with the corresponding SCISR at 23°C to compare the shapes of the two flow surface definitions. A target value of 120 Pa/sec was found to be suitable for the SCIP. To facilitate

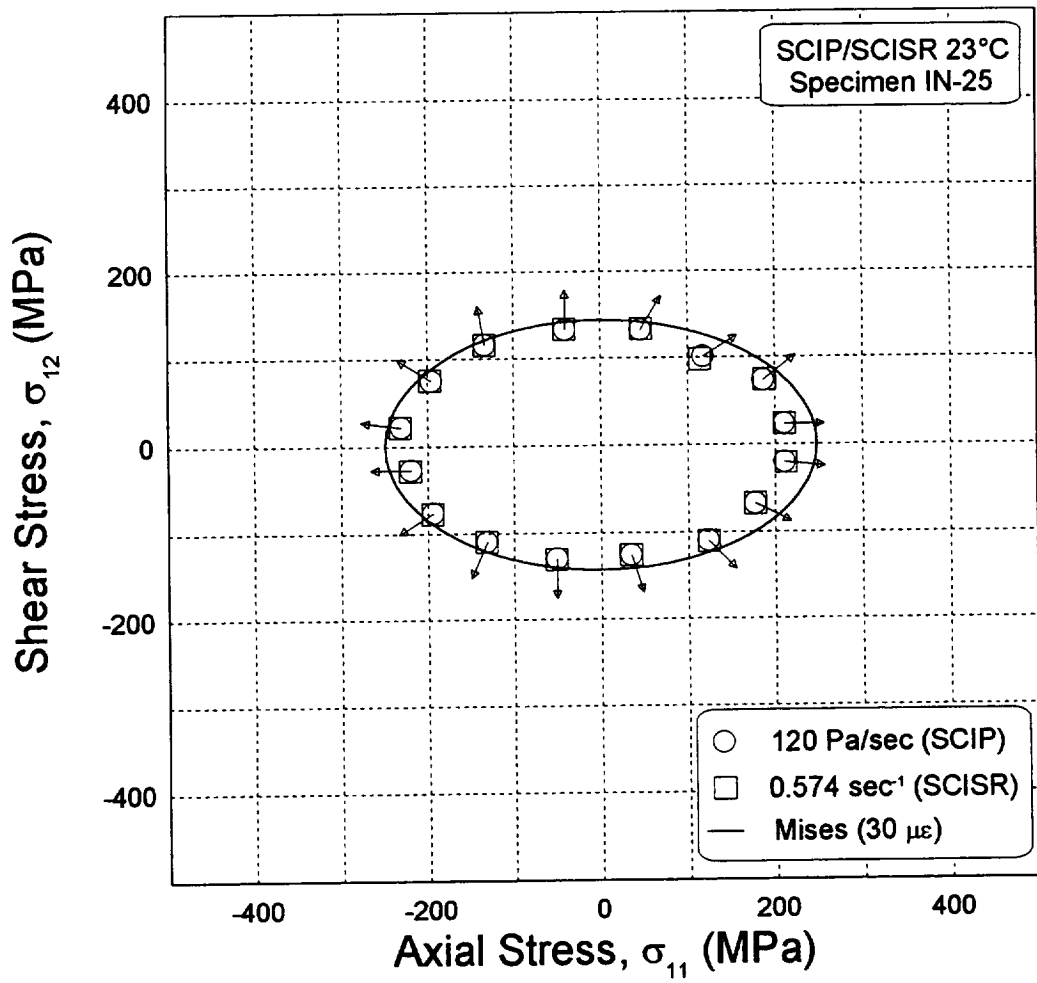


Figure 6.3 - Initial SCISR and SCIP for solutioned IN718 at 23°C.

this comparison, the target value of $\dot{\epsilon}_{eq}^{in}$ that corresponded to $\bar{\sigma}_{ij} \dot{\epsilon}_{ij}^{in} = 120$ Pa/sec was determined for the first probe (12° probe angle). The target value for the SCISR was determined to be 0.574 sec⁻¹. Figure 6.3 shows that for all intents and purposes the SCISR and SCIP are the same and also compare favorably with the 30 $\mu\epsilon$ Mises ellipse in the axial-shear stress plane. This suggests that at 23°C solutioned IN718 displays J_2 -type initial flow behavior, in which the SCISRs and SCIPs are theoretically proportional (see Lissenden and Arnold, 1997). Figure 6.3 also shows the directions of the inelastic strain rate vectors (magnitudes are not indicated) for the SCIP, which to a reasonable approximation, are normal to the SCIP.

A SCISR is plotted in Figure 6.4 for solutioned IN718 at 371°C, where a target value of 0.75 sec⁻¹ was chosen. In Figure 6.5, two SCIPs are shown for target values of 60 and 120 Pa/sec. Again, both flow surface definitions agree with the 30 $\mu\epsilon$ Mises ellipse. Furthermore, the directions of the inelastic strain rate vectors, plotted for the 120 Pa/sec SCIP, appear to be approximately normal to the ellipse.

In Figure 6.6, a SCISR was determined at 454°C after a proportional prestrain of 500 $\mu\epsilon$ offset. The data can be compared with the experimental yield points that were plotted in Figure 4.9. The shape of the loci are similar, however the SCISR appears to be translated less and no cross effect is observed. A similar observation is made for the SCIPs in Figure 6.7.

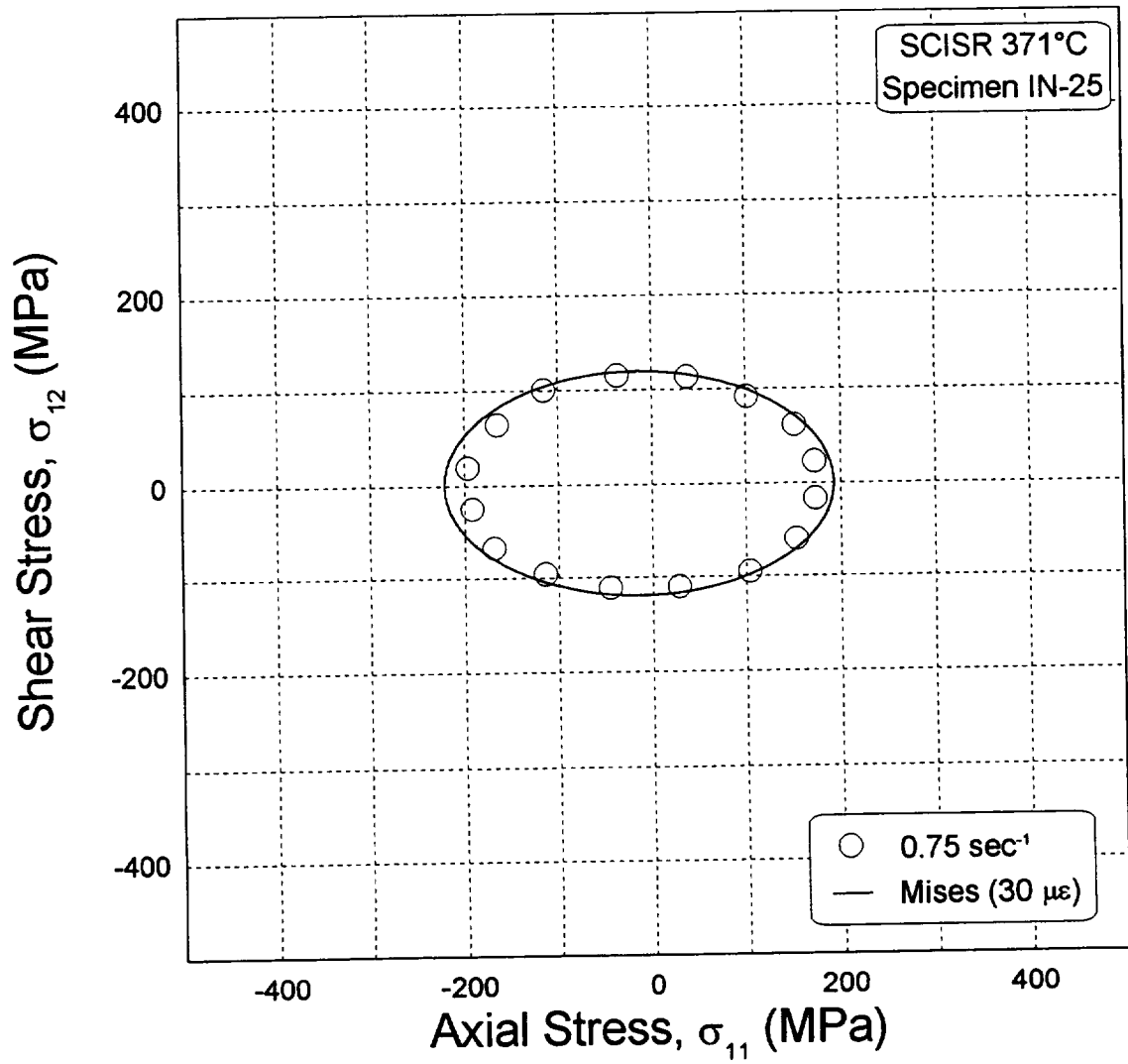


Figure 6.4 - Initial SCISR for solutioned IN718 at 371°C.

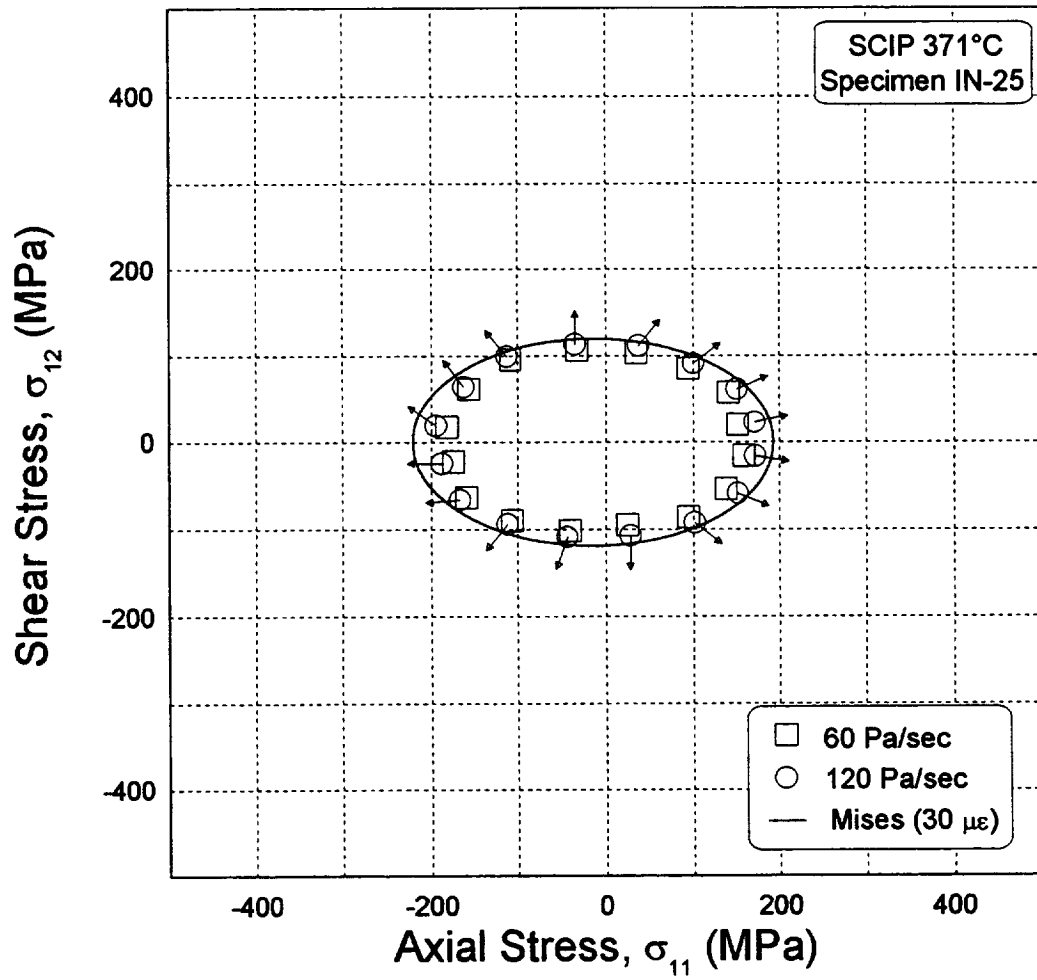


Figure 6.5 - Initial SCIPs for solutioned IN718 at 371°C.

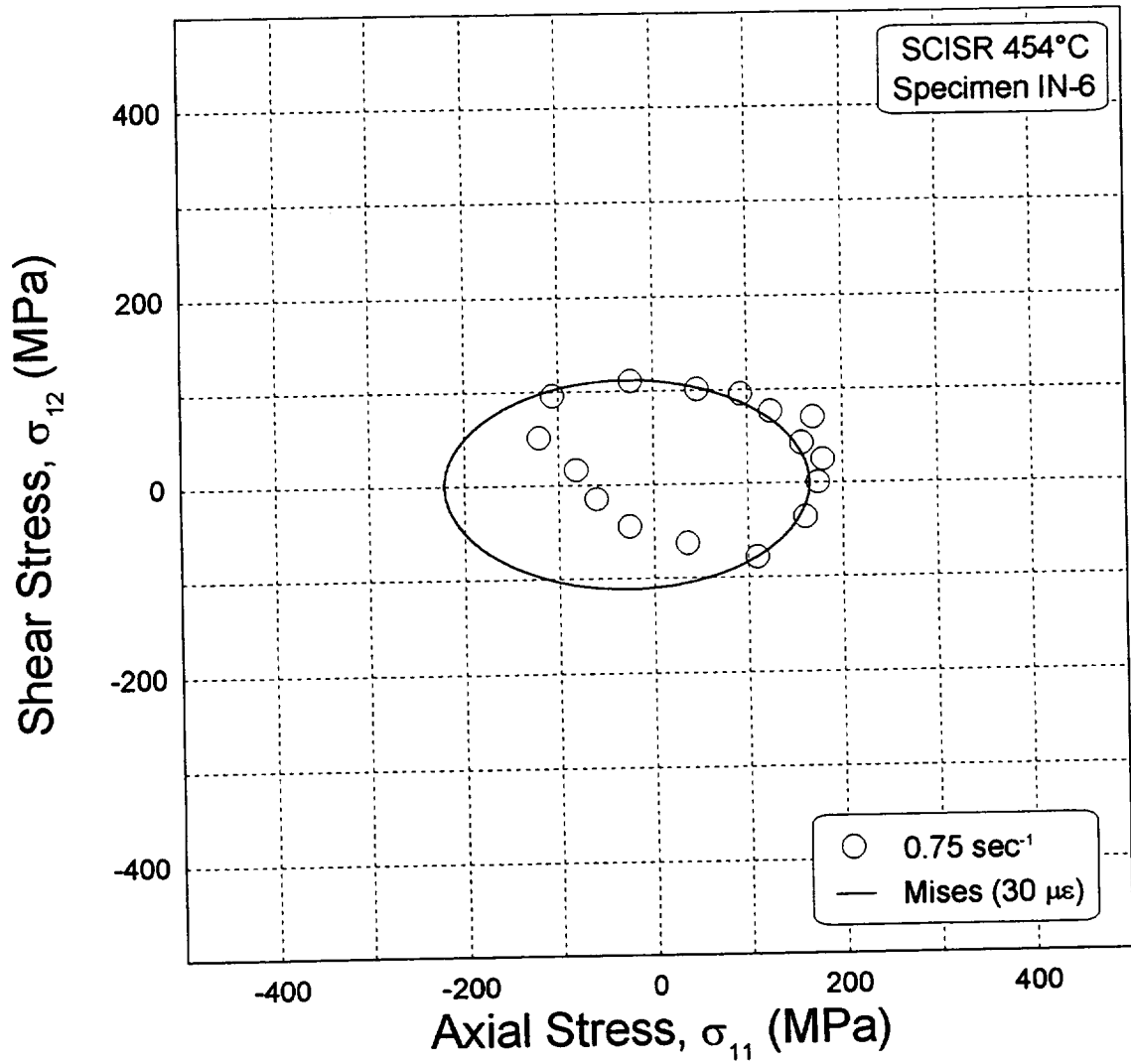


Figure 6.6 - Subsequent SCISR for solutioned IN718 at 454°C after a proportional prestrain of 500 $\mu\epsilon$ offset.

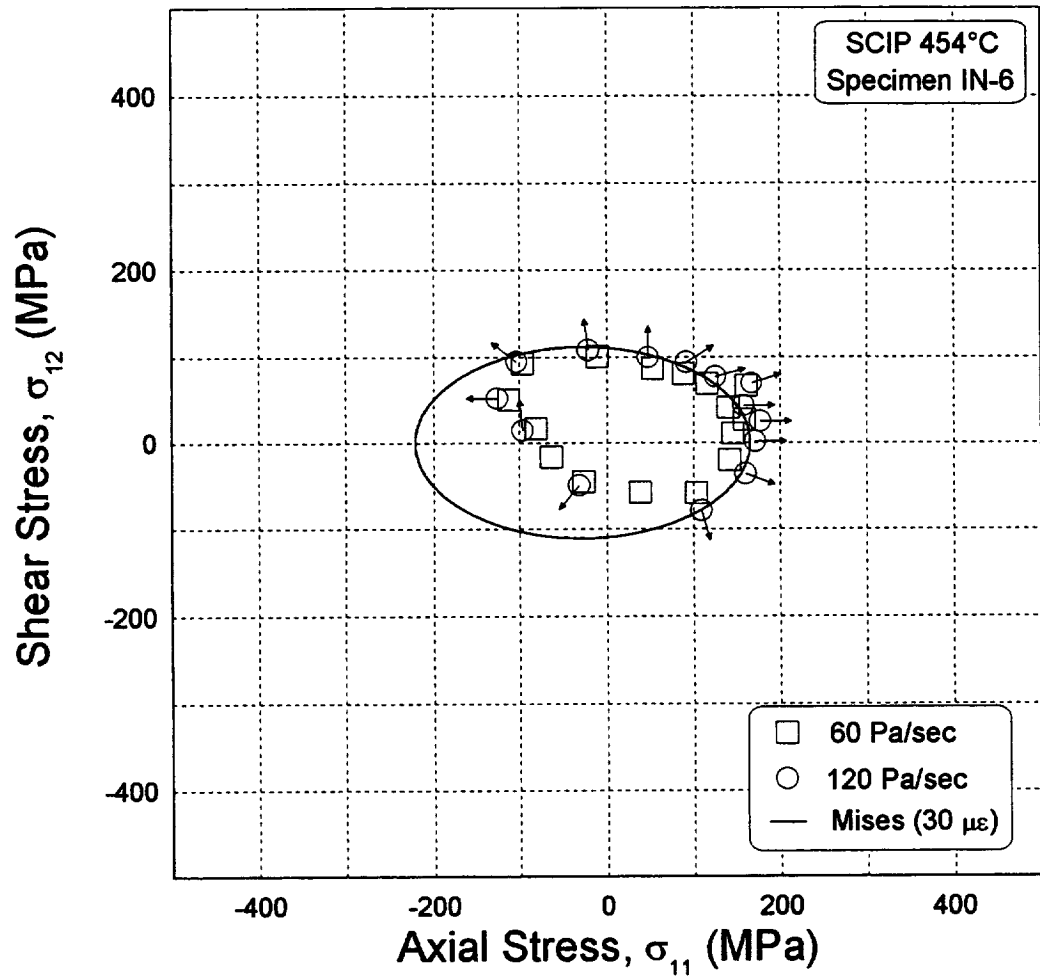


Figure 6.7 - Subsequent SCIPs for solutioned IN718 at 454°C after a proportional prestrain of 500 $\mu\epsilon$ offset.

6.2.2 Aged Inconel 718

An initial SCISR and initial SCIPs for aged IN718 at 23°C are plotted in the axial-shear stress plane in Figures 6.8 and 6.9, respectively. The centers of the flow surfaces are offset from the origin of the stress plane in the compression direction, and are similar in shape to the offset Mises ellipse. The maximum target value that could be achieved for the SCISR was 0.25 sec^{-1} . This is significantly less than the target value for solutioned IN718, suggesting that the inelastic strain rate for aged IN718 is less than the inelastic strain rate for solutioned IN718 for equal applied strain rates and a similar level of inelastic strain. This seems reasonable since aged IN718 exhibits more hardening. Also, the directions of the inelastic strain rate vectors appear to be reasonably normal to the 120 Pa/sec SCIP.

Figures 6.10 and 6.11 show an initial SCISR and initial SCIPs, respectively at 649°C. Both flow definitions are similar in shape to each other and to the $30 \mu\epsilon$ Mises ellipse. Aside from the expected decrease in size and additional scatter due to the electronic noise, the SCISR and SCIPs at 649°C appear similar to the flow surfaces at 23°C.

Finally, subsequent SCISRs and SCIPs are shown in Figures 6.12-6.15. Figure 6.12 shows a 0.25 sec^{-1} SCISR after a proportional prestrain of $500 \mu\epsilon$ offset at 649°C. In Figure 6.13, 60 and 120 Pa/sec SCIPs are shown along with the directions of the inelastic strain rate vectors for the 120 Pa/sec SCIP.

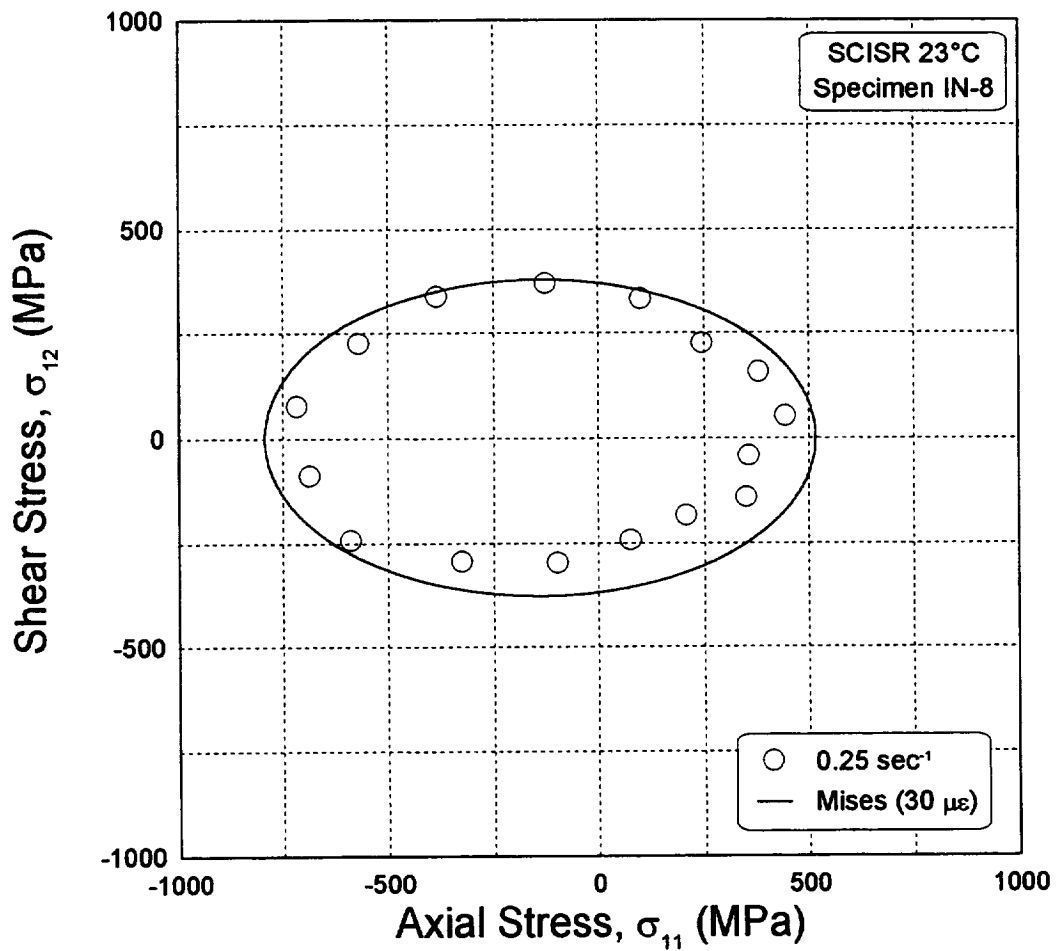


Figure 6.8 - Initial SCISR for aged IN718 at 23°C.

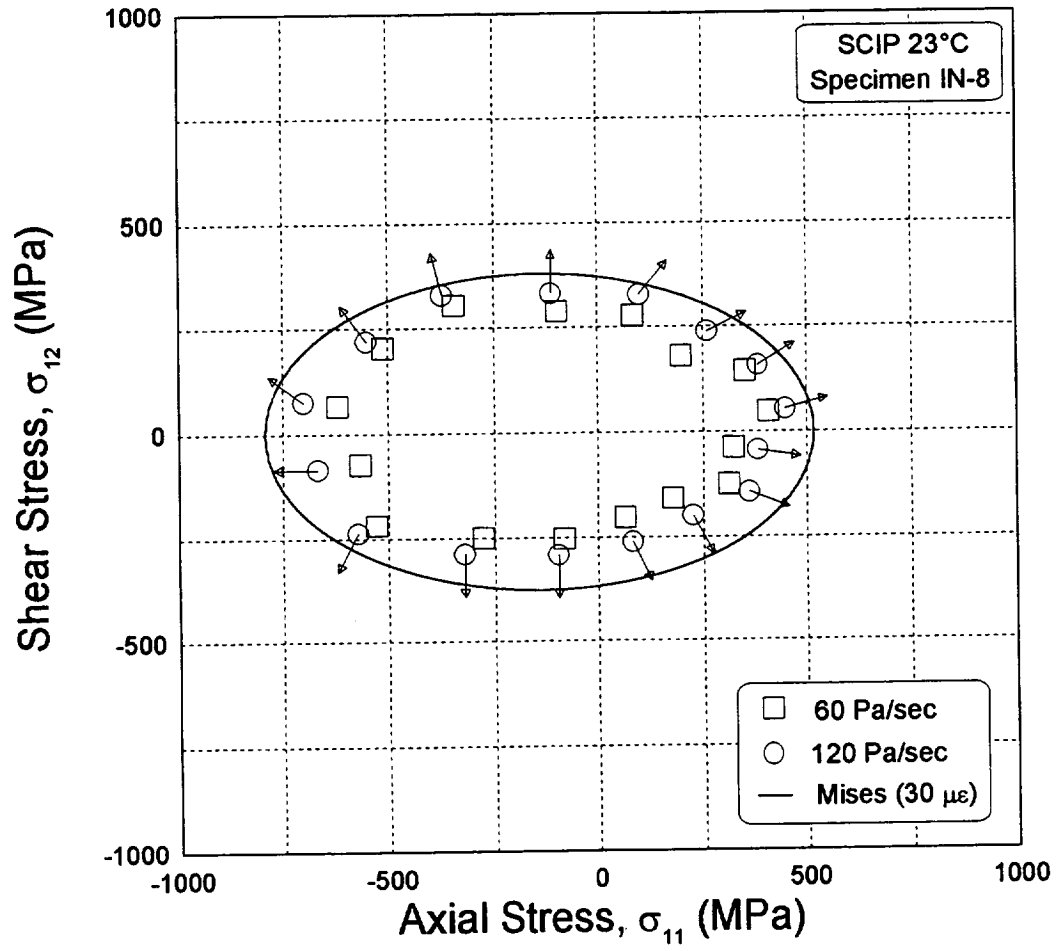


Figure 6.9 - Initial SCIPs for aged IN718 at 23°C.

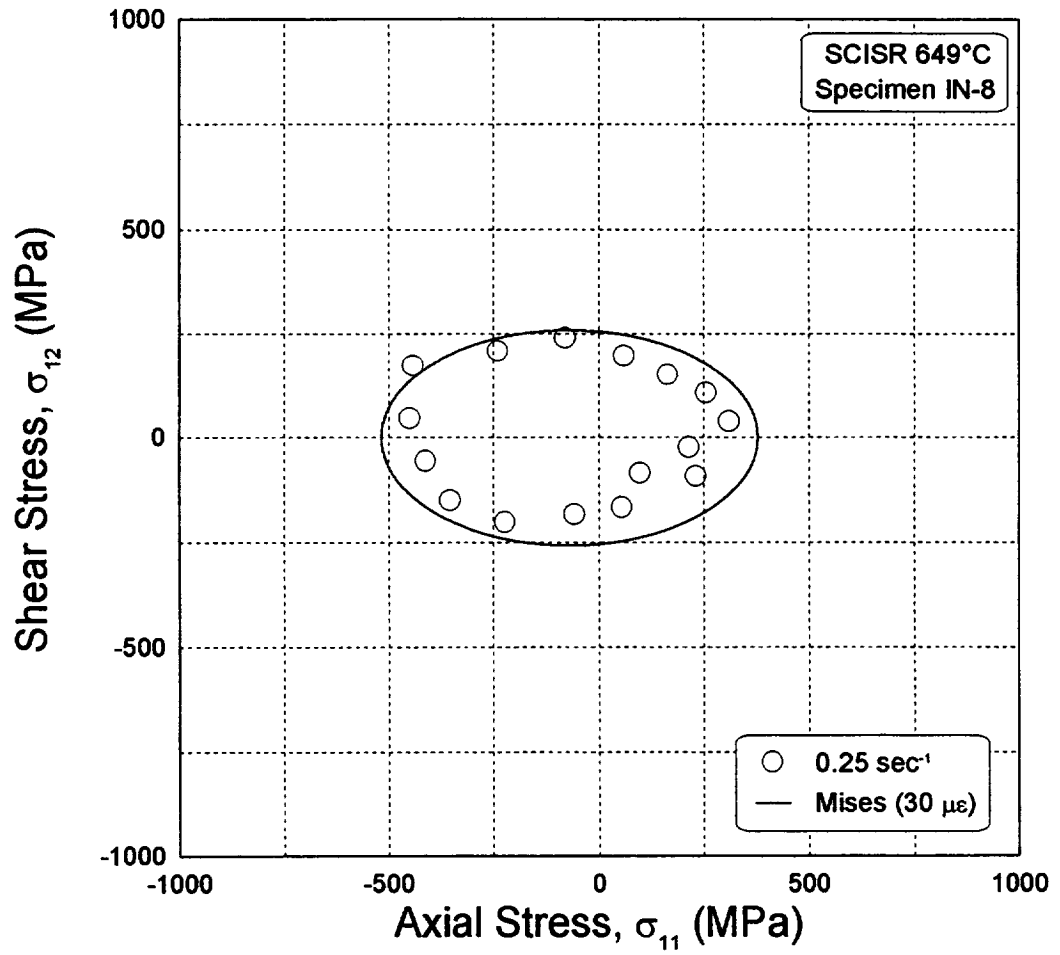


Figure 6.10 - Initial SCISR for aged IN718 at 649°C.

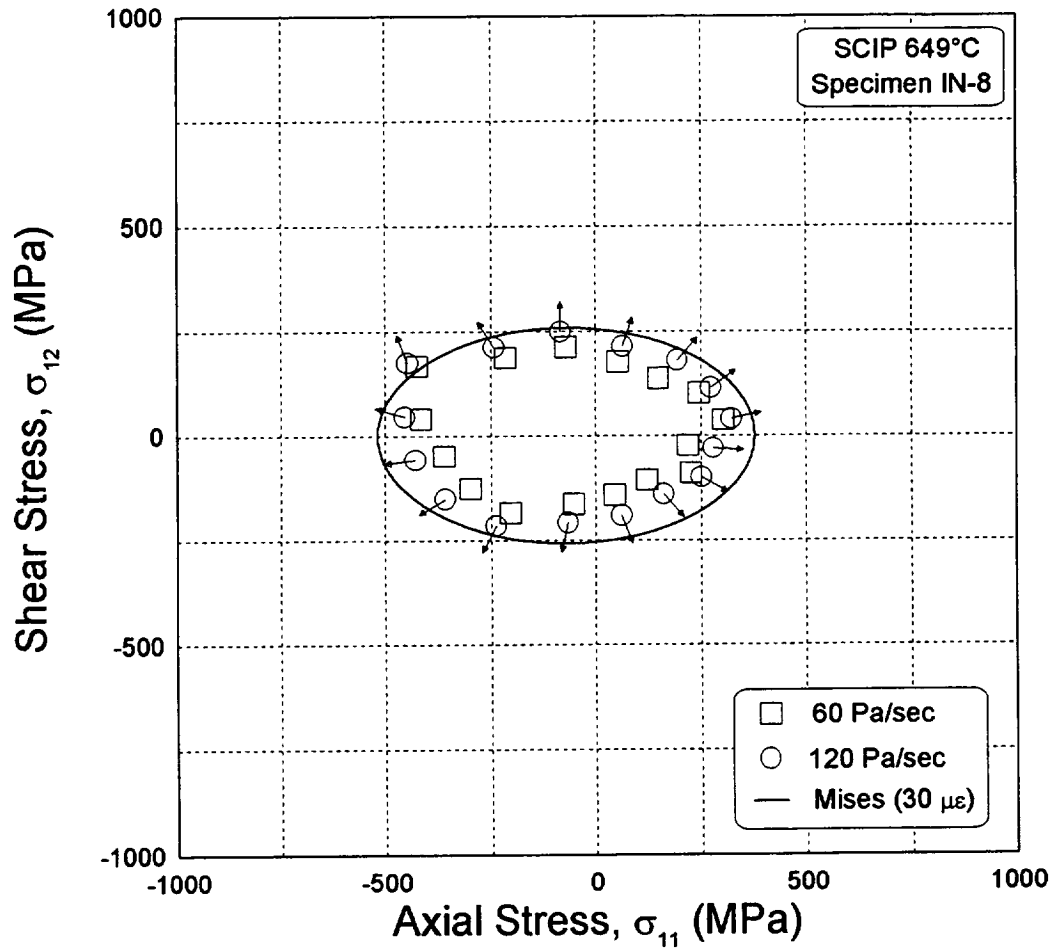


Figure 6.11 - Initial SCIPs for aged IN718 at 649°C.

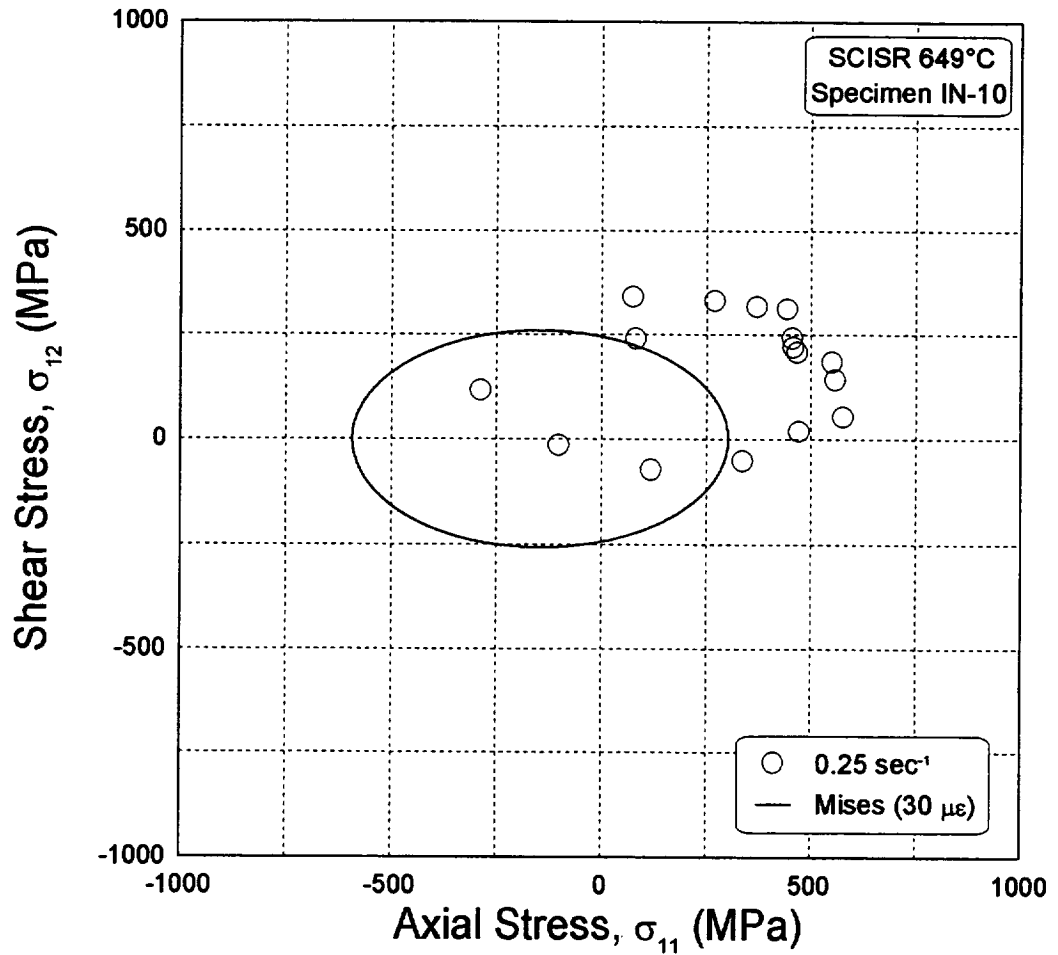


Figure 6.12 - Subsequent SCISR for aged IN718 at 649°C after a proportional prestrain of $500 \mu\epsilon$ offset.

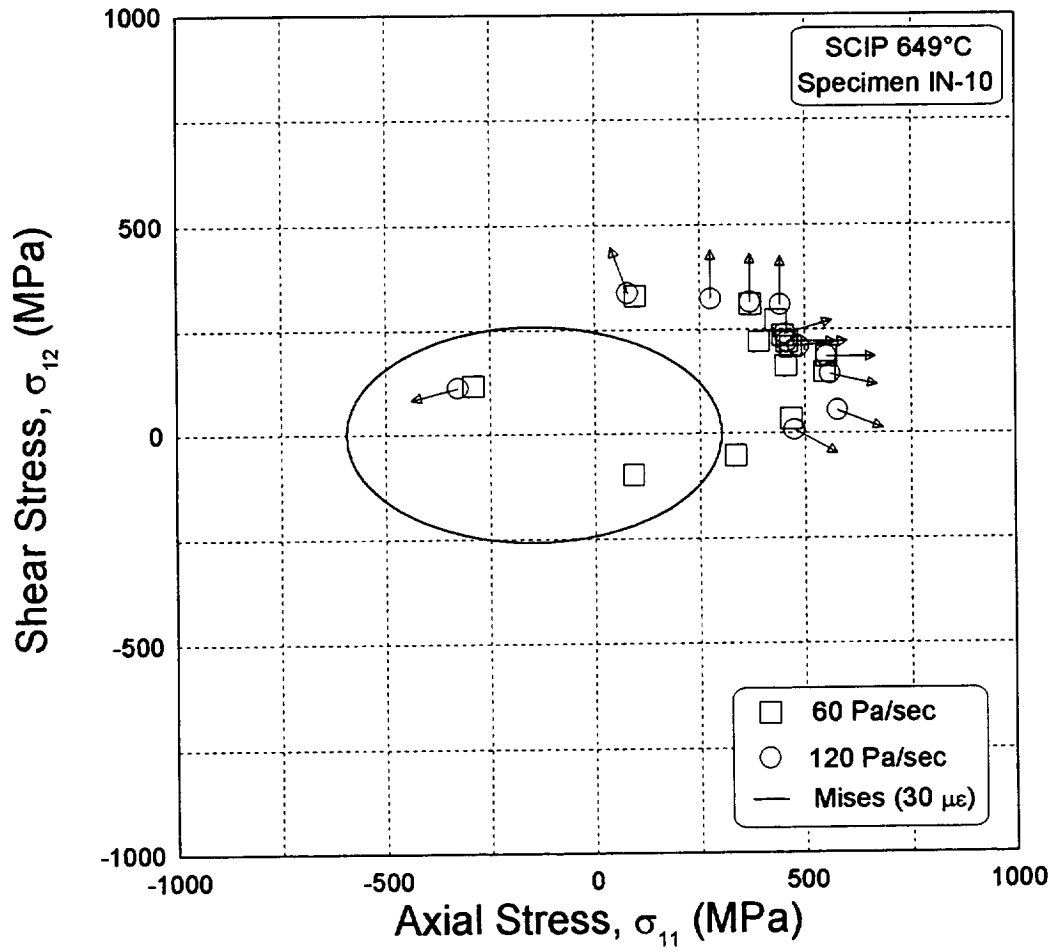


Figure 6.13 - Subsequent SCIPs for aged IN718 after a proportional prestrain of 500 $\mu\epsilon$ offset.

(The subsequent yield surface was plotted in Figure 4.20.) Figure 6.14 shows a 0.25 sec^{-1} SCISR following a $9000 \mu\epsilon$ tensile prestrain. Likewise, 60 and 120 Pa/sec SCIPs are plotted in Figure 6.15. See Figure 4.21 for a comparison with the subsequent yield surface.

In general, all of the flow surfaces appear to be similar in shape to the yield surfaces that were discussed in Chapter 4. This indicates that the appropriate form of the generalized dissipation potential for aged IN718 should give a similar result for yield loci, SCISRs, and SCIPs when equivalent target values are used.

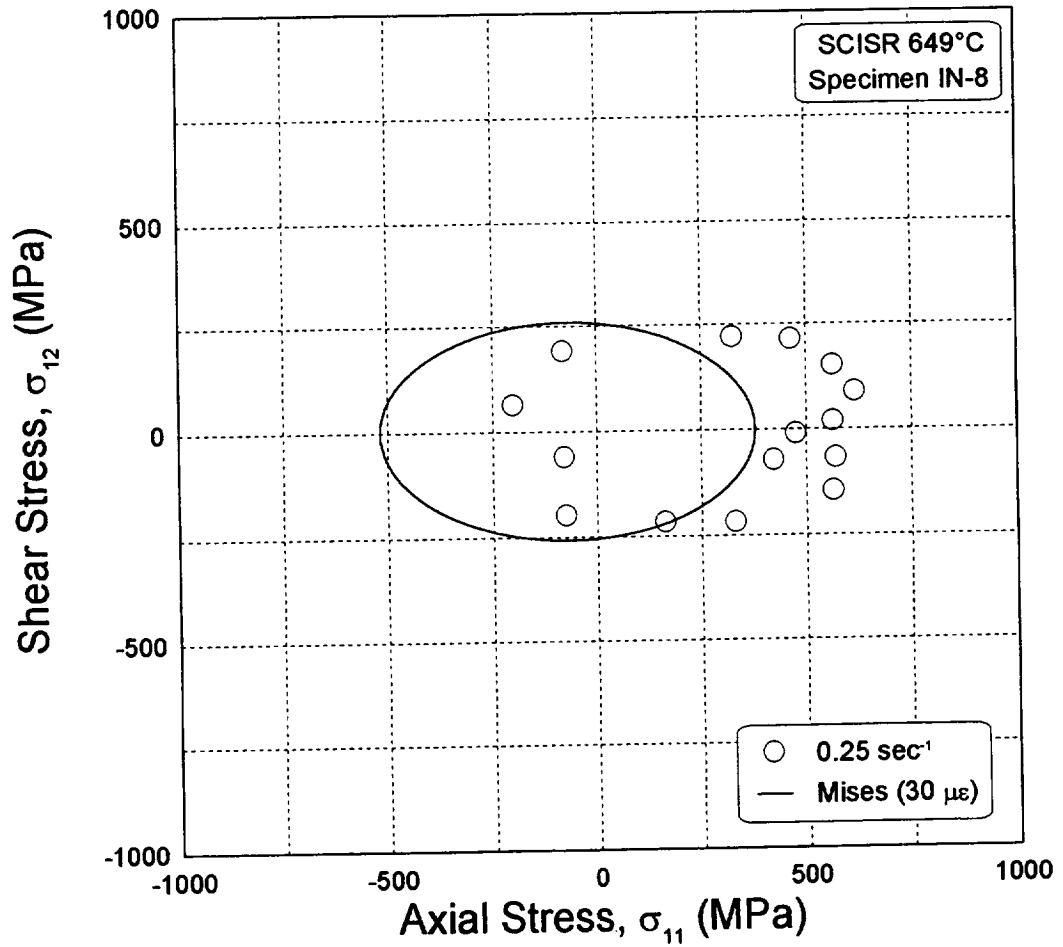


Figure 6.14 - Subsequent SCISR for aged IN718 after a tensile prestrain of $9000 \mu\epsilon$ (0.9%).

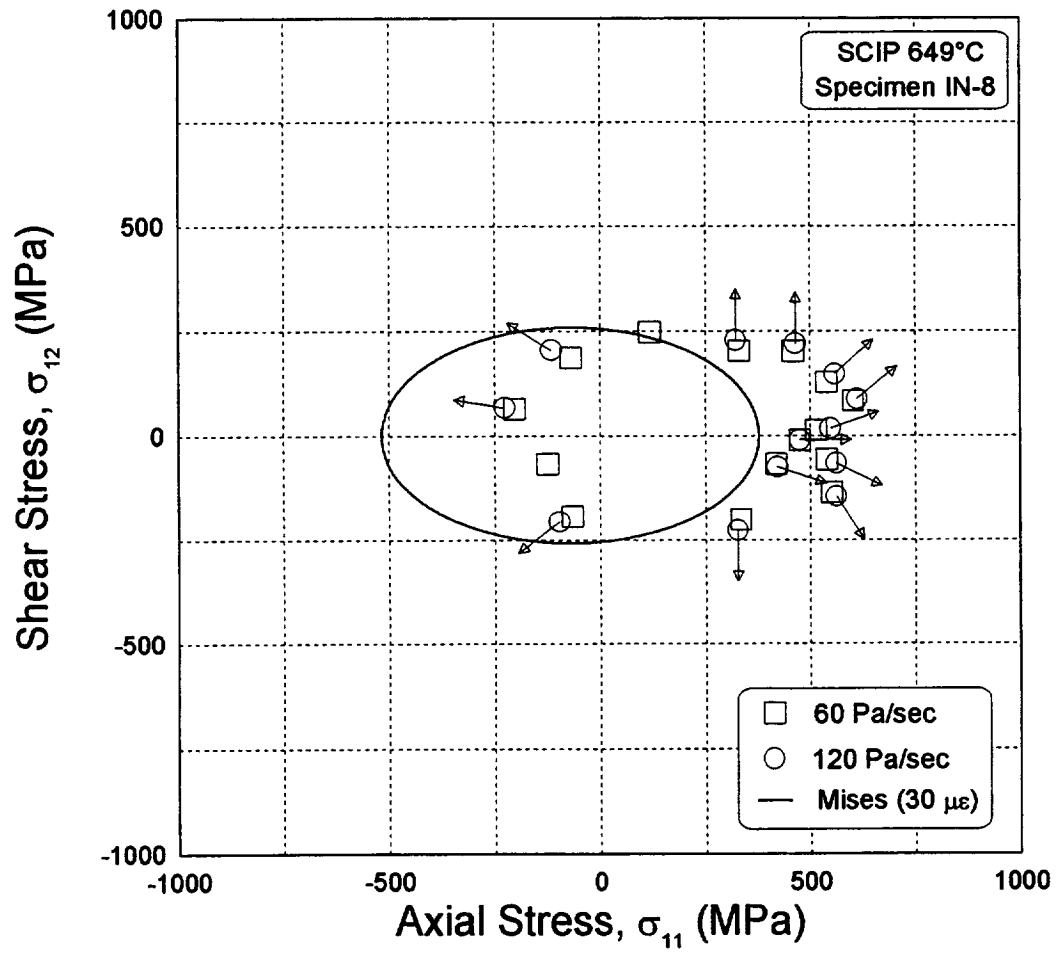


Figure 6.15 - Subsequent SCIPs for aged IN718 after a tensile prestrain of 9000 $\mu\epsilon$ (0.9%).

CHAPTER 7

SUMMARY, CONCLUSIONS, AND FUTURE WORK

This chapter provides a summary of the investigation on yield and flow surfaces for Inconel 718 and discusses additional issues that should be considered in future work in this area. Section 7.1 gives a brief summary of the work that was performed and documented throughout this thesis. In section 7.2, a list of conclusions are given. Finally, section 7.3 suggests future work involving yield and flow surface experiments.

7.1 Summary

Small offset yield loci experiments were performed on solutioned and aged specimens of Inconel 718 under combined axial-torsional loading over a wide temperature range (23-649°C). These experiments are unprecedented for precipitation hardened alloys at service temperatures. Initial and subsequent yield loci experiments involving determination of entire loci from a single specimen were successful largely because the biaxial extensometer was capable of precise strain measurement. It is interesting to note that some IN718 specimens were successfully re-solutioned to restore the material to a

near-virgin state after determination of subsequent flow surfaces. SCISRs and SCIPs were successfully determined using a new procedure for post-processing flow surfaces. This work opens the door for more detailed studies on hardening behavior at high temperatures.

7.2 Conclusions

The following general conclusions can be made based on the results of these experiments.

- The von Mises yield criterion fit the initial yield loci in the axial-shear stress plane very well if an initial offset, or strength-differential is considered. The strength-differential may be due to nonlinear elasticity (dislocation-precipitate interactions) and/or the effect of hydrostatic stress (increased dislocation density).
- Initial and subsequent SCISRs and SCIPs for both solutioned and aged IN718 are similar in size and shape to the yield loci in the axial-shear stress plane.
- Subsequent yield loci indicate hardening to be predominantly kinematic and secondarily distortional. In addition, there may be a slight cross effect for solutioned IN718.
- Aged IN718 displays significantly more hardening behavior than solutioned IN718.

- Re-solutioning lightly deformed (< 1% total strain) specimens can effectively return the specimens to the virgin (or near-virgin) material state.

7.3 Future Work

As mentioned, this work opens the door for a more in-depth study of hardening behavior at high temperatures. Now that these type of tests have been successful, additional work is needed to further investigate the high temperature deformation behavior of metals. Furthermore, there were some issues associated with IN718 that were not completely resolved and should be investigated in more detail. These are listed below.

- Initial yield loci and flow surfaces for aged IN718 exhibited a strong strength-differential that increased with increasing temperature. Tension and compression tests to a larger strain magnitude at various temperatures will help to determine the mechanism causing this behavior.
- The stress-strain response in compression for aged IN718 exhibited a nonlinear elastic response prior to the onset of plastic deformation, however it was unclear whether a similar, but opposite response was occurring in tension. Incremental loading/unloading tests in compression and tension using strain gages to measure strain should offer more information regarding this behavior.

- In the experiments reported here a constant strain rate of $10 \mu\text{s}/\text{sec}$ was used throughout. To determine the rate-dependent hardening behavior of IN718, more experiments should be performed using various strain rates.
- The small offset yield experiments are convenient since an entire locus can be determined from a single specimen. However, the drawback of these experiments is that only a small family of flow surfaces can be determined. Experiments that determine one yield point for each specimen can provide a much larger range of families of flow surfaces since larger excursions into the plastic region can be achieved.
- Further investigation into the re-solutioning of specimens will provide important information and may reduce the number of specimens needed for large scale yield experiments.

REFERENCES

- Abdel-Kader, M.S., Eftis, J., and Jones, D.L. (1986). "Modeling the Viscoplastic Behavior of Inconel 718 at 1200°F," *NASA Conference Publication 10010: Nonlinear Constitutive Relations for High Temperature Applications*, pp. 37-68.
- Althoff, J. and Wincierz, P. (1972). "The Influence of Texture on the Yield Loci of Copper and Aluminum," *Zeitschrift Flur Metallkunde*, Vol. 63, pp. 623-633.
- Arnold, S.M., Saleeb, A.F., and Castelli, M.G. (1996). "A Fully Associative, Nonisothermal, Nonlinear Kinematic, Unified Viscoplastic Model for Titanium Alloys," *Thermo-Mechanical Fatigue Behavior of Materials: Second Volume*, eds. M. J. Verrilli and M. G. Castelli, ASTM STP-1263, American Society for Testing and Materials, Philadelphia, pp. 146-173.
- Battiste, R.L. and Ball, S.J. (1986). "Determination of Surfaces of Constant Inelastic Strain Rate at Elevated Temperature," *NASA Conference Publication 2444: Turbine Hot Section Technology*, pp. 307-325.
- Bland, D.R. (1957). "The Associated Flow Rule of Plasticity," *Journal of the Mechanics and Physics of Solids*, Vol. 6, p. 71.
- Bodner, S.R. and Partom, Y. (1975). "Constitutive Equations for Elastic-Viscoplastic Strain Hardening Materials," *Journal of Applied Mechanics*, Vol. 24, p. 283.
- Bodner, S.R. (1987). "Review of a Unified Elastic-Viscoplastic Theory," *Unified Constitutive Equations for Creep and Plasticity*, A. K. Miller, ed., Elsevier Applied Science, Barking, Essex, England.
- Chaboche, J.L. (1977). "Viscoplastic Constitutive Equations for the Description of Cyclic and Anisotropic Behavior of Materials," *Bull. Acad. Pol. Sci. Sér. Sci. Tech.*, Vol. 25, p. 33.
- Chait, R. (1973). "The Strength Differential of Steel and Ti Alloys as Influenced by Test Temperature and Microstructure," *Scripta Metallurgica*, Vol. 7, no. 4, pp. 351-354.

Clinard, J.A. and Lacombe, C. (1988). "Determination of Multiaxial Flow Surfaces at Elevated Temperatures Using the Concept of Dissipation Potential," *ORNL/TM-10787*, Oak Ridge National Laboratory, Oak Ridge, TN, April.

Drucker, D.C. (1973). "Plasticity Theory, Strength-Differential (SD) Phenomenon, and Volume Expansion in Metals and Plastics," *Metall. Trans.*, Vol. 4, pp. 667-673.

Ellis, J.R., Robinson, D.N., and Pugh, C.E. (1983). "Time Dependence in Biaxial Yield of Type 316 Stainless Steel at Room Temperature," *Journal of Engineering Materials and Technology*, Vol. 105, pp. 250-256.

Ellis, J.R. and Robinson, D.N. (1985). "Experimental Determination of Flow Potential Surfaces Supporting a Multiaxial Formulation of Viscoplasticity," *NASA Conference Publication 2405: Turbine Engine Hot Section Technology*, pp. 259-269.

Ellis, J.R. and Bartolotta, P.A. (1997). "Adjustable Work Coil Fixture Facilitating the Use of Induction Heating in Mechanical Testing," *Multiaxial Fatigue and Deformation Testing Techniques, ASTM STP 1280*, S. Kalluri and P.J. Bonacuse, Eds., American Society for Testing and Materials, pp. 43-62.

Fournier, D. and Pineau, A. (1977). "Low Cycle Fatigue Behavior of Inconel 718 at 298 K and 823 K," *Metall. Trans.* Vol. 8A, pp. 1095-1105.

Gil, C.M., Lissenden, C.J., and Lerch, B.A. (1998). "An Investigation of Anomalous Behavior in Metallic-Based Materials Under Compressive Loading," *NASA TM-206640*, NASA Lewis Research Center, Cleveland, Ohio (in press).

Greenstreet, W.L. (1977). "Structural Analysis Technology for High-Temperature Design," *Nuclear Engineering Design*, Vol. 41, pp. 375-386.

Hecker, S.S. (1971). "Yield Surfaces in Prestrained Aluminum and Copper," *Metall. Trans.*, Vol. 2, pp. 2077-2086.

Hecker, S.S. (1976). "Experimental Studies of Yield Phenomena in Biaxially Loaded Metals," *Constitutive Equations in Viscoplasticity: Computational and Engineering Aspects*, ASME, pp. 1-33.

- Helling, D.E., Miller, A.K., and Stout, M.G. (1986). "An Experimental Investigation of the Yield Loci of 1100-0 Aluminum, 70:30 Brass, and an Overaged 2024 Aluminum Alloy After Various Prestrains," *Journal of Engineering Materials and Technology*, Vol. 108, pp. 313-320.
- Hill, R. (1948). "A Theory of the Yielding and Plastic Flow of Anisotropic Metals," *Proc. Roy. Soc., London, Series A*, Vol. 193, pp. 281-297.
- Hirth, J.P. and Cohen, M. (1970). "On the Strength-Differential Phenomenon in Hardened Steel," *Metall. Trans.*, Vol. 1, pp. 3-8.
- Ivey, H.J. (1961). "Plastic Stress-Strain Relations and Yield Surfaces for Aluminum Alloys," *Journal of Mechanical Engineering Science*, Vol. 3, pp. 15-31.
- Kalish, D. and Cohen, M. (1969). "Anisotropy of Properties in Martensite as Developed by Thermomechanical Treatments," *Trans. ASM*, Vol. 62, no. 2, pp. 353-361.
- Kalluri, S. and Bonacuse, P.J. (1990). "A Data Acquisition and Control Program for Axial-Torsional Fatigue Testing," *Applications of Automation Technology to Fatigue and Fracture Testing, ASTM STP 1092*, A.A. Braun, N.E. Ashbaugh, and F.M. Smith, Eds., American Society for Testing and Materials, Philadelphia, pp. 269-287.
- Kalluri, S., Rao, K.B.S., Halford, G.R., and McGaw, M.A. (1997). "Deformation Mechanisms and Fatigue Behavior of Prestrained Inconel 718 Superalloy," *Proceedings of the Fourth International Special Emphasis Symposium on Superalloys 718, 625, 706 and Derivatives*, Pittsburgh, PA, June 15-18.
- Khan, A. and Wang, X. (1993). "An Experimental Study on Subsequent Yield Surface After Finite Shear Prestraining," *International Journal of Plasticity*, Vol. 9, pp. 889-905.
- Khan, A. and Huang, S. (1995). Continuum Theory of Plasticity. John Wiley & Sons, New York.
- Leslie, W.C. and Sober, R.J. (1967). "The Strength of Ferrite and of Martensite as Functions of Composition, Temperature and Strain rate," *Trans. ASM*, Vol. 60, no. 3, pp. 459-484.

Li, K. (1995). "Experimental Evaluation of a Viscoplastic Constitutive Model," *AIAA/ASME/ASCE/AHS/ASC, Structures, Structural Dynamics and Materials Conference*, 36th, New Orleans, LA, April 10-13.

Lissenden, C.J., Lerch, B.A., Ellis, J.R., and Robinson, D.N. (1997). "Experimental Determination of Yield and Flow Surfaces Under Axial-Torsional Loading," *Multiaxial Fatigue and Deformation Testing Techniques, ASTM STP 1280*, S. Kalluri and P.J. Bonacuse, Eds., American Society for Testing and Materials, pp. 92-112.

Lissenden, C.J. and Arnold, S.M. (1997). "Theoretical and Experimental Considerations in Representing Macroscale Flow/Damage Surfaces for Metal Matrix Composites," *International Journal of Plasticity*, Vol. 13, no. 4, pp. 327-358.

Liu, K.C. (1977). "Yield Surfaces and Elastic-Plastic Behavior of Type 304 Stainless Steel at Room Temperature," *ORNL/TM-5421*, Oak Ridge National Laboratory, Oak Ridge, TN, April.

Mannan, S.L. and Rodriguez, P. (1973). "Strength Differential Effect in Zirconium Alloys," *Scripta Metallurgica*, Vol. 7, no. 10, pp. 1069-1074.

Michno, M.J., Jr. and Findley, W.N., (1974), "Subsequent Yield Surfaces for Annealed Mild Steel Under Dead-Weight Loading: Aging, Normality, Convexity, Corners, Bauschinger, and Cross Effects," *Journal of Engineering Materials and Technology*, Vol. 96, pp. 56-64.

Michno, M.J. and Findley, W.N. (1976). "An Historical Perspective of Yield Surface Investigations for Metals," *International Journal of Nonlinear Mechanics*, Vol. 11, pp. 59-82.

Naghdi, P.M., Essenburg, F., and Koff, W. (1958), "An Experimental Study of Initial and Subsequent Yield Surfaces in Plasticity," *Journal of Applied Mechanics*, Vol. 25, no. 2, pp. 201-209.

Nouailhas, D. and Cailletaud, G. (1996). "Finite Element Analysis of the Mechanical Behavior of Two-Phase Single-Crystal Superalloys," *Scripta Materialia*, Vol. 34, no. 4, pp. 565-571.

Oblak, J.M., Paulonis, D.F., and Duvall, D.S. (1974). "Coherency Strengthening in Ni Base Alloys Hardened by $DO_{22} \gamma$ Precipitates," *Metall. Trans.*, Vol. 5, pp. 143-153.

Olsen, R.J. and Ansell, G.S. (1969). "The Strength Differential in Two-Phase Alloys," *Trans. ASM*, Vol. 62, no. 3, pp. 711-720.

Pampillo, C.A., Davis, L.A., and Li, J.C.M. (1972). "The Effective Modulus Interpretation of the Strength-Differential Effect in Ferrous Alloys," *Scripta Metallurgica*, Vol. 6, no. 8, pp. 765-768.

Phillips, A., Liu, C.S., and Justusson, J.W. (1972). "An Experimental Investigation of Yield Surfaces at Elevated Temperatures," *Acta Mechanica*, Vol. 14, pp. 119-146.

Phillips, A. and Tang, J.L. (1972). "The Effect of Loading Path on the Yield Surface at Elevated Temperatures," *International Journal of Plasticity*, Vol. 8, pp. 463-474.

Phillips, A. and Moon, H. (1977). "An Experimental Investigation Concerning Yield Surfaces and Loading Surfaces," *Acta Mechanica*, Vol. 27, pp. 91-102.

Phillips, A. and Lu, W. (1984). "An Experimental Investigation of Yield Surfaces and Loading Surfaces of Pure Aluminum With Stress-Controlled and Strain-Controlled Paths of Loading," *Journal of Engineering Materials and Technology, Trans. ASME*, Vol. 106, pp. 349-354.

Prager, W. (1956). "A New Method of Analyzing Stresses and Strains in Work-Hardening Plastic Solids," *Journal of Applied Mechanics*, Vol. 78, pp. 493-496.

Prandtl, L. (1924). "Spannungsverteilung in plastischen Koerpern," *Proceedings. 1st International Congress on Applied Mechanics*, Delft, J. Waltman, Jr., Ed., Technische Boekhandel en Druckerij, pp. 43-54.

Rauch, G.C. and Leslie, W.C. (1972). "The Extent and Nature of the Strength-Differential Effect in Steels," *Metall. Trans.*, Vol. 3, no. 2, pp. 373-385.

Rauch, G.C., Daga, R.L., Radcliffe, S.V., Sober, R.J., and Leslie, W.C. (1975). "Volume Expansion, Pressure Effects, and the Strength Differential in As-Quenched Iron-Carbon Martensite," *Metall. Trans. A*, Vol. 6A, no. 12, pp. 2279-2287.

Reuss, E. (1930). "Beruecksichtigung der elastischen Formaenderungen in der Plastizitaetstheorie," *Zeitschrift fur Angewandte Mathematik und Mechanik*, Vol. 10, pp. 266-274.

Robinson, D.N. (1985). "On Thermomechanical Testing in Support of Constitutive Equation Development for High-Temperature Alloys," NASA CR-174879, NASA Lewis Research Center, Cleveland, OH.

Spitzig, W.A., Sober, R.J., and Richmond, O. (1975). "Pressure Dependence of Yielding and Associated Volume Expansion in Tempered Martensite," *Acta Metall.*, Vol. 23, pp. 885-893.

Stouffer, D.C. and Dame, L.T. (1996). Inelastic Deformation of Metals: Models, Mechanical Properties, and Metallurgy. John Wiley & Sons, Inc., New York, pp. 36-40.

Sundararaman, M., Mukhopadhyay, P., and Banerjee, S. (1988). "Deformation Behavior of γ " Strengthened Inconel 718," *Acta Metall.* Vol. 36, No. 4, pp. 847-864.

Taylor, G.I. and Quinney, H. (1931). "The Plastic Distortion of Metals," *Philosophical Transactions of the Royal Society*, London, Vol. A230, pp. 323-363.

Tresca, H. (1864). "Sur l'écoulement des corps solides soumis 'a defortes pression," *C.R. Acad. Sci.*, Paris, Vol. 59, p. 754.

von Mises, R. (1913). "Mechanics of Solids in the Plastically Deformable State," *NASA Technical Memorandum 88488*, 1986. (translation of *Mechanik der festen Körper im plastisch-deformablem Zustrand*, *Nachrichten von der Koniglichen Gesellschaft der Wissenschaften*, pp. 582-592).

von Mises, R. (1928). "Mechanik der plastischen Formaenderung von Kristallen," *Zeitschrift fur Angewandte Mathematik und Mechanik*, Vol. 8, pp. 161-185.

Voyiadjis, G.Z. and Foroozesh, M. (1990). "Anisotropic Distortional Yield Model," *Journal of Applied Mechanics*, Vol. 57, pp. 537-547.

Williams, J.F. and Svensson, N.L. (1970). "Effect of Tensile Prestrain on the Yield Locus of 1100-F Aluminum," *Journal of Strain Analysis*, Vol. 5, pp. 128-139.

Williams, J.F. and Svensson, N.L. (1971). "Effect of Torsional Prestrain on the Yield Locus of 1100-F Aluminum," *Journal of Strain Analysis*, Vol. 6, pp. 263-272.

Winstone, M.R., Wright, M.L., and Rawlings, R.D. (1973). "The Strength Differential in Some Titanium Alloys," *Scripta Metallurgica*, Vol. 7, no. 12, pp. 1265-1268.

Worthern, D.W., Altstetter, C.J., Robertson, I.M., and Socie, D.F. (1989). "Cyclic Deformation and Damage Structure in Inconel 718," *Biaxial and Multiaxial Fatigue*, EGF 3 (Edited by M. W. Brown and K. J. Miller), Mechanical Engineering Publications, London, pp. 131-143.

Wu, Han C. and Yeh, Wei C. (1991). "On the Experimental Determination of Yield Surfaces and Some Results of Annealed 304 Stainless Steel," *International Journal of Plasticity*, Vol. 7, pp. 803-826.

Ziegler, H. (1959). "A Modification of Prager's Hardening Rule," *Quarterly of Applied Mathematics*, Vol. 17, pp. 55-65.

APPENDIX A

YIELD LOCI AND FLOW SURFACE DATA

A.1 Yield Loci

Data from Fig. 4.6

<u>Spec. IN-6</u>			<u>Spec. IN-25</u>		
<u>Probe</u> <u>Angle</u>	<u>σ_{11}</u> <u>(MPa)</u>	<u>σ_{12}</u> <u>(MPa)</u>	<u>Probe</u> <u>Angle</u>	<u>σ_{11}</u> <u>(MPa)</u>	<u>σ_{12}</u> <u>(MPa)</u>
12	236	26	12	234	26
35	215	81	35	211	83
57	141	116	57	134	115
80	49	141	80	50	142
102	-49	144	102	-46	149
125	-152	125	125	-148	128
147	-220	78	147	-217	83
170	-251	23	170	-253	24
192	-237	-27	192	-239	-30
215	-211	-79	215	-211	-84
237	-147	-116	237	-146	-121
260	-58	-139	260	-57	-144
282	39	-137	282	37	-138
305	141	-119	305	134	-119
327	197	-73	327	188	-72
350	234	-23	350	226	-23

Data from Fig. 4.8

<u>Spec. IN-6</u>			<u>Spec. IN-25</u>		
Probe Angle	σ_{11} (MPa)	σ_{12} (MPa)	Probe Angle	σ_{11} (MPa)	σ_{12} (MPa)
12	181	19	12	185	24
35	172	64	35	166	67
57	110	92	57	112	101
80	35	106	80	40	121
102	-44	122	102	-40	127
125	-128	103	125	-125	110
147	-185	66	147	-181	70
170	-210	20	170	-211	20
192	-201	-23	192	-208	-28
215	-180	-66	215	-182	-74
237	-121	-95	237	-124	-104
260	-48	-116	260	-49	-122
282	33	-111	282	29	-113
305	114	-96	305	110	-100
327	154	-58	327	164	-64
350	190	-20	350	182	-18

Data from Fig. 4.9

<u>Spec. IN-6</u>			<u>Spec. IN-25</u>		
Probe Angle	σ_{11} (MPa)	σ_{12} (MPa)	Probe Angle	σ_{11} (MPa)	σ_{12} (MPa)
12	164	17	12	157	24
35	160	61	35	161	69
57	98	84	57	105	104
80	36	111	80	36	123
102	-44	122	102	-40	125
125	-133	106	125	-123	106
147	-194	68	147	-179	68
170	-219	20	170	-215	20
192	-209	-24	192	-215	-32
215	-179	-67	215	-176	-74
237	-129	-102	237	-120	-106
260	-49	-118	260	-40	-110
282	30	-104	282	30	-105
305	99	-86	305	74	-66
327	130	-48	327	142	-55
350	150	-13	350	172	-15

Data from Fig. 4.11

Probe Angle	Spec. IN-6	
	σ_{11} (MPa)	σ_{12} (MPa)
12	186	46
35	186	76
57	142	92
80	97	111
102	41	117
125	-39	121
147	-126	102
170	-143	54
192	-98	15
215	-82	-24
237	-39	-55
260	29	-82
282	112	-85
305	168	-43
327	190	-6
350	199	23

Data from Fig. 4.14

Probe Angle	Spec. IN-6	
	σ_{11} (MPa)	σ_{12} (MPa)
12	137	14
35	125	46
57	75	65
80	27	87
102	-47	114
125	-135	105
147	-194	66
170	-195	15
192	-211	-24
215	-186	-70
237	-132	-107
260	-48	-129
282	38	-120
305	118	-97
327	152	-55
350	161	-16

Data from Fig. 4.15

Probe Angle	Spec. IN-6 (Locus Q)	
	σ_{11} (MPa)	σ_{12} (MPa)
12	193	47
35	182	75
57	143	95
80	95	110
102	39	119
125	-50	129
147	-141	108
170	-164	55
192	-101	13
215	-63	-17
237	-46	-66
260	27	-105
282	121	-102
305	179	-49
327	189	-6
350	201	21

Probe Angle	Spec. IN-6 (Locus S)	
	σ_{11} (MPa)	σ_{12} (MPa)
12	208	63
35	195	89
57	167	110
80	121	122
102	73	124
125	-9	139
147	-103	124
170	-97	69
192	-40	36
215	-56	-9
237	-15	-47
260	50	-89
282	139	-71
305	209	-41
327	215	11
350	223	41

Data from Fig. 4.17

<u>Spec. IN-8</u>			<u>Spec. IN-10</u>		
Probe Angle	σ_{11} (MPa)	σ_{12} (MPa)	Probe Angle	σ_{11} (MPa)	σ_{12} (MPa)
12	536	64	12	486	58
35	450	186	35	491	200
57	286	263	57	317	290
80	115	377	80	122	401
102	-141	415	102	-153	444
125	-426	374	125	-431	383
147	-633	251	147	-648	261
170	-774	83	170	-799	94
192	-766	-98	192	-780	-94
215	-657	-271	215	-619	-250
237	-374	-335	237	-348	-310
260	-117	-354	260	-113	-348
282	100	-316	282	92	-283
305	262	-231	305	282	-252
327	440	-177	327	388	-156
350	460	-53	350	474	-58

Data for Fig. 4.19

<u>Spec. IN-8</u>			<u>Spec. IN-10</u>		
Probe Angle	σ_{11} (MPa)	σ_{12} (MPa)	Probe Angle	σ_{11} (MPa)	σ_{12} (MPa)
12	373	48	12	295	33
35	320	135	35	266	111
57	204	191	57	190	175
80	70	235	80	70	229
102	-92	274	102	-93	277
125	-264	231	125	-293	261
147	-475	186	147	-386	157
170	-506	52	170	-614	71
192	-513	-69	192	-592	-72
215	-382	-161	215	-416	-171
237	-269	-244	237	-267	-242
260	-69	-219	260	-76	-238
282	64	-198	282	66	-211
305	163	-143	305	181	-164
327	286	-114	327	297	-122
350	312	-34	350	222	-27

Data for Fig. 4.20

<u>Spec. IN-10</u>		
Probe Angle	σ_{11} (MPa)	σ_{12} (MPa)
12	563	221
35	580	273
57	513	299
80	450	337
102	356	351
125	239	357
147	26	359
170	57	244
192	-351	109
215	-112	-18
237	91	-98
260	331	-70
282	483	-22
305	602	30
327	611	120
350	631	175

Data for Fig. 4.21

<u>Spec. IN-8</u>		
Probe Angle	σ_{11} (MPa)	σ_{12} (MPa)
12	743	42
35	689	120
57	590	177
80	472	242
102	313	254
125	103	262
147	-153	220
170	-263	72
192	-163	-72
215	-128	-219
237	142	-234
260	320	-246
282	457	-185
305	593	-172
327	648	-100
350	641	-28

Data for Fig. 4.22

<u>Spec. IN-6 (virgin)</u>			<u>Spec. IN-6 (re-solut.)</u>			<u>Spec. IN-8 (re-solut.)</u>		
Probe Angle	σ_{11} (MPa)	σ_{12} (MPa)	Probe Angle	σ_{11} (MPa)	σ_{12} (MPa)	Probe Angle	σ_{11} (MPa)	σ_{12} (MPa)
12	205	27	12	212	35	12	207	27
35	204	76	35	198	86	35	199	83
57	134	110	57	124	118	57	126	115
80	49	134	80	42	144	80	41	139
102	-43	132	102	-47	139	102	-48	134
125	-141	116	125	-144	124	125	-140	120
147	-202	72	147	-207	79	147	-203	79
170	-234	21	170	-239	21	170	-243	24
192	-204	-25	192	-203	-29	192	-215	-28
215	-196	-74	215	-190	-82	215	-198	-82
237	-132	-104	237	-124	-115	237	-127	-113
260	-54	-130	260	-44	-138	260	-44	-137
282	35	-118	282	41	-124	282	40	-123
305	134	-114	305	135	-119	305	136	-118
327	183	-69	327	184	-72	327	185	-72
350	223	-21	350	231	-20	350	226	-23

A.2 Flow Surfaces

Data for Fig. 6.3

SCIP (120 Pa/sec)			SCISR (0.574 sec ⁻¹)		
Probe Angle	σ_{11} (MPa)	σ_{12} (MPa)	Probe Angle	σ_{11} (MPa)	σ_{12} (MPa)
12	211	23	12	211	23
35	187	74	35	188	74
57	118	101	57	114	98
79	46	132	79	46	133
102	-41	132	102	-41	134
125	-133	115	125	-134	116
147	-196	75	147	-197	76
170	-230	22	170	-231	22
192	-219	-28	192	-220	-28
215	-194	-77	215	-195	-77
237	-132	-110	237	-132	-110
259	-51	-130	259	-51	-130
282	34	-126	282	34	-126
305	123	-110	305	124	-110
327	177	-68	327	177	-68
350	211	-21	350	212	-21

Data for Fig. 6.4

Probe Angle	SCISR (0.75 sec ⁻¹)	
	σ_{11} (MPa)	σ_{12} (MPa)
12	173	23
35	152	62
57	101	92
79	38	114
102	-36	115
125	-115	101
147	-165	65
170	-196	19
192	-192	-25
215	-168	-67
237	-114	-96
259	-45	-111
282	28	-110
305	104	-95
327	153	-60
350	174	-17

Data for Fig. 6.5

Probe Angle	SCIP (60 Pa/sec)		Probe Angle	SCIP (120 Pa/sec)	
	σ_{11} (MPa)	σ_{12} (MPa)		σ_{11} (MPa)	σ_{12} (MPa)
12	151	20	12	171	22
35	141	57	35	150	61
57	94	85	57	100	91
79	35	104	79	37	112
102	-33	107	102	-35	114
125	-109	96	125	-113	99
147	-157	62	147	-163	64
170	-182	18	170	-195	19
192	-174	-22	192	-188	-24
215	-160	-64	215	-167	-67
237	-107	-90	237	-112	-94
259	-42	-102	259	-44	-109
282	24	-95	282	28	-108
305	95	-86	305	102	-93
327	138	-54	327	152	-59
350	158	-15	350	172	-17

Data for Fig. 6.6

Probe Angle	SCISR (0.75 sec ⁻¹)	
	σ_{11} (MPa)	σ_{12} (MPa)
12	157	43
35	170	71
57	125	77
79	93	96
102	47	102
125	-24	111
147	-106	96
170	-121	52
192	-82	17
215	-60	-15
237	-26	-45
259	36	-63
282	109	-79
305	161	-37
327	174	0
350	180	25

Data for Fig. 6.7

Probe Angle	SCIP (60 Pa/sec)		Probe Angle	SCIP (120 Pa/sec)	
	σ_{11} (MPa)	σ_{12} (MPa)		σ_{11} (MPa)	σ_{12} (MPa)
12	140	41	12	158	43
35	161	67	35	167	70
57	116	69	57	125	78
79	89	81	79	93	94
102	53	87	102	48	100
125	-11	101	125	-21	108
147	-96	93	147	-104	95
170	-113	51	170	-126	52
192	-81	17	192	-97	15
215	-63	-16	215	-	-
237	-26	-45	237	-32	-49
259	38	-57	259	-	-
282	103	-58	282	109	-79
305	141	-20	305	160	-36
327	145	11	327	171	1
350	158	27	350	177	25

Data for Fig. 6.8

Probe Angle	SCISR (0.25 sec ⁻¹)	
	σ_{11} (MPa)	σ_{12} (MPa)
12	444	53
35	380	157
57	245	225
79	102	332
102	-125	370
125	-384	339
147	-568	226
170	-716	77
192	-686	-87
215	-587	-243
237	-327	-294
259	-97	-297
282	77	-243
305	208	-183
327	350	-140
350	357	-41

Data for Fig. 6.9

Probe Angle	SCIP (60 Pa/sec)		Probe Angle	SCIP (120 Pa/sec)	
	σ_{11} (MPa)	σ_{12} (MPa)		σ_{11} (MPa)	σ_{12} (MPa)
12	408	48	12	448	53
35	351	144	35	382	157
57	199	182	57	260	238
79	85	277	79	100	327
102	-96	289	102	-111	331
125	-345	304	125	-372	329
147	-511	204	147	-551	219
170	-620	67	170	-701	76
192	-566	-72	192	-667	-85
215	-528	-218	215	-573	-237
237	-278	-250	237	-322	-289
259	-82	-252	259	-95	-292
282	64	-202	282	83	-262
305	178	-157	305	226	-199
327	311	-124	327	360	-144
350	323	-37	350	382	-44

Data for Fig. 6.10

Probe Angle	SCISR (0.25 sec ⁻¹)	
	σ_{11} (MPa)	σ_{12} (MPa)
12	311	39
35	256	108
57	163	152
79	59	198
102	-81	241
125	-239	209
147	-443	175
170	-451	46
192	-413	-56
215	-355	-150
237	-222	-202
259	-58	-184
282	54	-167
305	97	-85
327	231	-92
350	215	-23

Data for Fig. 6.11

Probe Angle	SCIP (60 Pa/sec)		Probe Angle	SCIP (120 Pa/sec)	
	σ_{11} (MPa)	σ_{12} (MPa)		σ_{11} (MPa)	σ_{12} (MPa)
12	304	39	12	323	41
35	246	104	35	275	116
57	148	139	57	194	181
79	53	179	79	64	216
102	-71	213	102	-84	250
125	-215	188	125	-243	213
147	-426	168	147	-447	176
170	-416	43	170	-454	47
192	-362	-49	192	-430	-58
215	-299	-127	215	-360	-152
237	-203	-185	237	-238	-215
259	-52	-164	259	-66	-208
282	45	-142	282	61	-191
305	122	-107	305	161	-142
327	226	-90	327	252	-101
350	220	-24	350	280	-30

Data for Fig. 6.12

Probe Angle	SCISR (0.25 sec ⁻¹)	
	σ_{11} (MPa)	σ_{12} (MPa)
12	467	209
35	458	221
57	455	242
79	443	312
102	371	317
125	269	331
147	74	341
170	81	241
192	-287	117
215	-101	-14
237	118	-73
259	337	-50
282	471	20
305	576	54
327	558	143
350	550	186

Data for Fig. 6.13

Probe Angle	SCIP (60 Pa/sec)		Probe Angle	SCIP (120 Pa/sec)	
	σ_{11} (MPa)	σ_{12} (MPa)		σ_{11} (MPa)	σ_{12} (MPa)
12	467	209	12	485	211
35	458	221	35	458	221
57	449	236	57	453	240
79	432	274	79	442	310
102	372	311	102	371	316
125	391	222	125	277	324
147	96	332	147	79	338
170	-	-	170	-	-
192	-290	117	192	-326	112
215	-	-	215	-	-
237	92	-97	237	-	-
259	336	-52	259	-	-
282	467	35	282	475	8
305	455	164	305	576	54
327	547	147	327	558	143
350	550	186	350	550	186

Data for Fig. 6.14

Probe Angle	SCISR (0.25 sec ⁻¹)	
	σ_{11} (MPa)	σ_{12} (MPa)
12	564	20
35	615	90
57	563	152
79	464	215
102	325	221
125	-	-
147	-82	192
170	-201	65
192	-79	-61
215	-76	-197
237	163	-216
259	330	-217
282	422	-72
305	563	-146
327	569	-68
350	475	-10

Data for Fig. 6.15

Probe Angle	SCIP (60 Pa/sec)		Probe Angle	SCIP (120 Pa/sec)	
	σ_{11} (MPa)	σ_{12} (MPa)		σ_{11} (MPa)	σ_{12} (MPa)
12	514	13	12	548	18
35	602	84	35	612	88
57	538	129	57	559	148
79	460	203	79	466	221
102	331	204	102	322	229
125	118	249	125	-	-
147	-70	187	147	-116	205
170	-203	65	170	-226	68
192	-124	-67	192	-	-
215	-66	-193	215	-97	-206
237	-	-	237	-	-
259	335	-201	259	327	-227
282	420	-66	282	422	-74
305	551	-135	305	562	-145
327	539	-56	327	562	-65
350	475	-10	350	475	-10

APPENDIX B

FLOW SURFACE EXPERIMENTS ON SiC/Ti-6-2-4-2

B.1 Introduction

Prior to the work on Inconel 718, flow surface experiments were performed on unidirectional SiC/Ti-6-2-4-2 tubular specimens. Unfortunately, these experiments were not completely successful. This appendix serves as a record of these experiments and offers some explanations for their unsuccessful nature and suggestions for future work.

B.2 Results, Discussion, and Suggested Future Work

Small offset flow surface experiments (to 10 $\mu\epsilon$ equivalent offset strain) were performed on SiC/Ti-6-2-4-2 initially at 23°C, where stiffening was observed during compressive loading. In fact, it was in these specimens where stiffening was first observed. However, after modifying the test procedure (see Chapter 4), stiffening no longer posed a problem.

A series of tension/compression cycles were then performed to observe the repeatability. The maximum absolute stress values are plotted in Figure

B.1. The results are reasonably repeatable, which suggests that stiffening does not hinder the ability to determine flow surfaces.

A flow surface was then performed at 482°C (shown in Fig. B.2).

Unfortunately, the results were somewhat meaningless. It is believed that the main problem in these experiments is associated with a weak bond strength between the fibers and the matrix. Nonetheless, based on the average stress values in tension and compression in Figure B.1 and any data from Figure B.2 that appeared to be reasonable, a best-guess surface is shown.

It does not appear possible to perform small offset flow surface experiments on these particular SiC/Ti-6-2-4-2 specimens. Future work should include large offset experiments, where one point on the surface is obtained from each specimen. Unfortunately, this would require many specimens and be very costly. However, these types of experiments would provide more meaningful data on the inelastic flow and damage behavior of SiC/Ti-6-2-4-2 under multiaxial loading conditions.

SiC/Ti-6-2-4-2 Tubes

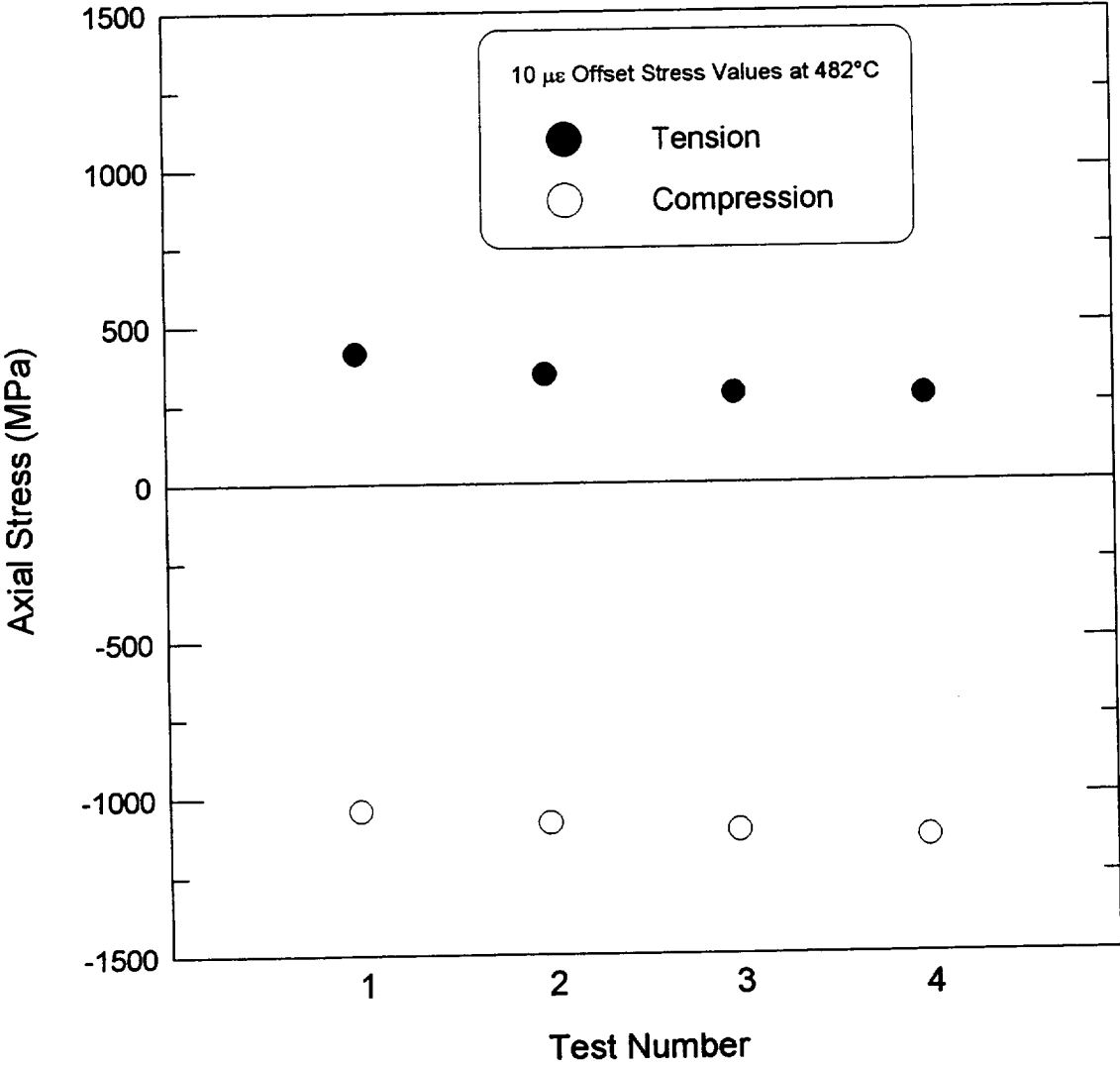


Figure B.1 - Max/Min stresses for SiC/Ti-6-2-4-2 tubes under axial loading at 482°C.

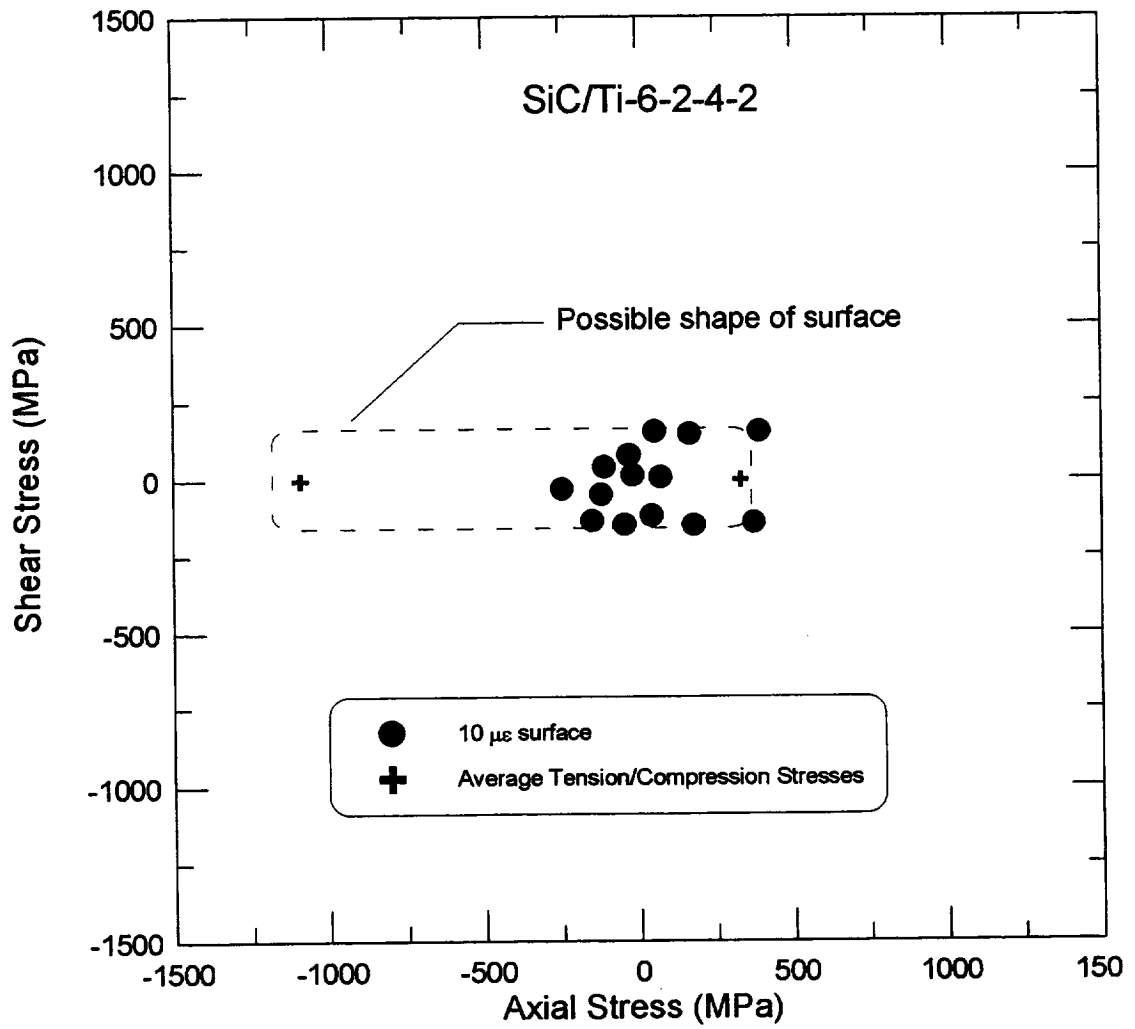


Figure B.2 - Attempt at an initial surface on SiC/Ti-6-2-4-2 at 482°C.

REPORT DOCUMENTATION PAGE

Form Approved
OMB No. 0704-0188

Public reporting burden for this collection of information is estimated to average 1 hour per response, including the time for reviewing instructions, searching existing data sources, gathering and maintaining the data needed, and completing and reviewing the collection of information. Send comments regarding this burden estimate or any other aspect of this collection of information, including suggestions for reducing this burden, to Washington Headquarters Services, Directorate for Information Operations and Reports, 1215 Jefferson Davis Highway, Suite 1204, Arlington, VA 22202-4302, and to the Office of Management and Budget, Paperwork Reduction Project (0704-0188), Washington, DC 20503.

1. AGENCY USE ONLY (Leave blank)		2. REPORT DATE July 1998	3. REPORT TYPE AND DATES COVERED Final Contractor Report	
4. TITLE AND SUBTITLE Determination of Yield and Flow Surfaces for Inconel 718 Under Axial-Torsional Loading at Temperatures up to 649 °C			5. FUNDING NUMBERS WU-523-21-13-00 NCC3-597	
6. AUTHOR(S) Christopher M. Gil				
7. PERFORMING ORGANIZATION NAME(S) AND ADDRESS(ES) Pennsylvania State University 110 Technology Center University Park, Pennsylvania 16802			8. PERFORMING ORGANIZATION REPORT NUMBER E-11201	
9. SPONSORING/MONITORING AGENCY NAME(S) AND ADDRESS(ES) National Aeronautics and Space Administration Lewis Research Center Cleveland, Ohio 44135-3191			10. SPONSORING/MONITORING AGENCY REPORT NUMBER NASA CR-1998-207932	
11. SUPPLEMENTARY NOTES This was report was submitted as a thesis in partial fulfillment of the requirements for the degree Master of Science in Engineering Mechanics to Pennsylvania State University in May 1998. Project Manager, Brad Lerch, Structures and Acoustics Division, NASA Lewis Research Center, organization code 5920, (216) 433-5522.				
12a. DISTRIBUTION/AVAILABILITY STATEMENT Unclassified - Unlimited Subject Category: 39 This publication is available from the NASA Center for AeroSpace Information, (301) 621-0390.			12b. DISTRIBUTION CODE Distribution: Nonstandard	
13. ABSTRACT (Maximum 200 words) An experimental program to determine flow surfaces has been established and implemented for solution annealed and aged IN718. The procedure involved subjecting tubular specimens to various ratios of axial-torsional stress at temperatures between 23 and 649 °C and measuring strain with a biaxial extensometer. Each stress probe corresponds to a different direction in stress space, and unloading occurs when a 30 microstrain ($1 \mu\epsilon = 10^{-6}$ mm/mm) offset is detected. This technique was used to map out yield loci in axial-torsional stress space. Flow surfaces were determined by post-processing the experimental data to determine the inelastic strain rate components. Surfaces of constant inelastic strain rate (SCISRs) and surfaces of constant inelastic power (SCIPs) were mapped out in the axial-shear stress plane. The von Mises yield criterion appeared to closely fit the initial loci for solutioned IN718 at 23 °C. However, the initial loci for solutioned IN718 at 371 and 454 °C, and all of the initial loci for aged IN718 were offset in the compression direction. Subsequent loci showed translation, distortion, and for the case of solutioned IN718, a slight cross effect. Aged IN718 showed significantly more hardening behavior than solutioned IN718.				
14. SUBJECT TERMS Plastic deformation; Plastic flow; Inconel; Yield strength; Viscoplasticity; Torsion			15. NUMBER OF PAGES 163	
			16. PRICE CODE A08	
17. SECURITY CLASSIFICATION OF REPORT Unclassified	18. SECURITY CLASSIFICATION OF THIS PAGE Unclassified	19. SECURITY CLASSIFICATION OF ABSTRACT Unclassified	20. LIMITATION OF ABSTRACT	